High-resolution SOFIA/EXES Spectroscopy of Water Absorption Lines in the Massive Young Binary W3 IRS 5

Li, J.; Boogert, A.; Barr, A.G.; DeWitt, C.; Rashman, M.; Neufeld, D.; ... ; Tielens, A.G.G.M.

Citation
Li, J., Boogert, A., Barr, A. G., DeWitt, C., Rashman, M., Neufeld, D., … Tielens, A. G. G. M. (2023). High-resolution SOFIA/EXES Spectroscopy of Water Absorption Lines in the Massive Young Binary W3 IRS 5. *The Astrophysical Journal*, *953*(1). doi:10.3847/1538-4357/ace16e

The Astrophysical Journal, 953:103 (30pp), 2023 August 10 https://doi.org/10.3847/1538-4357/ace16e

High-resolution SOFIA/EXES Spectroscopy of Water Absorption Lines in the Massive Young Binary W3 IRS 5

Jialu Li (李佳璐)[1], Adwin Boogert[2], Andrew G. Barr[3], Curtis DeWitt[4], Maisie Rashman[4], David Neufeld[5], Nick Indriolo[6], Yvonne Pendleton[7], Edward Montiel[8], Matt Richter[9], J. E. Chiar[10], and Alexander G. G. M. Tielens[1,11]

[1] Department of Astronomy, University of Maryland, College Park, MD 20742, USA; jialu@astro.umd.edu
[2] Institute for Astronomy, University of Hawaii, 2680 Woodlawn Drive, Honolulu, HI 96822, USA
[3] SRON Netherlands Institute for Space Research, Niels Bohrweg 4, 2333 CA Leiden, The Netherlands
[4] SOFIA Science Center, USRA, NASA Ames Research Center, M.S. N232-12, Moffett Field, CA 94035, USA
[5] Department of Physics and Astronomy, Johns Hopkins University, Baltimore, MD 20218, USA
[6] AURA for ESA, Space Telescope Science Institute, Baltimore, MD 21218, USA
[7] Department of Physics, University of Central Florida, Orlando, FL 32816 USA
[8] USRA, SOFIA, NASA Ames Research Center, MS 232-11, Moffett Field, CA 94035, USA
[9] University of California Davis, Phys 539, Davis, CA 95616, USA
[10] Physical Science Department, Diablo Valley College, 321 Golf Club Road, Pleasant Hill, CA 94523, USA
[11] Leiden University, Niels Bohrweg 2, 2333 CA Leiden, The Netherlands

Received 2023 February 13; revised 2023 June 23; accepted 2023 June 23; published 2023 August 8

Abstract

We present in this paper mid-infrared (5–8 μm) spectroscopy toward the massive young binary W3 IRS 5, using the Echelon Cross Echelle Spectrograph (EXES) spectrometer in high-resolution mode ($R \sim 50{,}000$) from the NASA Stratospheric Observatory for Infrared Astronomy (SOFIA). Many ($\sim$180) $\nu_2 = 1$–0 and ($\sim$90) $\nu_2 = 2$–1 absorption rovibrational transitions are identified. Two hot components over 500 K and one warm component of 190 K are identified through Gaussian fittings and rotation diagram analysis. Each component is linked to a CO component identified in the IRTF/iSHELL observations ($R = 88{,}100$) through their kinematic and temperature characteristics. Revealed by the large scatter in the rotation diagram, opacity effects are important, and we adopt two curve-of-growth analyses, resulting in column densities of $\sim 10^{19}$ cm^{-2}. In one analysis, the model assumes a foreground slab. The other assumes a circumstellar disk with an outward-decreasing temperature in the vertical direction. The disk model is favored because fewer geometry constraints are needed, although this model faces challenges as the internal heating source is unknown. We discuss the chemical abundances along the line of sight based on the CO-to-H_2O connection. In the hot gas, all oxygen not locked in CO resides in water. In the cold gas, we observe a substantial shortfall of oxygen and suggest that the potential carrier could be organics in solid ice.

Unified Astronomy Thesaurus concepts: Star formation (1569); Infrared sources (793); Interstellar molecules (849); Infrared spectroscopy (2285)

1. Introduction

Massive stars reach the main sequence while deeply embedded and still accreting. While rich chemistry is driven as the central object warms and ionizes the environment, complicated physical activities such as accretion disks, outflows, shocks, and disk winds are involved (Beuther et al. 2007; Cesaroni et al. 2007; Zinnecker & Yorke 2007). However, the large distances to the observers, the high extinction at optical and near-infrared wavelengths, and the highly clustered environment impede a clear understanding of their formation and evolution processes.

High spectral resolution, pencil beam absorption line studies at mid-infrared (MIR) wavelengths provide a unique opportunity to probe the embedded phases in massive star formation (Lacy 2013). First, the MIR continuum originates from the photosphere of the disk at a distance of tens to a few hundreds of astronomical unit (Beltrán & de Wit 2016; Frost et al. 2021). The effective pencil beam, therefore, avoids beam dilution issues that submillimeter observations are subject to. Second, molecules without dipole moments such as C_2H_2 and CH_4, which are among the most abundant carbon-bearing molecules, can only be observed through their rovibrational spectra in the infrared. Therefore, MIR spectroscopy at high resolution is a critical tracer of the physical conditions, the chemical inventory, and the kinematics of structures close to the massive protostars.

Among the rich chemical inventory in the regions associated with the protostars, water is of fundamental importance because it is one of the most abundant molecules in both the gas and ice phases. As its abundance varies largely between warm and cold gas (e.g., Draine et al. 1983; Kaufman & Neufeld 1996; Bergin et al. 2002), water has a powerful diagnostic capability in probing physical conditions (van Dishoeck et al. 2021). However, due to its prevalence in the Earth's atmosphere, water is very difficult to observe from the ground. We present in this work the power of combining the Stratospheric Observatory for Infrared Astronomy (SOFIA; Young et al. 2012) that observes between 39,000 and 45,000 ft and the Echelon Cross Echelle Spectrograph (EXES; Richter et al. 2018) spectrometer, which resolves lines to several km s^{-1} to make the most of the diagnostic capability of water.

Previous studies of the MIR water absorption spectrum toward massive protostars (Boonman & van Dishoeck 2003; Boonman et al. 2003) have revealed a rich spectral content. High spectral resolution observations can provide much insight into the characteristics of these regions (e.g., Knez et al. 2009; Indriolo et al. 2015; Barr et al. 2018; Dungee et al. 2018; Indriolo et al. 2018; Rangwala et al. 2018; Goto et al. 2019; Barr et al. 2020; Indriolo et al. 2020; Nickerson et al. 2021; Barr et al. 2022a, 2022b; Li et al. 2022; Nickerson et al. 2023). Water has also been studied at high spectral resolution via pure rotational transitions, using the heterodyne instruments on board SWAS, Odin, and Herschel Space Observatory (e.g., Snell et al. 2000; Wilson et al. 2003; Chavarría et al. 2010; Karska et al. 2014). Because of their limited spatial resolution, these observations mainly probed the large-scale environment of these sources.

We conducted high spectral resolution ($R = 50{,}000$) spectroscopy from 5–8 μm with EXES on board SOFIA toward the hot core region close to the massive binary protostar W3 IRS 5, which is a luminous, massive protostellar binary in transition from the embedded to the exposed phase of star formation (van der Tak et al. 2000, 2005). W3 IRS 5 is oriented along the northeast-to-southwest direction with a separation of 1$''$.2 (∼2800 au at $2.3^{+0.19}_{-0.16}$ kpc; Navarete et al. 2019). Following the nomenclature in van der Tak et al. (2005), we refer to the northeastern object of the binary as MIR1 and the southwestern one as MIR2.

Millimeter studies reveal complex structures surrounding the binary on a large scale (10^3–10^5 au), including a hot molecular core with outflows, jet lobes, shocks, and a circumbinary toroid (Imai et al. 2000; Rodón et al. 2008; Wang et al. 2012, 2013; Purser et al. 2021). In the infrared *M*-band (4.7 μm), high spectral resolution (R = 88,100) observations of rovibrational transitions of CO and its isotopologues (Li et al. 2022) show various absorbing structures along the pencil beam line of weight against the pencil beam MIR background. Physical conditions such as temperature and column density have been derived from these CO observations. While MIR1 and MIR2 are spatially resolved in Li et al. (2022), the absorbing components are identified as a shared envelope (∼50 K at −38.5 km s^{-1}), several foreground clumps produced by either J- or C-shocks (200–300 K from −100 to −60 km s^{-1}), and blobs that are likely associated with the circumstellar disks (∼500 K from −55 to −38.5 km s^{-1}). The *M*-band study sets up the backdrop for understanding the origin of spatially unresolved water absorption lines in this paper, and we refer readers to Table 7 in Li et al. (2022) for a complete list of properties of each decomposed CO component.

This paper presents the rich spectrum of rovibrational (the ν_2 band) water lines observed in absorption toward W3 IRS 5. The high spectral resolution spectroscopy allows us to separate and identify individual velocity components that are linked to different stars in the W3 IRS 5 binary and to derive the temperatures, the level-specific column densities, as well as the total column densities (and/or the abundances). We describe our observations and data reduction in Section 2 and our analysis methods with both the rotation diagram and the curve-of-growth in Section 3. We present in Section 4 the properties of multiple dynamical components and set up the connection between these water components to CO components that are identified in Li et al. (2022). We discuss the chemical abundances along the line of sight based on the CO-to-H_2O connection in Section 5.

2. Observations and Data Reduction

Object W3 IRS 5 was observed with the EXES spectrometer (Richter et al. 2018) on board the SOFIA observatory from 2021 June to 2022 February as part of programs 08_0136 and 09_0072. Archival data observed in programs 07_0063 and 76_0004 were also included in this study. The full spectral survey covers a wavelength range of 5.3–7.9 μm in 18 observational settings and was observed under the HIGH-LOW cross-dispersed mode. The observational parameters of all 18 settings are listed in Table 1. For all settings, the slit width is fixed to 3$''$.2 to limit slit losses perpendicular to the slit at an SOFIA point-spread function (PSF) FWHM (see ∼3$''$.0–3$''$.5), which provides a spectral resolution of $R \sim 50{,}000$, or equivalently, a velocity resolution of 6 km s^{-1}. The slit length is dependent on the wavelength and the angle of the echelle grating and is in the range of 1$''$.36–3$''$.43 after accounting for the anamorphic magnification (Figure 1). Off-slit nodding was applied to remove the background night sky emission and the telescope thermal emission.

The EXES data were reduced with the SOFIA Redux pipeline (Clarke et al. 2015), which has incorporated routines originally developed for the Texas Echelon Cross Echelle Spectrograph (Lacy et al. 2003). The science frames were despiked and sequential nod positions subtracted, to remove telluric emission lines and telescope/system thermal emission. An internal blackbody source was observed for flat-fielding and flux calibration and then the data were rectified, aligning the spatial and spectral dimensions. The wavenumber solution was calibrated using sky emission spectra produced for each setting by omitting the nod-subtraction step. We used wavenumber values from HITRAN (Rothman et al. 2013) to set the wavelength scale. The resulting wavelength solutions have 1σ errors of 0.5 km s^{-1}.

Before measuring intrinsic lines in the source, the spectra had to be corrected for telluric absorption. The telluric absorption lines can be separated from lines that are from W3 IRS 5 thanks to the Doppler shifts (Table 1). Ideally, removing telluric absorption is done by taking a spectrum of a featureless hot star immediately before or after the target observation. This method also has the advantage of removing instrumental baseline effects, such as fringing, present in both spectra. Unfortunately, it was impractical to schedule calibrators for every part of the W3 IRS 5 survey due to the limitations of airborne observation scheduling and the scarcity of bright standard stars. Only one survey setting was observed with the adjacent calibrator star Sirius (7.28–7.46 μm; see Table 1). Thus, we relied on atmospheric transmittance models created with the Planetary Spectrum Generator (PSG; Villanueva et al. 2018) and tuned the H_2O column and pressure for the longitude, latitude, and altitude of the observations (Appendix A) to remove telluric features, including minor features that may overlap with water lines from W3 IRS 5. The quality of these corrections was verified by telluric lines not overlapping with W3IRS5 lines. To establish the reliability of the construction procedure of the PSG models, we compared the Sirius spectrum with the PSG model built from 7.28–7.46 μm (see Appendix B). We conclude that the telluric correction yields uncertainties on the equivalent widths at the level of 10%. After the PSG models are divided, further data reduction such as removing the local baseline is still conducted.

Since the distance between the binary (1$''$.2) is smaller than the SOFIA PSF (∼3$''$–3$''$.5), W3 IRS 5 is not spatially resolved in the observed spectra. As both sources contribute to the observed flux in our slit, the derived equivalent width of an absorption associated with one IR source will be diminished by the continuum emission from the other source. The two sources have very comparable MIR

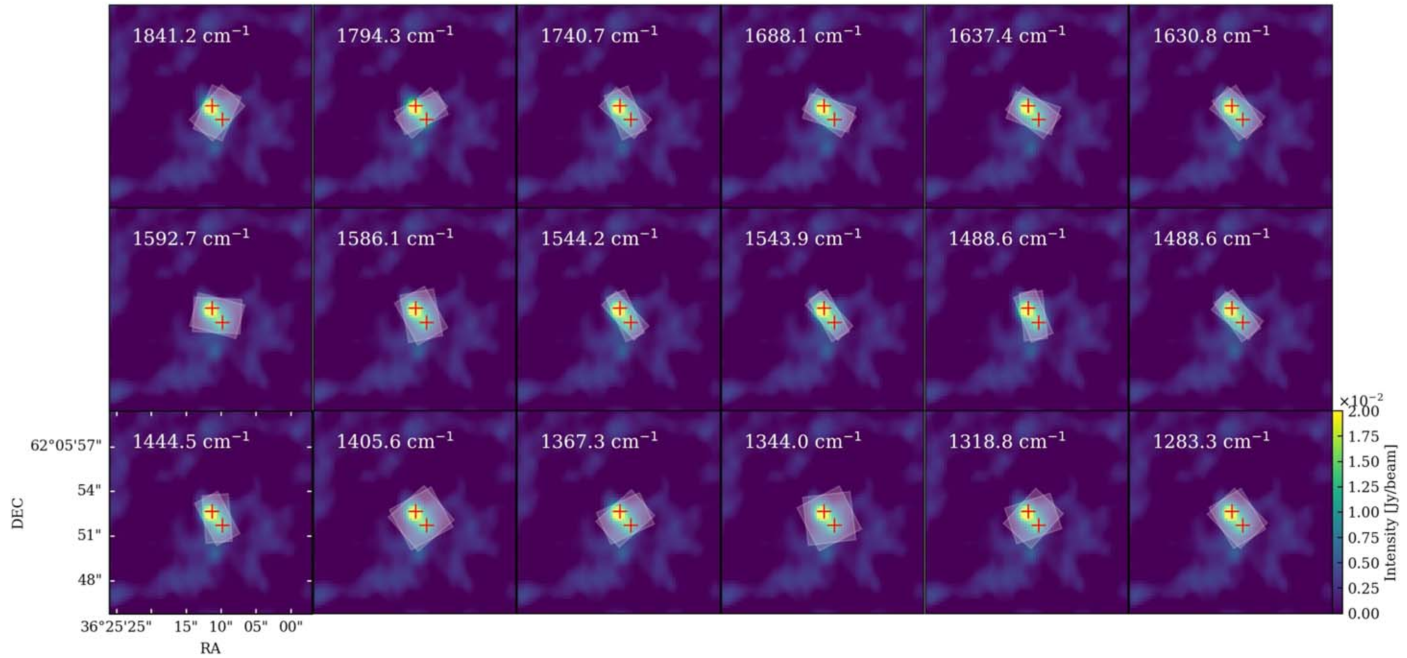

Figure 1. Slit coverage (white rectangles) on top of W3 IRS 5 at different observational settings. Only the initial and final positions are plotted in the figure. The range of the position angles is listed in Table 1. The three settings centered at 1405.6, 1344.0, and 1318.8 cm^{-1} are the archival data. The background is the PdBI 3.4 mm image of W3 IRS 5 adopted from Rodón et al. (2008), and the two red crosses (R.A.: 02 25 40.68, decl.: 62 05 51.53 and R.A.: 02 25 40.78, decl.: 62 05 52.47; van der Tak et al. 2005) mark the positions of the protobinary stars.

Table 1
Observational Parameters

Source (1)	Date (UT) (2)	Time (UT) (3)	$\mathrm{WN}_{\mathrm{cen}}$ (cm^{-1}) (4)	λ (μm) (5)	v_{geo} (km s^{-1}) (6)	Long. (deg) (7)	Lat. (deg) (8)	Alt. (feet) (9)	ZA (deg) (10)	Slit Height ($''$) (11)	PA (°) (12)
W3 IRS 5	2022-02-24	09:01:10	1841.2	5.36–5.51	−20.8	−117.11	49.11	41772	63.97	2.11	293.3–312.5
	2021-12-04	08:57:30	1794.3	5.48–5.67	−36.8	−124.41	29.93	43072	46.06	1.74	318.3–335.2
	2021-12-04	08:01:15	1740.7	5.65–5.84	−36.8	−132.92	26.80	43075	40.21	1.74	42.4–67.3
	2021-12-02	06:46:07	1688.1	5.83–6.02	−37.5	−91.80	34.73	41513	40.66	1.74	17.4–36.3
	2021-12-01	07:26:18	1637.4	6.01–6.20	−37.9	−104.60	38.89	40113	35.51	1.93	19.9–37.7
	2021-06-16	07:11:54	1630.8	6.01–6.20	−51.5	−98.82	45.37	42475	62.47	1.93	219.1–236.0
	2021-06-16	06:00:33	1592.7	6.18–6.37	−51.5	−113.11	48.40	41056	67.76	2.31	240.7–259.0
	2021-12-01	08:10:29	1586.1	6.19–6.37	−37.9	−98.06	41.39	40607	40.87	2.31	3.1–14.8
	2021-06-11	19:37:02	1544.2	6.35–6.61	−50.1	−111.17	48.82	41004	61.99	1.36	226.9–245.3
	2021-06-18	06:40:39	1543.9	6.35–6.61	−52.1	−100.56	45.11	41079	64.06	1.36	226.9–241.5
	2021-06-10	19:55:04	1488.6	6.59–6.85	−49.7	−98.07	45.88	42010	59.82	1.56	218.1–234.1
	2021-06-18	05:37:44	1488.6	6.59–6.85	−52.1	−114.09	47.81	41002	67.61	1.55	247.8–263.7
	2021-06-09	18:45:41	1444.5	6.79–7.06	−49.4	−123.32	51.26	41023	64.68	1.75	242.2–265.1
	2020-02-06[a]	08:38:37	1405.6	7.02–7.21	−21.0	−126.47	46.66	43007	55.00	3.06	318.7–331.3
	2022-02-24	07:53:55	1367.3	7.19–7.45	−20.8	−131.46	45.93	40589	57.87	2.33	318.3–335.2
	2018-10-31[b]	03:26:20	1344.0	7.34–7.52	−49.4	−102.79	33.33	38020	39.28	3.25	152.7–173.0
	2020-02-07[a]	09:10:52	1318.8	7.49–7.68	−21.0	−152.16	49.01	41024	45.90	3.43	312.5–341.6
	2021-06-09	20:06:39	1283.3	7.67–7.92	−49.4	−107.06	48.97	43011	59.73	2.51	226.3–238.9
Sirius	2022-02-24	06:45:01	1367.3	7.18–7.46	⋯	−135.36	41.32	39098	62.13	⋯	⋯

Notes. Column (1): Sirius is the standard star for the observation session on 2022-02-24 at 7.19–7.45 μm. Column (4): the central wavenumber of the setting. Column (6): the Earth's Doppler velocity with respect to W3 IRS 5 at the time of the observation. Columns (7)–(10): the longitude, latitude, altitude, and zenith angle of the telescope of the observation session. Columns (11)–(12): the height and the position angle (from north to east) of the slit. Note that the shortest slit height ($1\overset{\prime\prime}{.}36$) is longer than the distance between the binary of W3 IRS 5 ($1\overset{\prime\prime}{.}2$). For all settings, the slit width is fixed to $3\overset{\prime\prime}{.}2$.

[a] Archival data (AOR_ID: 07_0063).

[b] Archival data (AOR_ID: 76_0004).

brightness (see the SpeX observations in Li et al. 2022), and we include a factor of 2 in our analysis to account for this effect throughout this study unless otherwise stated. In other words, we think the relative absorption depth should be two times deeper because the continuum level should be two times weaker. It should be mentioned that the actual contribution of the nonabsorbing source will depend on the slit orientation over the source, and this changes slightly between the different grating settings (see Figure 1). We have decided to accept this additional source of uncertainty to the results in view of the uncertain brightness distribution of the two sources on the sky.

3. Data Analysis

By comparing with the spectra constructed via the existing laboratory line information (HITRAN; Rothman et al. 2013) and LTE models, we identified over 180 H_2O $\nu_2 = 1$–0 and about 90 H_2O $\nu_2 = 2$–1 absorption lines in this survey. As shown in Figure 2, the velocity ranges of the absorbing components are very similar to those present in ^{13}CO or in high-J ^{12}CO lines (Li et al. 2022). All components are blueshifted compared to or are located at the cloud velocity $v_{\rm LSR} = -38$ km s^{-1} (van der Tak et al. 2000). Each kinematic component is characterized by different excitation conditions.

We fit the $\nu_2 = 1$–0 absorption line profiles with a sum of multiple Gaussians indicated as the ith component in the form of

$$\frac{I_{\rm obs}(v)}{I_c} = 1 - \sum_i \frac{W_i}{\sigma_{v,i}\sqrt{2\pi}} \exp\left(-\frac{1}{2}\frac{(v - v_{{\rm LSR},i})^2}{\sigma_{v,i}^2}\right) \quad (1)$$

using the `curve_fit` function in `scipy`. In Equation (1), $I_{\rm obs}(v)$ is the observed line intensity profile in the velocity space, I_c is the intensity of the continuum, W_i is the area or the equivalent depth of the Gaussian component, $\sigma_{v,i}$ is the standard deviation, and $v_{{\rm cen},i}$ is the center velocity of the component. The fitting results are determined by restricting the range of the free parameters. Specifically, two components centered at ~ -39.5 km s^{-1} and -54.5 km s^{-1} are present across all energy levels, while the component centered at -45 km s^{-1} only appears in transitions originating from relatively low-energy states (<800 K). As we will explain in Section 3.1, we name the three components at ~ -39.5 km s^{-1}, -45 km s^{-1}, and -54.5 km s^{-1} as "H1," "W," and "H2." For very-low-energy states (<200 K), an extra component at -39.5 km s^{-1} is possibly needed for a better fitting result (see Appendix C), and we discuss its existence and the implications in Section 5.1.

We therefore fit two and three Gaussians above and below 800 K, separately. Above 800 K, we constrain the velocity center to -43 to -36 km s^{-1} for the "H1" component, and the "H2" component with a relative velocity of -17 to -14 km s^{-1} guided by an initial guess. The line widths, σ_v, were constrained to 4–6 and 7–9 km s^{-1}. We apply the same constraints to the $\nu_2 = 2$–1 absorption line profiles. On the other hand, we think the profiles of the low-energy transitions (<800 K) are a blend of more than two components, including the rather weak "W" and "H2" components. After a careful assessment, we decided to limit the number of free parameters in the fit to these transitions as, from a physical perspective, we expect that transitions from a given temperature component will occur at consistent central velocities. We keep using a range for the velocity dispersion in the fitting procedure as we did for the high-energy transitions. More specifically, for the low-energy transitions, we fix the rather weak "W" and "H2" with the central velocity, $v_{\rm LSR}$, of -45 and -54.5 km s^{-1}, and the velocity dispersion parameter, σ_v, from 4–5 km s^{-1}. We note that the H2 (-54.5 km s^{-1}) component disappears in some of the low-energy transitions (see the second panel in Figure 2) as a result of the opacity effect (see Section 3.1). In this case, we only fit the line profile with one Gaussian for the "H1" component. We list in Appendix E in detail the parameters of each individual component such as the central velocity, velocity width, and equivalent widths, and report "H1" as -39.1 ± 2.4 km s^{-1}, and "H2" (>800 K) as -54.1 ± 3.0 km s^{-1}, respectively.

3.1. Rotation Diagram Analysis and the Opacity Problem

After the distinct velocity components are determined, we use a rotation diagram to provide a first view of their characteristics. If the absorption lines are optically thin, we can get the column density N_l in the lower state of a transition directly from the integrated line profile by

$$N_l = 8\pi/(A_{ul}\lambda^3) g_l/g_u \int \tau(v) dv, \quad (2)$$

in which λ is the wavelength, A_{ul} is the Einstein A coefficient, g_l and g_u are the statistical weight of the lower and upper levels, v is the velocity, and

$$\tau(v) = -\ln(I_v/I_c), \quad (3)$$

where I_v and I_c are the intensity of the absorption line and the continuum, and I_v of each identified velocity component in a given transition is derived from the Gaussian fitting parameters (Equation (1)). All spectral line parameters used in this study are adopted from HITRAN (Rothman et al. 2013).

If the foreground absorbing gas is in LTE, the population of one rotational level can be described with the Boltzmann equation (Goldsmith & Langer 1999),

$$\frac{N_l}{g_l} = \frac{N_{\rm tot}}{Q(T_{\rm ex})} \exp\left(-\frac{\Delta E_l}{k_B T_{\rm ex}}\right), \quad (4)$$

in which $T_{\rm ex}$ is the excitation temperature, $N_{\rm tot}$ is the total column density, ΔE_l is the relative energy between the excitation state and the ground state energy of the vibration state, and is equal to E_l for $\nu_2 = 1$–0 transitions.[12] $Q(T_{\rm ex})$ is the partition function, and k_B is the Boltzmann constant. Specifically, $\ln(N_l/g_l)$ and E_l/k_B of all absorption lines constructs the so-called rotation diagram. For a uniform excitation temperature, $\ln(N_l/g_l)$ and E_l/k_B fall on a straight line. The inverse of the slope represents the temperature, and the intercept represents the total column density over the partition function.

We present the rotation diagrams of the rovibrational H_2O lines from W3 IRS 5 in Figure 3. For the three velocity components centered at -39.5, -45, and -54.5 km s^{-1} identified in $\nu_2 = 1$–0 transitions, the derived temperatures are 807 ± 58, 200 ± 18, and 669 ± 57 K (Table 2). The three components are hence named "H1," "W," and "H2," in which "W" and "H" stand for "warm" and "hot," respectively, following the nomenclature in Li et al. (2022). For $\nu_2 = 2$–1 transitions, only the components "H1" and "H2" at -39.5 and -54.5 km s^{-1} are identified, and the derived temperatures are 703 ± 60 and 946 ± 170 K (Table 2).[13]

The derived total column densities of "H1," "W," and "H2" in the $\nu_2 = 0$ state are $(1.2 \pm 0.6) \times 10^{18}$, $(3.3 \pm 2.0) \times 10^{17}$, and $(6.2 \pm 3.4) \times 10^{17}$ cm^{-2}, respectively (Table 2). However, it is noticeable that the large scatter in the rotation diagram

---

[12] For $\nu_2 = 2$–1 transition, ΔE_l is relative to the ground state energy of $\nu_2 = 1$ ($J_{K_a,K_c} = 0_{0,0}$, 2294.7 K).

[13] The derived temperature of "W" of ~200 K from the $\nu_2 = 1$–0 transitions explains the nondetection of "W" in the $\nu_2 = 2$–1 transition. According to Equation (16), the column density of "W" is expected to be 3 orders of magnitude weaker than that of "H1" and "H2" in ~600 K.

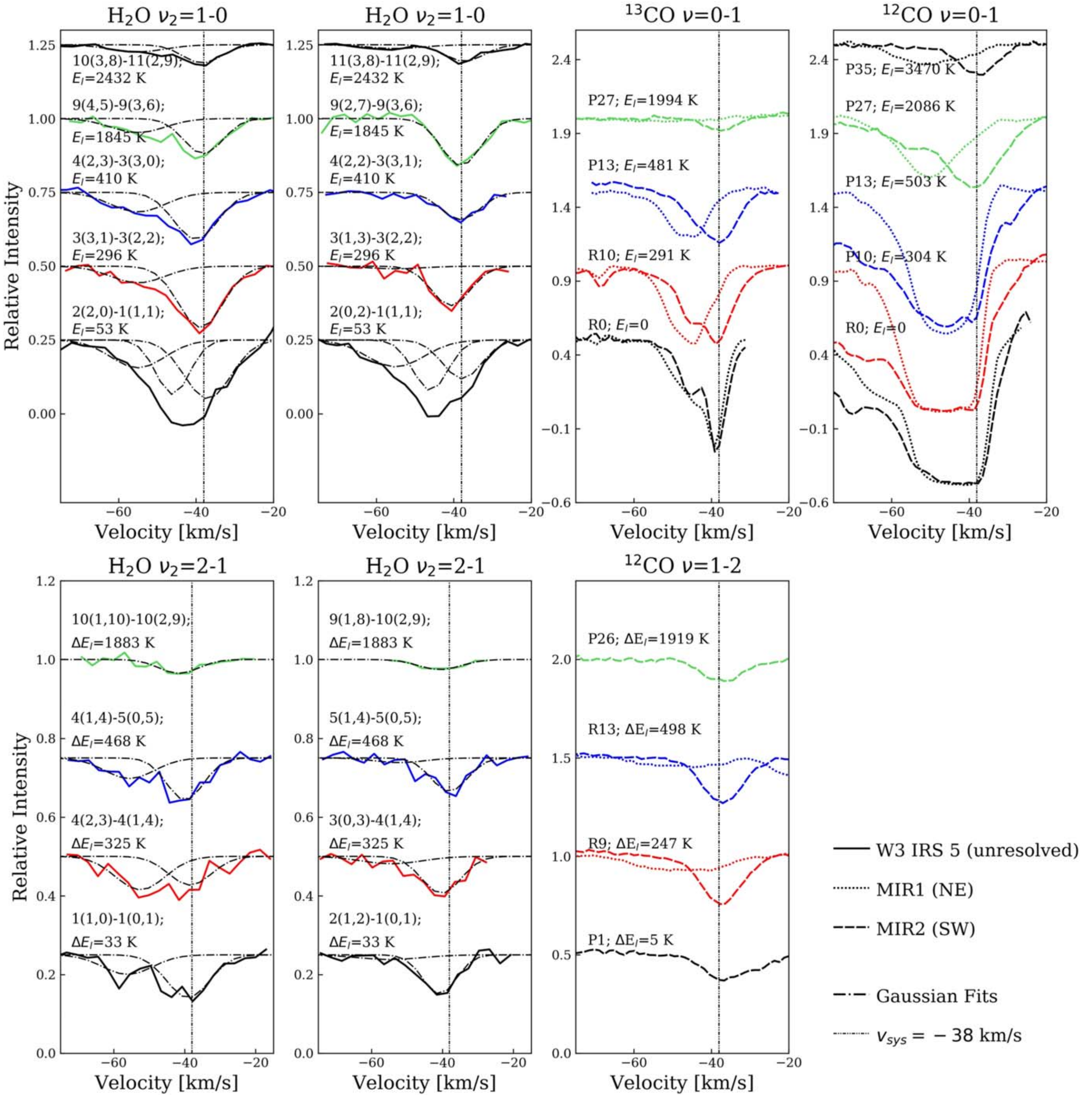

Figure 2. Selected H$_2$O $\nu_2 = 1$–0, H$_2$O $\nu_2 = 2$–1 (from this study), ^{13}CO $\nu = 0$–1, ^{12}CO $\nu = 0$–1, and ^{12}CO $\nu = 1$–2 (adopted from Li et al. 2022) absorption lines observed toward W3 IRS 5. This binary, consisting of sources MIR1 and MIR2, is spatially resolved in ground-based IRTF studies of CO, and their observed line profiles are indicated by dotted and dashed lines. MIR1 and MIR2 are not spatially resolved in the H$_2$O observations on SOFIA. However, the high spectral resolution of these observations assists in the disentanglement of MIR1 and MIR2. The dashed vertical lines at −38 km s^{-1} are the systematic velocity. Across the panels, transitions with similar energy levels are represented by the same color. For vibrationally excited states, ΔE_l is the energy difference relative to the ground state energy of $\nu_2 = 1$ for water or $\nu = 1$ for CO. Distinct kinematic components in H$_2$O transitions are present under different excitation conditions. Gaussian fitting profiles on top of H$_2$O lines are centered at −54.5 ("H2"), −45 ("W"), and −39.5 ("H1") km s^{-1} (see Section 3 for the nomenclature). We note that H$_2$O line profiles can originate from states with comparable energies and yet may differ significantly in their line profiles due to the opacity effect (see Section 3.1).

exceeds what the error bars can account for in components H1 and H2. Specifically, as shown in Figure 3, for transitions that share the same lower state (and the same g_l), the difference in the derived N_l is up to an order of magnitude.

We can further illustrate this problem by directly comparing the line profiles of the transitions that have a common lower energy level, and present such a comparison in Figures 2 and 4. As shown in Figures 2 and 4, lines that share the same lower level but different oscillator strength (f_{ul}) or Einstein A do not necessarily have the same absorption intensity and/or the equivalent width, which is defined as

$$W_\nu = \int (1 - I_\nu/I_c) d\nu \qquad (5)$$

in the frequency space. This behavior where transitions with high values of Einstein A fall systematically below the relation

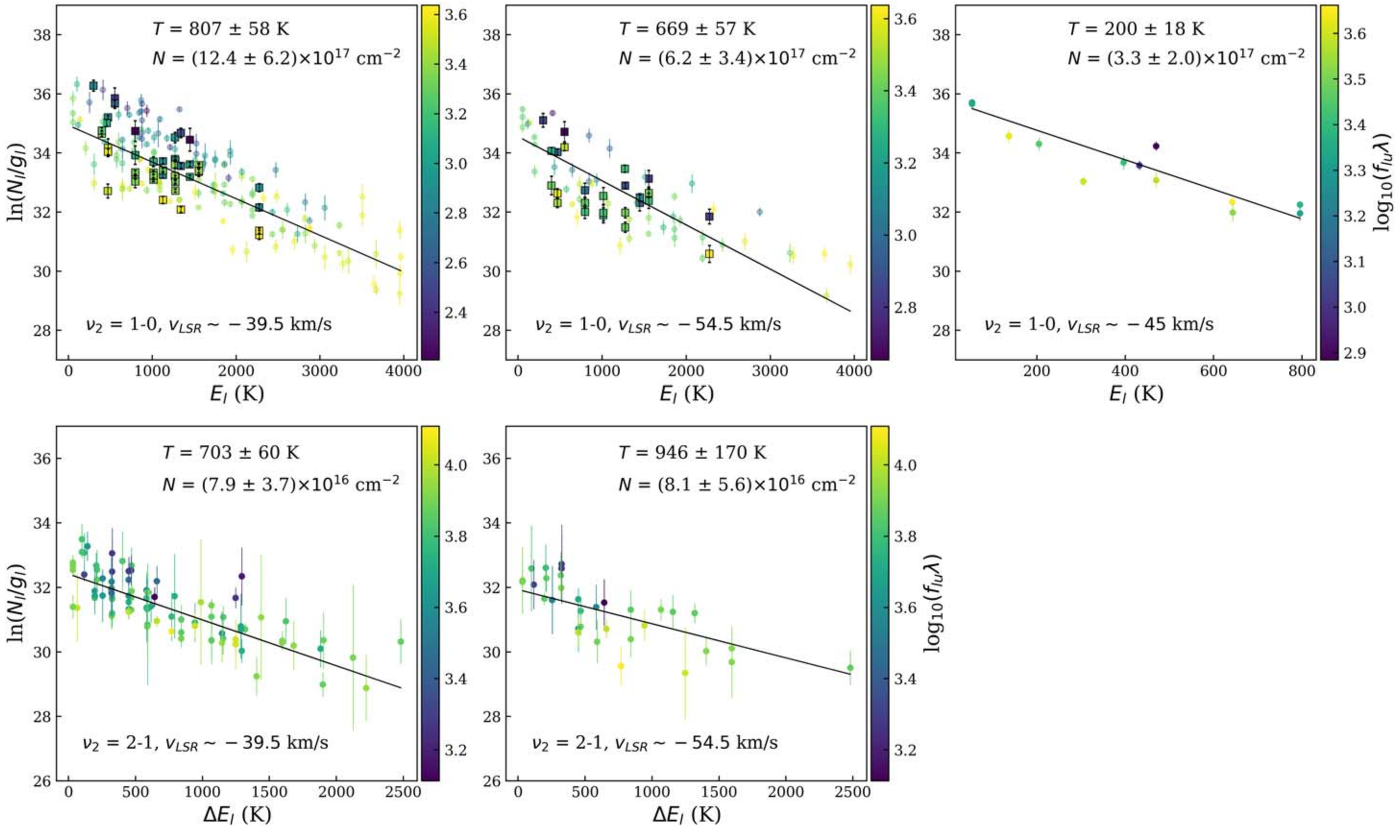

Figure 3. Rotation diagrams of H_2O $\nu_2 = 1$–0 (upper panels) and $\nu_2 = 2$–1 (lower panels) transitions from the decomposed velocity components: −39.5 (“H1”), −45 (“W”), and −54.5 (“H2”) km s^{-1}. For $\nu_2 = 2$–1 transitions, E_l in the x-axis are ΔE_l relative to the ground state energy of $\nu_2 = 1$ ($J_{K_a,K_c} = 0_{0,0}$, 2294.7 K). Square data points represent a collection of lines that share the same lower level as shown in Figure 4. The N_l are derived from Equation (2) with Gaussian fitting on the line profiles assuming optically thin absorption. The color code is log $_{10}(f_{lu}\lambda)$, which is representative of the intrinsic strength (see Section 3.2). The parameter f_{lu} is the oscillator strength, and λ is the wavelength.

Table 2
Physical Conditions of Decomposed Components

Component	“W,” −45 km s^{-1}	“H1,” −39.5 km s^{-1}		“H2,” −54.5 km s^{-1}	
Transitions	$\nu_2 = 1$–0	$\nu_2 = 1$–0	$\nu_2 = 2$–1	$\nu_2 = 1$–0	$\nu_2 = 2$–1
			Rotation Diagram		
$T_{\rm ex}$ (K)	200 ± 18	807 ± 58	703 ± 60	669 ± 57	946 ± 170
$N_{\rm tot}$ (cm^{-2})	$(6.6 \pm 4.0) \times 10^{17}$[a]	$(1.2 \pm 0.6) \times 10^{18}$	$(7.9 \pm 3.7) \times 10^{16}$	$(6.2 \pm 3.4) \times 10^{17}$	$(8.1 \pm 5.6) \times 10^{16}$
			Slab Model		
f_c	…	0.4	0.4	0.3	…
b (km s^{-1})	…	2.8	2.8	3.5	…
$T_{\rm ex}$ (K)	…	471^{+14}_{-15}	654^{+135}_{-191}	600^{+28}_{-27}	…
$N_{\rm tot}$ (cm^{-2})	…	$2.5^{+0.3}_{-0.2} \times 10^{19}$	$2.8^{+0.5}_{-0.7} \times 10^{17}$	$5.3^{+0.3}_{-0.6} \times 10^{18}$	…
$\chi^2_{r,min}$	..	1.7	0.65	3.8	…
			Disk Model[b]		
b (km s^{-1})	…	2.8	2.8	3.5	…
$T_{\rm ex}$	…	491^{+13}_{-14}	691^{+122}_{-212}	612^{+27}_{-30}	…
Abun. (w.r.t H)	…	$2.6^{+0.1}_{-0.2} \times 10^{-3}$	$5.0^{+1.4}_{-3.5} \times 10^{-5}$	$5.1^{+0.4}_{-0.5} \times 10^{-4}$	…
$\chi^2_{r,min}$	…	1.7	0.34	2.3	…

Notes.

[a] This value is corrected by assuming that “W” covers protobinary and that the absorption intensity is not diluted (see Section 4.2).

[b] Pure absorption with parameter ϵ of 1 is assumed in this table. See Table 3 for results with an ϵ of 0 and 0.5.

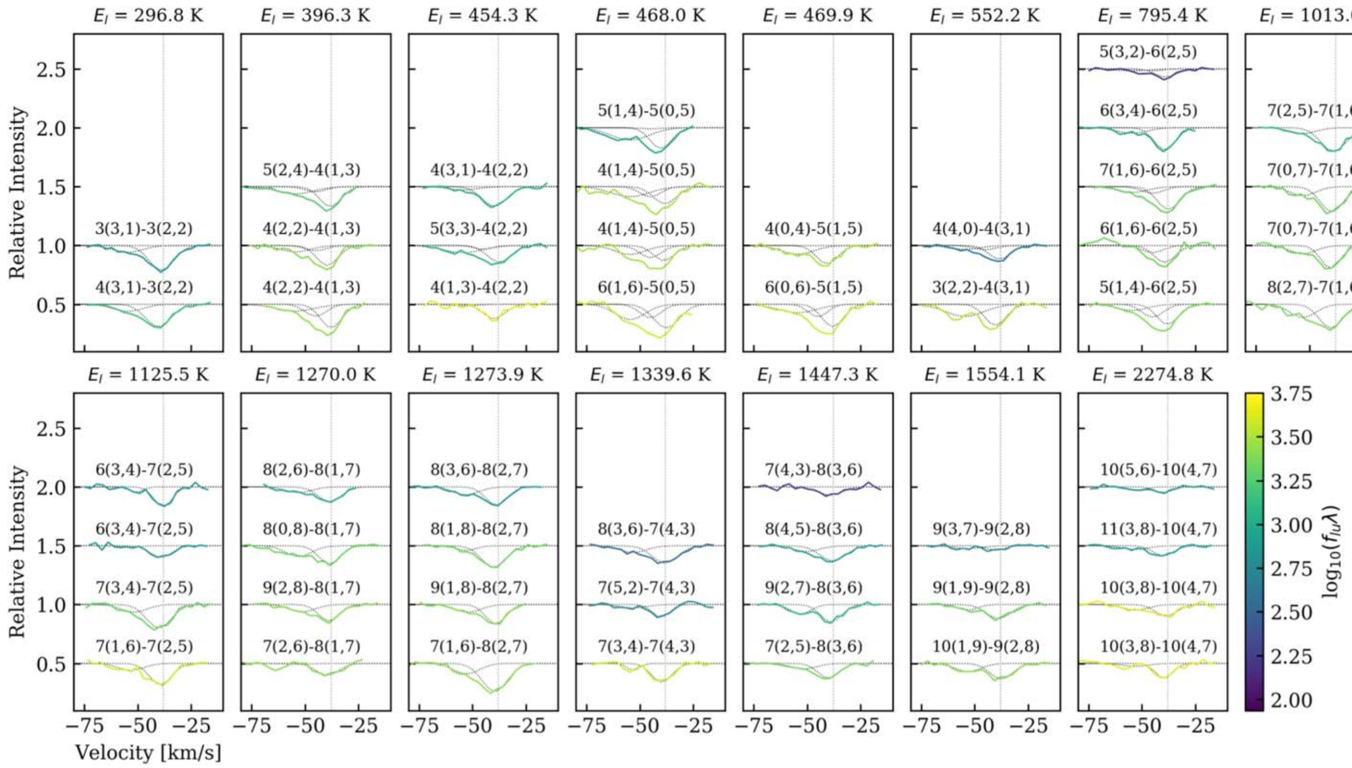

Figure 4. Selected H_2O $\nu_2 = 1$–0 absorption lines observed toward W3 IRS 5. In each panel, all rovibrational lines share the same lower energy state, and thus column density. But, while the intrinsic strength, $\log(f_{lu}\lambda)$, increases from top to bottom, the equivalent width often does not, indicating that the lines are optically thick. Some transitions appear in more than one setting and result in duplicated entries in the figure. The line profiles are color-coded following the color bar in Figure 3 (see Section 3.2), and are listed in each panel from top to bottom with increasing $\log_{10}(f_{lu}\lambda)$, which is representative of the opacity. Gaussian fitting in dotted lines for "H1" and "H2" components at $E_l > 800$ K (for "W," "H1," and "H2" at $E_l < 800$ K) are presented together with each absorption line. The dashed vertical lines at $-38\ \mathrm{km\ s^{-1}}$ indicate the systematic velocity of W3 IRS 5 (van der Tak et al. 2000).

provided by transitions with low values of Einstein A in the rotation diagram (Figure 3) is characteristic for opacity effects. Specifically, when transitions are optically thick, an increase in absorption strength (due to an increase in Einstein A) results in only a small increase in line width (not in depth) and hence marginally increases the equivalent width. This effect was noted earlier in Indriolo et al. (2020) and Barr et al. (2022a) in studies of MIR H_2O rovibrational lines toward massive protostars AFGL 2136 and AFGL 2591.

3.2. Curve-of-growth Analysis

Considering that $\tau(v)$ in Equation (2) does not represent an optically thin Gaussian core, the definition of the equivalent width in Equation (5) can be written as

$$\begin{aligned} W_\nu &= \int (1 - I_\nu/I_c)\,d\nu \\ &= \int (1 - \mathrm{e}^{-\tau(\nu)})\,d\nu \\ &= \int (1 - \mathrm{e}^{-\tau_p H(a,v)})\,d\nu \end{aligned} \tag{6}$$

in which the integration is over the frequency ν. The Voigt profile $H(a,\ v)$ is defined as (Equations (9)–(34) in Mihalas 1978):

$$H(a,\ v) = \frac{a}{\pi}\int_{-\infty}^{+\infty}\frac{e^{-y^2}dy}{(v - y)^2 + a^2}. \tag{7}$$

The parameter, v, is defined as

$$v = \frac{\nu - \nu_0}{\Delta\nu_D} \tag{8}$$

and represents the shift from the line center in Doppler units. $\Delta\nu_D$ is the Doppler width in frequency space. The parameter a is the damping factor. The peak optical depth τ_p is

$$\tau_p = \frac{\sqrt{\pi}\,e^2}{m_e bc}N_l f_{lu}\,\lambda. \tag{9}$$

In Equation (9), e is the electron charge, m_e is the electron mass, c is the speed of light, and f_{lu} is the oscillator strength. The Doppler parameter in velocity space, b, is related to the FWHM of an optically thin line by $\Delta v_{\mathrm{FWHM}} = 2\sqrt{\ln 2}\,b$.

Equation (9) clearly shows that for lines that share the same lower level and have the same N_l, a difference in $f_{lu}\lambda$ will lead to different τ_p. Defining $\log_{10}(f_{lu}\lambda)$ as the representative for the line strength, lines with a larger line strength have larger equivalent widths (as shown in Figure 4), and as a result, the N_l derived via Equation (2) will be underestimated (as shown in Figure 3).

3.2.1. Slab Model of a Foreground Cloud

A curve-of-growth analysis (Rodgers & Williams 1974) is required to reconcile the opacity problem and to correctly derive N_l and $N_{\rm tot}$ (Equation (9.27) in Draine 2011):

$$\frac{W_\lambda}{\lambda}\approx \begin{cases} \dfrac{\sqrt{\pi}\,b}{c}\dfrac{\tau_p}{1+\tau_p/(2\sqrt{2})} & \text{for } \tau < 1.254 \\ \dfrac{2b}{c}\sqrt{\ln(\tau_p/\ln 2)+\dfrac{\gamma\lambda}{4b\sqrt{\pi}}(\tau_p-1.254)} & \text{for } \tau > 1.254 \end{cases}. \tag{10}$$

We specifically note that this correction applies to an absorbing foreground slab model. In the equations above, the definitions of all parameters follow Equation (9). The parameter γ is the damping constant of the Lorentzian profile and is of the order of 10 for radiative damping. We stress that for H_2O lines discussed in this paper, the Lorentzian line width that γ corresponds to is 10^{-9} km s^{-1}, and is negligible compared to the observed Doppler width (a few kilometeres per second).

For such an absorbing slab model, the emission from the foreground is negligible against the representative background temperature of ∼600 K in this study (see Li et al. 2022). Furthermore, if the foreground cloud does not cover the entire observing beam, a covering factor f_c $(0 \leqslant f_c \leqslant 1)$ has to be accounted for, and Equation (3) is modified to:

$$I_\nu = I_{\rm c}(1 - f_c(1 - {\rm e}^{-\tau(\nu)})), \tag{11}$$

and the left-hand side of the Equation (10) is modified to $W_\lambda/(\lambda f_c)$.

3.2.2. Stellar Atmosphere Model of a Circumstellar Disk

The absorption can also occur in an accretion disk scenario in the system of a forming massive star (Barr et al. 2020, 2022a; Li et al. 2022). Specifically, the disk has an outward-decreasing temperature gradient from the mid-plane to the surface. Such disks show absorption lines because the thermal continuum from the dust is mixed with the molecular gas. For such a scenario, we adopt the curve-of-growth of the stellar atmosphere model in which the continuum and the line opacities are coupled. The residual flux,

$$R_\nu \equiv I_\nu / I_c, \tag{12}$$

where I_ν is the intensity of the absorption line, can then be approximated by the Milne-Eddington model (Mihalas 1978) which assumes a gray atmosphere. The absorption line profile may originate in pure absorption or scattering. The parameter ϵ characterizes the line formation, and can take the form of 1 (pure absorption), 0 (pure scattering), or between 0 and 1 (a combination of scattering and absorption). We refer to Appendix A in Barr et al. (2020) for details of the line residual flux expected from this model.

The curve of growth in the stellar atmosphere model is constructed via the equivalent width versus β_0, the ratio of the line opacity at the line center, $\kappa_L(\nu = \nu_0)$, to the continuum opacity κ_c:

$$\frac{W_\nu}{2\Delta\nu_D} = \int_0^{+\infty}(1 - R_\nu)dv = A_0\int_0^{+\infty}\beta_0 H(a, v)[1 + \beta_0 H(a, v)]^{-1}dv, \tag{13}$$

in which

$$\beta_0 = \frac{\kappa_L(\nu = \nu_0)}{\kappa_c} = \frac{A_{ul}\lambda^3}{8\pi\sqrt{2\pi}\,\sigma_v}\frac{g_u}{g_l}\frac{N_l}{\sigma_c N_H}\left(1 - \frac{g_l}{g_u}\frac{N_u}{N_l}\right), \tag{14}$$

where we have used the continuum opacity, κ_c, equal $\sigma_c N_H$ where σ_c is the dust cross section per H atom, $H(a, v)$ is the Voigt function that gives the line profile in velocity space, and v is defined as the velocity shift with respect to the line center in units of the Doppler width (see Equation (7)). The damping factor $a = \gamma\lambda/b$ is of the order of 10^{-8} for H_2O rovibrational lines. The parameter A_0 is the central depth of an opaque line. Its exact value is determined by the radiative transfer model of the surface of the disk and is related to the gradient of the Planck function. For a gray atmosphere and lines in pure absorption, A_0 is ∼0.5–0.9 from 900–100 K (see Appendix A in Barr et al. 2020). The dispersion in velocity space, σ_v , is transformed from the Doppler parameter, $b/\sqrt{2}$, with which we convert W_ν to the velocity space:

$$\frac{W_\nu}{2\Delta\nu_D} = \frac{W_v}{2b}. \tag{15}$$

We can disregard the bracketed item in Equation (14) if stimulated emission is negligible.

We adopt a value of 7×10^{-23} cm^2/H-nucleus for σ_c following Barr et al. (2020), as it is appropriate for coagulated interstellar dust (Ormel et al. 2011). Theoretical fits to these curves of growth will provide abundances relative to the dust opacity. As this value of σ_c is adopted in the CO analysis (Li et al. 2022) as well, we are able to derive an absolute water-to-CO ratio once the CO correspondent component to water is identified via the kinematic information (see Section 4.2).

4. Results

As shown in Section 3, the H_2O $\nu_2 = 1$–0 lines are decomposed into three velocity components at −45, − 39.5, and −54.5 km s^{-1}, while the $\nu_2 = 2$–1 absorption lines are decomposed into two components at −39.5 and −54.5 km s^{-1}. The components at the three different velocities, as explained in Section 3.1, are labeled as “W,” “H1,” and “H2” based on the preliminary estimation of their temperatures derived from the rotation diagram analysis under the optically thin assumption (Table 2).

We hereafter apply the curve-of-growth analyses to the $\nu_2 = 1$–0 transitions from “H1 and ‘H2” and $\nu_2 = 2$–1 from “H1.” The rotation diagrams of the three sets of transitions illustrate a large scatter indicative of the opacity problem discussed in Section 4.1, unlike for the other components and transitions. In Section 4.2, all of the water components are compared to and connected with warm and/or hot CO components. The implications of the vibrationally excited water lines are presented in Section 5.1.2.

4.1. Two Hot Physical Components: H1 and H2

We conduct the grid-search method (Li et al. 2022) on the ($T_{\rm ex}$, $N_{\rm tot}$) and ($T_{\rm ex}$, abundance) grid in the curve-of-growth analyses for the slab model and the disk model, respectively. For the slab model, $T_{\rm ex}$ together with $N_{\rm tot}$ determines τ_p, or $Nf_{ul}\lambda$ (Equation 10). We, therefore, search for the parameter

Table 3
Results of the Physical Component "H1" Derived from Different ϵ and σ_v in the Disk Model

	$\epsilon = 0$			$\epsilon = 0.5$			$\epsilon = 1$		
	$\chi^2_{r,min}$	T_{ex} (K)	X_{H_2O}/X_{CO}	$\chi^2_{r,min}$	T_{ex} (K)	X_{H_2O}/X_{CO}	$\chi^2_{r,min}$	T_{ex} (K)	X_{H_2O}/X_{CO}
$\sigma_v = 1.5$ km s^{-1}	2.02	579	1.19	1.79	449	2.45	1.88	419	3.71
$\sigma_v = 2.0$ km s^{-1}	2.54	565	0.78	1.84	510	1.30	1.73	491	1.53
$\sigma_v = 2.5$ km s^{-1}	3.14	598	0.61	1.99	560	0.90	1.88	521	1.20
$\sigma_v = 3.0$ km s^{-1}	3.72	622	0.52	2.37	594	0.72	1.98	564	0.92

Note. (1) The 1σ uncertainty for the derived temperatures is of the order of ±10 K. (2) X_{H_2O}/X_{CO} is derived by assuming that "H1" and "MIR2-H1" in CO coexist.

combination of (T_{ex}, N_{tot}) that gives the smallest reduced χ^2 between the observed equivalent width W_λ (in the wavelength space) and that derived from the theoretical curve of growth (Equation (10)). Similarly, for the disk model, T_{ex} together with the abundance (N/N_H) determines β_0, the ratio of the line opacity to the continuum opacity. We search for the best (T_{ex}, abundance) combination that gives the smallest reduced χ^2 between the observed equivalent width W_ν (in the frequency space) and that derived from the theoretical curve of growth (Equation (13)).

When fitting the observed W_λ/λ to the theoretical curve-of-growth of a slab model, we note that the partial coverage, f_c, and the Doppler width, b ($=\sqrt{2}\sigma_v$), are degenerated parameters. Different combinations of f_c and b can provide as good fitting results, and we illustrate this point below for a similar case in the disk model. Observational results can put constraints on the range of f_c and b to some extent. For example, f_c are constrained as ∼0.4, which is twice the lower limit of the line intensities, ∼0.2. The factor of 2 is because of the dilution effect—the effect that the absorption line is against the continuum contributed by both MIR sources in W3 IRS 5 (see Section 2). As for the Doppler width b, its lower limit can be constrained by the thermal line width, and for gas of 500 K, $\sigma_{th} = \sqrt{(k_B T)/(\mu m_H)} = 9.12 \times 10^{-2}$ km s^{-1} $(T/\mathrm{K})^{0.5}\mu^{-0.5}$ ≈ 0.5 km s^{-1}. The upper limit of b can be constrained by the observed line width, which is b convolved with the instrument resolution $\sigma_{res} = c/(2\sqrt{2\ln 2}R) = 2.5$ km s^{-1}.

For the disk model, there is also a dependence on the chosen line width b, and the degree of absorption relative to the scattering in the line ϵ. We illustrate this in a more quantitative way. Take the "H1" component as an example, as presented in Table 3, while the results of the temperature and abundance depend on the adopted σ_v and ϵ, combinations of different σ_v and ϵ may provide comparable $\chi^2_{r,min}$. Although we may have some control over σ_v, the value of ϵ is unconstrained. We, therefore, provide Table 3 as a reference for conditions when the lines are not due to pure absorption.

For "H1" and "H2," we therefore choose the partial coverage, f_c, to 0.4 and 0.3, and set the Doppler width b ($=\sqrt{2}\sigma_v$) to 2.8 and 3.5 km s^{-1}, separately, since the chosen values provides the smallest χ^2_r. For the $\nu_2 = 1$–0 transition, we present the best-fitting results of the "H1" component for both the foreground and disk model in Figure 5 (results of "H2" are presented in Figure 12 in Appendix D) and summarize the derived properties in Table 2, assuming that the lines are formed in pure absorption ($\epsilon = 0$). In either the slab or the disk model, about half of the data points are located on the logarithmic part of the curve-of-growth, confirming that the corresponding absorption lines are optically thick. In the slab model, the curve-of-growth analysis "corrects" the underestimated total column densities in the rotation diagram by factors of 21 and 9 for "H1" and "H2," respectively. The derived temperatures are lowered to 471 K and 600 K, respectively (Table 2). In the disk model, as relative abundances are derived, the correction in column densities is quantified once the connection between CO and water components is established (see Section 4.2). The derived temperatures from the disk model are comparable to those derived from the slab model (Table 2). As for the $\nu_2 = 2$–1 transition on "H1," the correction after the curve-of-growth analysis on the temperature and column density is insignificant (Figure 13 in Appendix D and Table 2), indicating that the optical depth effect is not severe.

4.2. Connecting the Absorbing Components of H_2O and CO

High spectral resolution *M*-band absorption spectroscopy (R = 88,100) toward W3 IRS 5 at 4.7 μm revealed multiple kinematic components in ^{12}CO and its isotopologues (Li et al. 2022). Specifically, IRTF/iSHELL spatially resolved the two protostars in W3 IRS 5. As CO lines also trace ambient gaseous components that absorb against the MIR background, building a connection between the components identified in H_2O and CO will help us to understand the origins of the gaseous H_2O components.

The velocity resolution of EXES (6 km s^{-1}) and iSHELL (3.4 km s^{-1}) enables the comparison between H_2O and CO components through their kinematic information. We note that we elected to link the observed H_2O and CO components through their similarity in velocity and temperature. The velocity width is not used for aiding the comparison because it is dependent on the optical depth and is degenerated with the column density (Table 3). We, therefore, present in Figure 6 the comparison between the absorption profiles and list in Table 4 the velocity and derived excitation temperature of components identified in the two species.

As the different velocity components are characterized by different excitation temperatures, both the profiles of the H_2O and CO spectra are averaged in low-energy (<400 K) and high-energy (>400 K) transitions. As we have described in Section 3, we identified three components centered at −39.5, −45, and −54.5 km s^{-1} ("H1," "W," and "H2") in low-energy transitions, and two centered at −39.5 and −54.5 km s^{-1} in high-energy transitions. We note that half of the transitions (6 of 12) with a −45 km/s component are at energies between 400 and 800 K.

In low-energy levels, both MIR1 and MIR2 have two components revealed in CO, with one centered at $v_{sys} = -38$ km s^{-1} (MIR1-C1 and MIR2-C1[14]), and the other centered at −46 km s^{-1} (MIR1-W1 and MIR2-W2). No low-energy CO components were found at −55 km s^{-1}. MIR1-C1

---

[14] Naming of each individual CO components is consistent with the nomenclature in Li et al. (2022). More specifically, each CO component has a prefix of either "MIR1-" or "MIR2-."

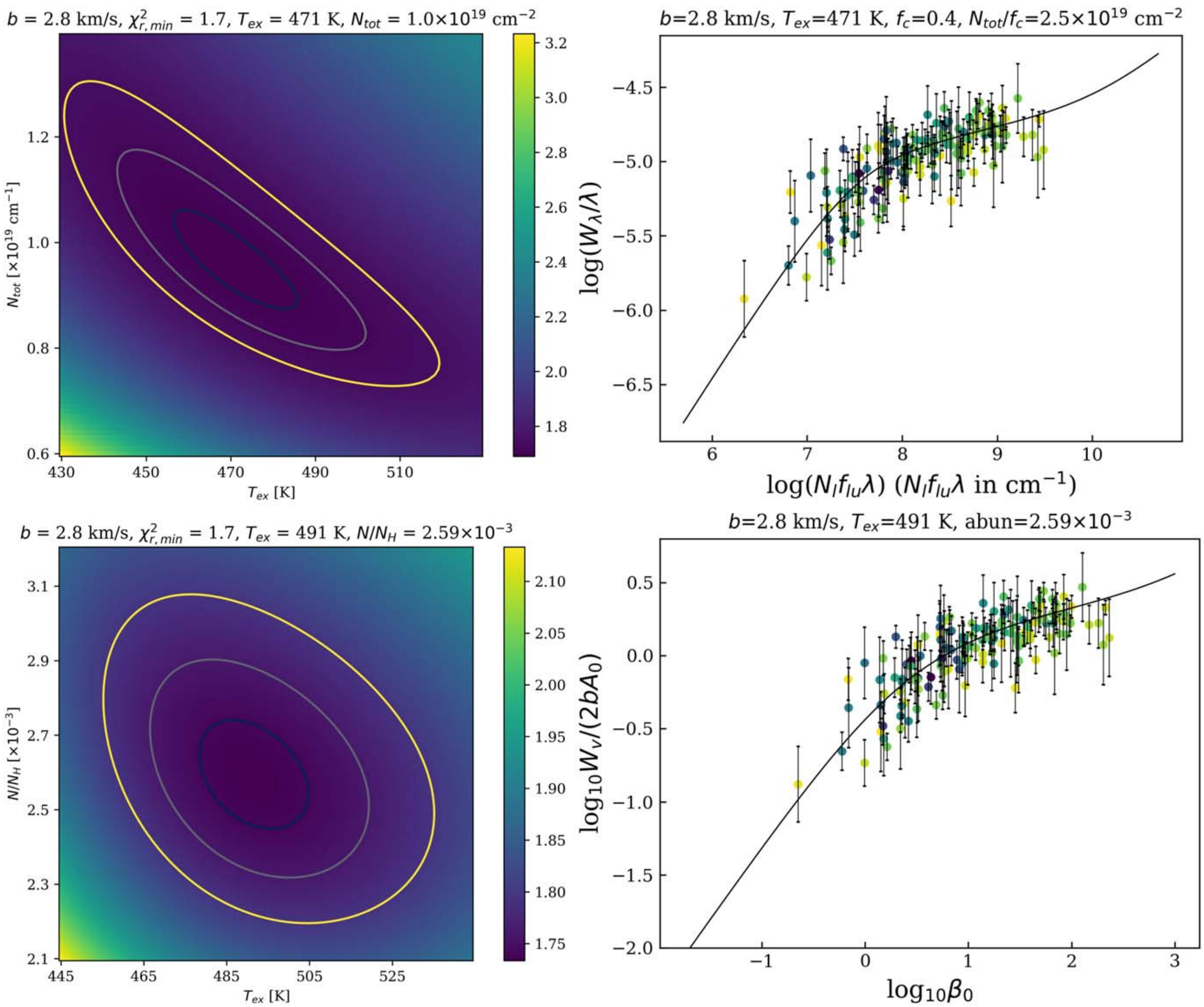

Figure 5. Curve of growth analysis for the slab (top) and disk (bottom) models for $\nu_2 = 1$–0 absorption lines from the "H1" component. Left panels: grid-search results for both the slab and the disk model illustrating the best-fitting results. The contours represent the 1σ, 2σ, and 3σ uncertainty levels. Right panels: the curves of growth for the slab and the disk model. The color scale of the data points is the same as that in the rotation diagram. Similar figures for the curve-of-growth analysis for $\nu_2 = 1$–0 transitions from the "H2" component, and $\nu_2 = 2$–1 transitions from the "H1" component, are presented in Figures 12 and 13, respectively.

and MIR2-C1, as well as MIR1-W1 and MIR2-W2, have similar temperatures and column densities (see Table 7 in Li et al. 2022; so do temperatures of CO components mentioned below), and are regarded to cover MIR1 and MIR2 simultaneously.

The temperatures of MIR1-C1 and MIR2-C1 are low (∼50 K). MIR1-C1 and MIR2-C1 are therefore not related to any water components. In contrast, the temperatures of MIR1-W1 and MIR2-W2 are ∼180 K and are close to that of the H_2O "W" component (T_{ex}∼200 K; Table 2), which is at -46 km s^{-1}, and we thus conclude that MIR1-W1/MIR2-W2 corresponds to the H_2O "W" component. We emphasize that, because the CO components MIR1-W1 and MIR2-W2 were found to be in front of both binary stars, for the "W" component in H_2O, we do not consider the dilution of the relative intensity (see discussion in Section 2) when performing the rotation diagram analysis in Section 3.

We note that for the "H1" H_2O component, which is centered at -39.5 km s^{-1} and is close to v_{sys}, the existence of $\nu_2 = 2$–1 transitions and its derived high temperature exclude a connection between it and the cold CO component ("MIR1-C/MIR2-C"). It is possible that in the low-energy CO transitions, the CO counterpart of this hot H_2O component at -38 km s^{-1} may be hidden underneath a lower-temperature component at that velocity. We will discuss this possibility in Section 5.2.1.

At high-energy levels, MIR1 and MIR2 contribute differently toward the absorbing components. The component MIR2-H1 in CO is centered at -37.5 km s^{-1} and is characterized by 600–700 K. We link this to the "H1" water component. It is more difficult to determine the origin of the -54.5 km s^{-1} "H2" H_2O component. On the one hand, the velocity position, as well as the temperature, of the "H2" H_2O component, are compatible with the CO MIR2-H2 component (Table 4). On the other hand, the "H2" H_2O component is also likely correlated with the hot CO MIR1-W′ component, which is a complex amalgam of several components. MIR1-W′ has a complicated origin as is indicated by the varying average line profiles in ^{13}CO, ^{12}CO, and ^{12}CO $\nu = 2$–1. One of the two peaks in the ^{12}CO $\nu = 2$–1 profile (at -54 km s^{-1}) of MIR1-W′ coincides more

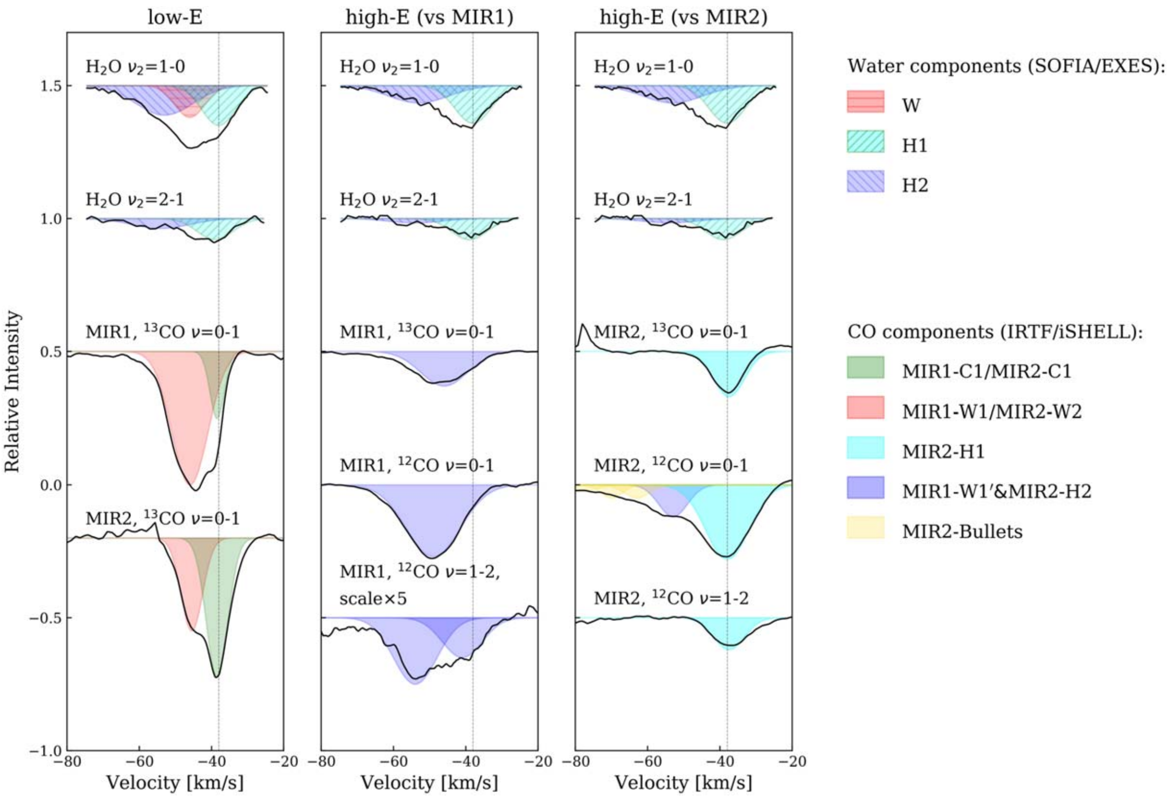

Figure 6. Comparison between averaged H_2O and CO components in low (<400 K) and high (>400 K) energy levels. The dashed vertical line represents $v_{\rm sys} = -38$ km s^{-1}, and the decomposed components are colored following Li et al. (2022). In principle, components with the same central velocities are given the same color. If components are at the same velocity and are identified with different temperatures, different colors are given. MIR1-W1′ is an exception due to the multiple potential origins (Li et al. 2022), and for lack of further information, both components in the averaged spectra of MIR1 ^{12}CO $\nu = 1$–2 are given the same color.

Table 4
Comparing Water and CO Components

Comp.	Species	$v_{\rm LSR}$ (km s^{-1})	$T_{\rm ex}$ (K)
"W"	H_2O	−46	200 ± 18
MIR1-W1	CO	−43	180^{+11}_{-14}
MIR2-W2	CO	−45.5	116 ± 7
"H1"	H_2O (Slab)	−39.4 ± 2.1	471^{+14}_{-15}
	H_2O (Disk)	−39.4 ± 2.1	491^{+13}_{-14}
MIR2-H1	CO	−37.5	662^{+23}_{-28}
"H2"	H_2O (Slab)	−54.1 ± 3.0	600^{+28}_{-27}
	H_2O (Disk)	−54.1 ± 3.0	612^{+27}_{-30}
MIR2-H2	CO	−52	482^{+97}_{-70}
MIR1-W1′	CO	−40, ∼ − 54	709^{+136}_{-101}

Note. Physical conditions of CO components are adopted from Table 7 in Li et al. (2022). The adopted temperatures of hot CO components (MIR2-H1, MIR2-H2, MIR1-W1′) are corrected values assuming a disk model.

or less with the −54.5 km s^{-1} H_2O "H2" component, although the other one (at −39.5 km s^{-1}) has no counterpart in the H_2O spectrum. Likewise, the ^{12}CO and ^{13}CO MIR1-W′ components are centered at −46 and −49 km s^{-1}, respectively. Hence, we consider that the H_2O "H2" component is related to one of the CO MIR1-W′ components.

In conclusion, the water component "H1" is much stronger, and it better matches MIR2-H1 in CO. The water component "H2" is weaker, and its origin is less clear. Thus, we connect "W" to the warm component at −45 km s^{-1} in CO, "H1" to MIR2-H1, and "H2" to either MIR2-H2 or MIR1-W′ . Once the hot components in H_2O are linked to those in CO, we can derive the H_2O/CO abundance ratio (Table 5). Assuming that the CO abundance is equal to the gas-phase C abundance in the diffuse interstellar medium (ISM; 1.6×10^{-4}; Cardelli et al. 1996; Sofia et al. 1997), we derive H_2O column densities under the disk model of 3.6×10^{19} and 8.9×10^{18} cm^{-2} for "H1" and "H2," respectively (Table 5).

5. Discussion

Under the framework of the known structures in W3 IRS 5, the *M*-band spectroscopic study on CO pictures the kinematic and physical properties of the gaseous environment. Specifically, it includes a shared foreground envelope at −38 km s^{-1}, several high-velocity clumps (referred to as "bullets") from −60 to −100 km s^{-1}, and a few warm and/or hot components in the immediate environment of the binary from −38 to −60 km s^{-1} (Li et al. 2022). While we have connected "W," "H1," and "H2" in water to MIR1-W1/MIR2-W1, MIR2-H1, and MIR2-H2 (or MIR1-W′) in CO (Section 4.2), gaseous water is not detected in the shared cold envelope or the bullets. We refer to past water studies for a more complete view toward W3 IRS 5 (see Table 5) in this section and discuss the implications of these "detections" and "nondetections" from the perspective of both the kinematics and the chemical abundances (Table 6).

Table 5
Comparison of H_2O Characteristics Derived from ISO-SWS and SOFIA-EXES Observations

Properties	ISO-SWS[a]	SOFIA-EXES			
		H1 (Slab)	H1 (Disk)	H2 (Slab)	H2 (Disk)
$T_{\rm ex}(H_2O)$ (K)	400^{+200}_{-150}	471^{+14}_{-15}	491^{+13}_{-14}	600^{+28}_{-27}	612^{+27}_{-30}
$N(H_2O)$ ($\rm cm^{-2}$)	$3^{+1}_{-1} \times 10^{17}$	$2.5^{+0.3}_{-0.2} \times 10^{19}$	$3.6 \pm 1.2 \times 10^{19}$	$5.3^{+0.3}_{-0.6} \times 10^{18}$	$8.9 \pm 0.3 \times 10^{18}$
$X[H_2O]/X[CO]$	0.05	$1.1^{+0.4}_{-0.4}$	1.5 ± 0.5	$3.8^{+1.8}_{-2.0}$ *or* $0.9^{+0.2}_{-0.4}$	0.9 ± 0.3

Note.
[a] Boonman & van Dishoeck (2003).

Table 6
Identified CO Components from the Perspective of H_2O

CO	H_2O	Origins	Implications	References
MIR2-H1	‘H1’	Blobs on the disks	The inclination of disks are in question	5.1.1
MIR1-W1′ /MIR2-H2	‘H2’	Blobs on the disks	The inclination of disks are in question	5.1.1
MIR1-W1/MIR2-W2	“W”	Shared warm foreground component	Low H_2O/CO relative abundance	5.2.1
MIR1-C1/MIR2-C2	Not detected	Shared cold foreground envelope	Low H_2O/CO relative abundance	5.2.1
MIR2-B1 to B4	Not detected	Shocked bullets	Maybe not linked to water masers	5.2.2

5.1. Hot Gaseous Water in W3 IRS 5

5.1.1. Physical Origins of the Hot Components

As we have built the connections of H_2O “H1” and “H2” components to the hot CO components via the kinematic information, it is natural to consider that, as for the corresponding CO components, the two H_2O components have a disk rather than a foreground cloud origin. Although the observed W_λ/λ can be successfully fitted to the theoretical curve-of-growth of either model (see Sections 3 and 4.1), and the two models derive comparable column densities (see Section 4.2) and temperatures, we nevertheless consider the disk model as the more preferred one for the following reasons.

If the hot components have a foreground origin, the heating mechanisms are either due to the radiative heating or due to shocks. On the one hand, if the water components are radiatively heated, the temperature range from 450–600 K corresponds to a distance of 280–140 au in the W3 IRS 5 system (Li et al. 2022). As “H1” is at the systemic velocity, this would imply that this component is static in radial velocity in the highly dynamic environment close to a high-mass protostar. The “H2” component has the opposite issue, as it is moving at a radial velocity of -15 km s^{-1} relative to the system, and would move outward by some 100 au in 30 yr. As the physical conditions derived from CO observations in 2020 are very similar to those derived in 1991 (Mitchell et al. 1991), this distance range does not work for H2, either, because of its relative velocity of 15 km s^{-1}, and it shall move outward along the line of sight for a large distance ($\sim$100 au). On the other hand, interpreting the warm temperature of these two components as the results of shocks has issues too. For J-shocks, the derived temperatures are quite high. J-shocks initially heat the gas to very high temperatures larger than 10^4 K. The gas then cools rapidly and, as molecules form, the H_2 formation energy keeps the temperature at $\sim$400 K for a column density of $\sim 10^{22}$ cm^{-2} (Hollenbach et al. 2013). Using the relationship between postshock temperature in this plateau region derived from J shock models (Equation (24) in Hollenbach et al. 2013), a temperature of 500 K (see, Table 5) requires a preshock density of, $n_0 \simeq 10^8 (T/500\ {\rm K})^{8.3} (v_s/50\ {\rm km/s}) (\Delta v_D/1\ {\rm km/s})^{1.8}$ cm^{-3}, where v_s is the shock velocity and Δv_D is the Doppler width in the molecular gas. C-type shocks can yield temperatures of 450–600 K for shock velocity of $\sim$10 km s^{-1} (Kaufman & Neufeld 1996). However, a C-shock produces a warm H_2 column density of $\sim 10^{21}$ cm^{-2}, which is far too small to be consistent with the column density we derived for the hot components.

If “H1” and “H2” are in the disks, the H_2O (and CO) excitation temperatures are similar to (but slightly lower than) the dust continuum temperature. Hence, heating is not an issue. However, the problem now resides in the exact positions of the two components on the disk based on their projected velocity information along the line of sight. As pointed out in Li et al. (2022), it is difficult to pinpoint the locations of the blobs on the disk because the inclination angles of both MIR1 and MIR2 and the systematic velocity of MIR1 are unknown. “H1” was connected with “MIR2-H1” because of the similar velocity and temperature. We note that although the central velocities of “H1” and “MIR2-H1” differ by $\sim$2 km s^{-1}, such a difference is insignificant compared with the uncertainty level of $v_{\rm LSR}$ of “H1,” which is 2.1 km s^{-1} (see Section 3). For “H2,” it is not even clear whether it is associated with MIR1 or MIR2, as the binary protostars are not spatially resolved by SOFIA, and both binary stars show hot components at the same velocity close to -55 km s^{-1}. As shown in Figure 6, in MIR1, the hot component shows up in ^{12}CO $\nu = $ 2–1 vibrationally excited transitions, which indicate a high-density region, $\sim 10^{10}$ cm^{-3}. In MIR2, the component is possibly a blob on an inclined disk at a distance smaller than 80 au to the central protostar, but such a scenario poses questions on the inclination of the disk MIR2 again. Therefore, we emphasize that disks in MIR1 and MIR2 need to be spatially and spectrally resolved to fully understand the structures in this region. Observations of vibrationally excited lines via submillimeter interferometers may be very instrumental in settling these issues.

Analyses of AFGL 2136 and AFGL 2591 observations have faced the same issues in determining whether the hot 600 K absorbing components reside in the foreground slab or the disk (Barr et al. 2022a). A foreground slab model places very strong constraints on the geometry. In AFGL 2136, if the slab has a water maser origin, the spatial coverage is even larger than the MIR disk, inconsistent with the required covering factor in order to explain the saturation of absorption lines at nonzero flux. In AFGL 2591, wavelength-dependent covering factors are needed to interpret the difference of the spatial coverage derived from the 7 and 13 μm spectroscopy, while the component does not cover the source at all at 3 μm (Barr et al. 2022b). Continuum emission size and chemistry need to be radius dependent, possibly due to the temperature gradient, to interpret the different covering factors. Moreover, similar to W3 IRS 5, too high a density, and too high an abundance argue against a shock origin. In contrast, Keplerian disks as well as clumpy substructures were spatially resolved by Atacama Large Millimeter/submillimeter Array (AFGL 2136; Maud et al. 2019) and NOEMA (AFGL 2591; Suri et al. 2021), supporting the scenario that the absorption arises in blobs in the disk.

In summary, from a broad view, it is a prevalent scenario that hot absorption gas is detected against the MIR continuum backgrounds in massive protostars (e.g., van Dishoeck & Helmich 1996; Cernicharo et al. 1997; Lahuis & van Dishoeck 2000; Boonman & van Dishoeck 2003). Locating a blob on a disk that has a vertical outward-decreasing temperature gradient requires fewer constraints on the geometry than a foreground slab model does. However, disk models face challenges in realizing such an internal heating mechanism. As discussed in Barr et al. (2022a), the flashlight effect may ensure the disk is not externally heated (Nakano 1989; Yorke & Bodenheimer 1999; Kuiper et al. 2010). However, if one proposes the dissipation of gravitational energy, the accretion rate would be orders of magnitude higher than the expected accretion rate (McKee & Tan 2003; Hosokawa et al. 2010; Kuiper et al. 2011; Caratti o Garatti et al 2017). Hence, dissipation of turbulent and/or magnetic energy inherited from the prestellar core would be required, implying a very early and active stage in the formation of these massive protostars.

5.1.2. Vibrationally Excited H_2O

We presented in Figure 3 the rotational temperatures of "H1" and "H2" in the first excited vibrational state ($\nu_2 = 1$), which are 703 ± 60 K and 946 ± 170 K, respectively. Applying curve-of-growth analyses to "H1," the corrected rotational excitation temperatures are 654^{+135}_{-191} K in the slab model and 691^{+122}_{-212} K in the disk model (Table 2) and are not far away from the result derived from the rotation diagram. The increment of the total column density of "H1" after correction is ~3–4 times, much less than that of ~20 times on the $\nu_2 = 0$ state, indicating a less severe optical depth effect.

One can derive the vibrational excitation temperature $T_{\rm vib}$ via the Boltzmann equation by comparing the column density in the $\nu_2 = 0$ level, N_0, with N_1 in the $\nu_2 = 1$ level:

$$N_1/N_0 = \exp(-2294.7\ {\rm K}/T_{\rm vib}). \tag{16}$$

We list in Table 7 multiple vibrational excitation temperatures for "H1" and "H2," using N_0 and N_1 before and after corrections on the optical depth effects. Results in Table 7 indicate that such a correction also decreases the derived vibrational excitation temperatures by a few hundred kelvin. Comparing the corrected $T_{\rm vib}$ with the corrected rotational excitation temperature for the population in the $\nu_2 = 0$ state (Table 2) or in the $\nu_2 = 1$ state, we conclude that those temperatures are in relatively good agreement within the error and that vibrational equilibrium is reached.

Table 7
Vibrational Excitation Temperatures

	H1	H2
$T_{\rm vib}$(thin) (K)[a]	843^{+553}_{-233}	1127^{+2083}_{-498}
$T_{\rm vib}$(slab) (K)[b]	511^{+30}_{-42}	549^{+86}_{-130}
$T_{\rm vib}$(disk) (K)[c]	581^{+52}_{-139}	488^{+66}_{-100}

Notes.

[a] Values of N_1 and N_0 in Equation (16) are derived from rotation diagram analysis (see Table 2; same for the columns below).

[b] N_1 and N_0 are corrected under the slab model. Since no curve-of-growth analysis is applied for the $\nu_2 = 1$ state of "H2," we adopt N_1 from the rotation diagram analysis, which is the same for the "H2" result under the disk model.

[c] N_1 and N_0 are corrected under the disk model.

The existence of vibrationally excited H_2O implies that the physical conditions of the hot absorbing gas are extreme, as the $\nu_2 = 1$ state lies 2295 K above the ground vibrational state. The two main excitation mechanisms are collisional excitation due to warm, dense gas and radiative excitation by infrared radiation due to warm dust. If the $\nu_2 = 1$ state is collisionally populated, a (postshock) density exceeding 10^{10} cm^{-3} is required for thermalization. This order takes account of a critical density[15] of 10^{11} cm^{-3} and a radiative trapping effect with β of ~0.1 for an optically thick line ($\tau \sim 10$). As a comparison, Barr et al. (2020) estimated a blob density of 10^9 cm^{-3} in the disk systems of AFGL 2136 and AFGL 2591.

Other than the collisional excitation, one can estimate the relative importance of the excitation due to the strong radiation field. As is described in Tielens (2005), with a dilution factor W ($W < 1$) on the radiation,

$$\frac{T_{\rm ex}}{T_R} = 1 + \frac{kT_{\rm ex}}{h\nu} \ln W, \tag{17}$$

in which T_R is the radiation temperature and can be characterized by a dust temperature T_d inside a blackbody. Taking that the hot components are on the surface of the disk and are receiving radiation with $W = 0.5$ (half of the disk), that $T_{\rm ex}$ is from 400–500 K (Equation (16)), and that $h\nu$ are larger than 2295 K, we derive $T_{\rm ex}/T_R > 0.85$. This result indicates that the radiation field does drive the gas to the radiative temperature. We note that at the high implied densities (~10^{10} cm^{-3}), collisions between gas and dust will lead to gas kinetic temperatures that are coupled to but slightly lower than the dust temperature (Takahashi et al. 1983).

Li et al. (2022) detected vibrationally excited CO transitions and derived a rotational excitation temperature, 791 K, of CO $\nu = 1$ state for the MIR2-H1 component. The similarity excitation temperatures of the vibrational band of water (703 K) and CO support that the excitation temperature is more representative of the color temperature of the radiation field than the kinetic temperature because water has a much larger dipole moment than CO and therefore much more rapid spontaneous radiation. Finally, we emphasize that the scenario

---

[15] Take the transition $\nu_2 = 1$, $J_{K_a,K_c} = 1_{0,1}$ as an example: the critical densities from 200–1000 K are ~6×10^{10} to 10^{11} cm^{-3}. Values of the Einstein A and the collisional rate of relevant energy states are adopted from Tennyson et al. (2001) and Faure & Josselin (2008).

that the kinetic temperature is less than the dust temperature is inherent to our results, as otherwise, one would observe emission rather than absorption lines against the MIR continuum of the observed sources (see Appendix A in Barr et al. 2022a).

5.1.3. Comparison with Past Observations

The temperature range of "H1" and "H2" at −39.5 and −54.5 $\mathrm{km\,s^{-1}}$ from 400–500 K is comparable with that derived from the ISO-SWS observations in Boonman & van Dishoeck (2003).[16] In the ISO-SWS study, the individual velocity components were not spectrally resolved, separate transitions were blended ($R = 1400$, 214 $\mathrm{km\,s^{-1}}$), and a Doppler width b of 5 $\mathrm{km\,s^{-1}}$ was assumed in modeling the absorption features. As presented in Table 5, the column density of hot gaseous components derived from our SOFIA/EXES study is about 2 orders of magnitude larger than the ISO-SWS results. This is a significant increment and much more that the 2.4 and 4.3 times increments derived for AFGL 2136 and AFGL 2591 (Barr et al. 2022a). We interpret this from two aspects: first, the absorption intensities of W3 IRS 5 measured by ISO-SWS are much lower than those for AFGL 2136 and AFGL 2591 (Boonman & van Dishoeck 2003). This indicates a more significant opacity effect than in AFGL 2136 and AFGL 2591. As a result, the column densities in W3 IRS 5 corrected by the curve-of-growth analysis are much higher than those corrected values in AFGL 2136 and AFGL 2591 (Barr et al. 2022a). Second, saturated lines do not go to 0 but rather reach a nonzero intensity because of either the temperature gradient in a disk atmosphere or a covering factor less than 1 for a foreground cloud.

5.2. Other Foreground Gaseous Components

5.2.1. The Radiatively Heated Foreground Clouds

Comparison between the average low-energy CO and H_2O lines (Figure 6) reveals a warm component "W" at −45.5 $\mathrm{km\,s^{-1}}$, which has a H_2O-to-CO relative abundance of 4.4%. While "W" is considered a shared component in front of MIR1 and MIR2, according to Li et al. (2022), this component is radiatively heated and located at least as close as 2000 au to the protostars. In contrast, the cold CO component at −38 $\mathrm{km\,s^{-1}}$, which is regarded as a shared foreground envelope of ~50 K, is not present in H_2O. If the water in the cold envelope has a comparable column density to that of CO, saturated absorption lines will be detected (see Appendix C). We conclude that the nondetection of water is due to a too-low column density ($<4.7 \times 10^{15}$ $\mathrm{cm^{-2}}$). Therefore, both the warm and the cold components have a low H_2O/CO relative abundance.

However, past observations of water lines reveal the rather cool (~50 K) component but did not observe the warm component (~200 K). Observations in the pure rotational ortho-lines of water by SWAS (Snell et al. 2000) and Odin (Wilson et al. 2003) derive comparable results. Adopting a temperature of 40 K, both studies reveal a relative ortho-H_2O abundance of the order of 1–2 × 10^{-9}, or column densities of $\sim 10^{13}$ $\mathrm{cm^{-2}}$. These results are also comparable with the column density of 10^{13} $\mathrm{cm^{-2}}$ derived by Herschel-HIFI observations (Chavarría et al. 2010), albeit that the latter result is rather model dependent. Therefore, we are reporting an EXES upper limit that is much higher than the column density observed by SWAS, Odin, and Herschel. We suggest that both the SWAS and Odin beams are very large and they may be measuring the large-scale core, which has a low average column density. If there is a density gradient rising toward the central source, then the submillimeter observations would measure column density that could be much less than along a pencil beam. With a pencil beam, it is difficult to come up with a clear picture of the structural relationship of these three components and with the larger scale structure of the source.

5.2.2. The Foreground Bullets

The four high-velocity "bullets" from −100 to −60 $\mathrm{km\,s^{-1}}$ in CO (200–300 K) were not detected in the water observations. Those bullets have been attributed to shocked gas intercepted by the pencil beam (Li et al. 2022). Specifically, Li et al. (2022) quantified the column density, the density, the velocity, and the thickness of these bullets and concluded that they are possibly correlated with the maser clumps moving toward us. As a comparison, assuming that water has a comparable column density to CO, one would expect to see water absorption lines with a depth of ~80% relative to the continuum. However, among all of the identified water lines, the only transition that has a potential absorption feature with an intensity depth of 5% at ~ -80 $\mathrm{km\,s^{-1}}$ is $2_{2,1} - 3_{1,2}$, which has an expected line depth of ~30%. Therefore, CO bullets are indeed not detected in water lines.

J and C shocks are expected to lead to high abundances of H_2O, comparable to CO (Hollenbach et al. 2009, 2013). Hence, the absence of water absorption lines associated with this high-velocity gas sheds some doubt on their interpretation as shocked bullets and a potential link to water masers. We emphasize that we do recognize other factors that are related to nondetections of the bullets, although those factors are insignificant. For example, we may define the baseline beyond ~ -75 $\mathrm{km\,s^{-1}}$ poorly where the bullets are expected. In addition, those foreground bullets were exclusively found in front of MIR2 in the CO observations and may suffer from extra dilution in the SOFIA observations. However, these factors are insignificant for the high abundances of H_2O-to-CO, as one would expect to observe prominent saturated H_2O absorption features.

5.3. Chemical Abundances along the Line of Sight

The availability of data on column densities of different species such as gaseous CO and ices along the line of sight toward W3 IRS 5 makes it an appropriate example to address the oxygen and carbon budget. We discuss below the reservoirs of the two elements in different environments of the W3 IRS 5 system and other massive protostars including the hot disks as well as the cold foreground clouds.

As described in Section 5.1, SOFIA observations derived much higher column densities of hot gaseous water than that of hot gaseous CO in W3 IRS 5 as well as AFGL 2136 and AFGL 2591 (Barr et al. 2022a). While iSHELL measurements (Barr et al. 2020; Li et al. 2022) provide a better constraint on the amount of gaseous CO from the same region, we derive

---

[16] According to Salgado et al. (2012), in the mid-IR, W3 IRS 5 is isolated, even in the large ~20″ISO/SWS beam. To our knowledge, there is only one other source, which is found and labeled as "MIR3" by van der Tak et al. (2005). The brightness of MIR3 is ~1% of either MIR1 or MIR2, so we ignore its influence on our comparison between the ISO and SOFIA observations.

Table 8
Repository of Elemental Carbon and Oxygen in the Cold Regions of Massive Protostars

	W3 IRS 5			AFGL 2136			AFGL 2591		
	N (cm^{-2})	X_C (ppm)	X_O (ppm)	N (cm^{-2})	X_C (ppm)	X_O (ppm)	N (cm^{-2})	X_C (ppm)	X_O (ppm)
Hydrogen	2.0(23)			7.4(22)			8.0(22)		
CO (gas)[a]	4.7(18)	23.5	23.5	5.1(18)	68.9	68.9	2.5(18)	31.3	31.3
H_2O (gas)[b]	<4.7(15)	…	<0.02	…	…	…	…	…	…
CO (ice)[c]	2.1(17)	1.1	1.1	2.7(17)	3.6	3.6	…	…	…
CO_2 (ice)[c]	7.1(17)	3.6	7.1	7.8(17)	10.5	21.1	1.6(17)	2.0	4.0
H_2O (ice)[c]	5.1(18)	…	25.5	5.1(18)	…	68.9	1.2(18)	…	15.0
CH_3OH (ice)[c]	1.7(17)	0.9	0.9	2.6(17)	3.5	3.5	1.7(17)	2.1	2.1
Sum (ice)	…	5.6	34.6	…	17.6	97.1	…	4.1	21.1
Sum (total)	…	29.1	58.1	…	86.5	166.0	…	35.4	52.4
Diffuse Clouds (gas)		160[d]	284[e]		160	284		160	284
Silicate Abundance[f]			200			200			200
Solar Abundance[g]		269	490		269	490		269	490
B-stars Abundance[h]		214	575		214	575		214	575

Notes. (1) For column densities, powers of 10 are given in parentheses. (2) X_C and X_O are the relative abundances derived from N_C/N_H and N_O/N_H.

[a] Results of gaseous CO are adopted from Li et al. (2022) for W3 IRS 5, and are from Barr et al. (2020) for AFGL 2136 and AFGL 2591. The temperatures of the cold regions are ~50 K, 27 K, and 49 K for W3 IRS 5, AFGL 2136, AFGL 2591, separately (Barr et al. 2020; Li et al. 2022).

[b] Results from this work.

[c] All measurements on ice are adopted from Gibb et al. (2004).

[d] Cardelli et al. (1996), Sofia et al. (1997).

[e] Cartledge et al. (2004).

[f] Tielens & Allamandola (1987).

[g] $\log\epsilon_C = 8.43$, $\log\epsilon_O = 8.69$ (Asplund et al. 2009).

[h] Nieva & Przybilla (2012).

high relative abundances of H_2O to CO; i.e., ~1–1.5 for W3 IRS 5, 1.6 for AFGL 2136, and 7.4 for AFGL 2591. Such a high relative H_2O to CO abundance is expected for warm, dense gas where gas-phase chemistry rapidly converts the available O not in CO into H_2O (Kaufman & Neufeld 1996). As a comparison, these values are much higher than the $H_2O/CO = 10^{-4}$ derived from submillimeter observations by Herschel-HIFI toward the hot core region of AFGL 2591 (Kaźmierczak-Barthel et al. 2014), or the value of 4.4% from the warm 200 K component identified in this water study (see Table 2). On the other hand, a high relative H_2O to CO abundance from 1–2 was observed toward T Tauri and Herbig disks (Carr & Najita 2008; Salyk et al. 2011).

In the cold dense ISM, there is a well-documented problem of the missing oxygen budget (Whittet 2010). While Hollenbach et al. (2009) predicted that oxygen not in silicates or oxides should be eventually converted into gaseous CO and ices, a substantial shortfall of oxygen is observed. In the study of the Taurus complex dark clouds (Whittet 2010), the combined contributions of gaseous CO, ice, and silicate/oxide account for < 300 ppm of the elemental oxygen compared to the solar value of 490 ppm (Asplund et al. 2009). We observed a similar missing oxygen reservoir in W3 IRS 5: assuming 284 ppm of the O in diffuse clouds (Cartledge et al. 2004), we only see a value of 58.1 ppm (20.4%) in cold, dense clouds (see Table 8). If one uses local B stars as the interstellar standard, the total budget of the elemental abundance of oxygen is even higher (575 ppm rather than 490 ppm; Nieva & Przybilla 2012). Therefore, a budget close to the oxygen abundance in silicate (~200 ppm; Tielens & Allamandola 1987) is missing or is locked up in an unidentified form, which is referred to as "the unidentified depleted oxygen (UDO)" in Whittet (2010).

The intrinsic properties of the reservoir of the missing oxygen remain mysterious. Refractory dust compounds like carbonates are implausible, as they will also survive and appear in the diffuse medium. Neither gas-phase nor solid-phase O_2 are possible as well. While SWAS observations (Goldsmith et al. 2000) toward massive protostars provide an upper limit of 0.1 ppm on the gaseous O_2, solid O_2 is too volatile in the line of sight of W3 IRS 5. Oxygen-bearing organics in solid ice would be a potential carrier, although no significant detection of the related bonds has yet been detected at infrared wavelengths (Gibb et al. 2004). We suggest that the MIRI spectrograph on board the JWST is well suited to study such an organic inventory. One other possibility of the UDO is a population of very large water ice grains (>1 μm) in the cold gas (Jenkins 2009). These large grains produce gray extinction, and their putative presence is hard to refute.

Similar to the "oxygen crisis," a depletion problem in elemental carbon exists in the envelope of W3 IRS 5 (see Table 8). The total amount of carbon (32 ppm) comprises only 19.7% of the value expected in diffuse clouds (160 ppm; Cardelli et al. 1996; Sofia et al. 1997). As discussed in Li et al. (2022), one speculation is that the carbon-containing ice compounds were converted into an organic residue by prolonged UV photolysis (Bernstein et al. 1995, 1997; Vinogradoff et al. 2013).

Both the "oxygen crisis" and the "carbon crisis" were observed in AFGL 2136 and AFGL 2591 as well. In contrast to previous studies that relied on comparing pencil beam IR absorption line studies with submillimeter emission observations, the IR pencil beam samples the same material in absorption for these massive protostars. As shown in Table 8, the depletion problems are more severe for AFGL 2591, but less severe for AFGL 2136. We suggest that further studies of the different oxygen reservoirs could help pinpoint the processes involved in the missing oxygen or carbon reservoirs by studying a large enough sample with diverse characteristics.

6. Summary

We conducted high spectral resolution ($R = 50{,}000$; $6\ \mathrm{km\,s^{-1}}$) spectroscopy from 5–8 μm with EXES on board SOFIA toward the hot core region associated with the massive binary protostar W3 IRS 5. By comparing with the LTE models constructed with the existing laboratory line information, we identified about 180 $\nu_2 = 1 - 0$ and 90 $\nu_2 = 2 - 1$ absorption lines. Preliminary Gaussian fittings and rotation diagram analyses reveal two hot components with $T > 600$ K and one warm component of 190 K. However, the large scatter in the rotation diagrams of the two hot components reveals (1) opacity effects, (2) that the absorption lines are not optically thin, and (3) the total column densities derived from the rotation diagrams are underestimated.

We adopted two curve-of-growth analyses to account for the opacity effects of the hot components. One model considers absorption in a foreground slab partially covering the background emission. The other model assumes absorption in the photosphere of a circumstellar disk with an outward-decreasing temperature in the vertical direction. In both models, about half of the data points converted from the $\nu_2 = 1 - 0$ transitions are located on the logarithmic part of the curve-of-growth, confirming that the corresponding absorption lines are optically thick. The two curve-of-growth analyses correct the column densities by at least an order of magnitude and lower the derived excitation temperatures accordingly. We note that for the disk model, the results of the curve-of-growth analysis depend on the adopted velocity width σ_v and the parameter ϵ that characterizes absorption and scattering of the absorption line. We provide a reference table for different σ_v and ϵ, as the two parameters are poorly constrained.

Although our SOFIA-EXES observations do not spatially resolve the binary protostars in W3 IRS 5, using the kinematic and temperature characteristics, we link each H_2O component to a spatially separate CO component identified in IRTF/iSHELL observations ($R = 88{,}100$). Specifically, the warm H_2O component "W" is linked to the shared warm CO component MIR1-W1/MIR1-W2, the hot H_2O component "H1" is linked to the MIR2-H2 in CO, and the hot H_2O component "H2" is considered to be related to one of the CO MIR1-W′ components.

Once the connections of H_2O components and CO components were established, we discussed the physical origins of H_2O components in light of a better understanding of CO components. From our analysis, we conclude that the disk model is the preferred one over the slab model, due to consideration of the geometry constraints, although disk models face challenges in realizing such an internal heating mechanism.

We derive the H_2O/CO abundance ratio based on the results of the disk model and discuss the chemical abundances along the line of sight based on the H_2O-to-CO connection. For the hot gas, we derive a high H_2O/CO abundance ratio of 0.9. Such a high relative H_2O to CO abundance is expected for warm, dense gas where gas-phase chemistry rapidly converts the available O not in CO into H_2O. For the cold gas, we observe a substantial shortfall of oxygen in agreement with earlier studies of cold dense clouds. We suggest that organics in solid ice are the potential carrier.

Acknowledgments

We thank the anonymous referee for providing thorough comments and helpful suggestions that greatly improved the quality of this paper. We acknowledge the support for the EXES Survey of the Molecular Inventory of Hot Cores (SOFIA No. 08-0136) at the University of Maryland from NASA (NNA17BF53C) Cycle Eight GO Proposal for the Stratospheric Observatory for Infrared Astronomy (SOFIA) project issued by USRA.

Software: Astropy (Astropy Collaboration et al. 2013, 2018), Matplotlib (Hunter 2007), NumPy (Harris et al. 2020), SciPy (Virtanen et al. 2020).

Appendix A
Telluric Molecular Lines from 5.36–7.92 μm

We present in Figure 7 the important telluric lines from 5.36–7.92 μm produced by the PSG models under representative observational parameters (see Table 9). Eight molecular species, H_2O, O_3, CH_4, NO_2, N_2O, CO_2, HNO_3, and O_2, are among the most important ones. For the 15 observational settings, the input surface pressure and scaling factors are tuned by hand to visually match the telluric features in observed spectra, and therefore, may not represent the actual values.

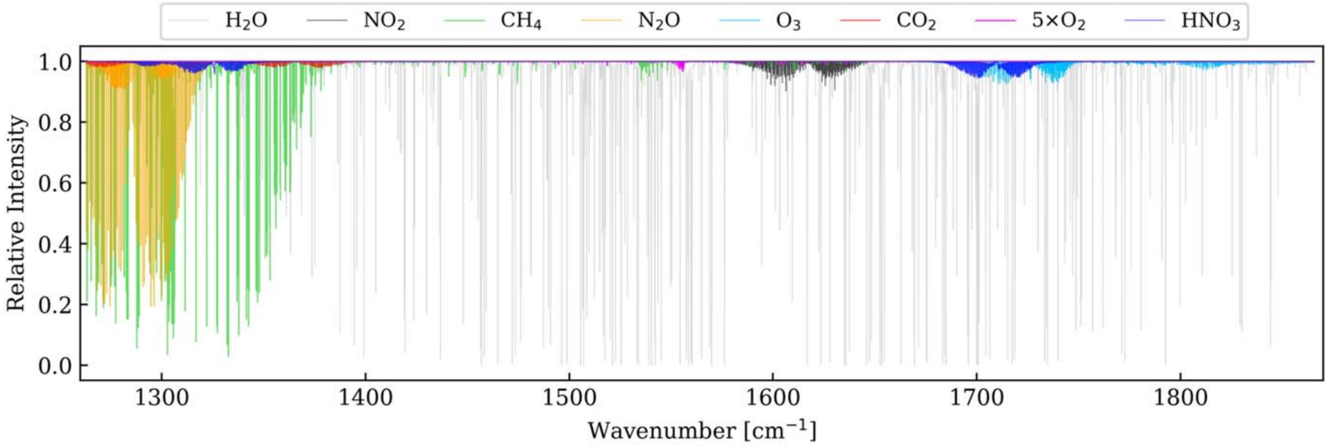

Figure 7. Important atmospheric telluric lines from 5.36–7.92 μm.

Table 9
Inputs for the PSG Models

Source (1)	λ (μm) (2)	P (bar) (3)	H_2O (4)	O_3 (5)	CH_4 (6)	NO_2 (7)	N_2O (8)	CO_2 (9)	HNO_3 (10)	O_2 (11)
W3 IRS 5	5.36–5.51	0.75	1	1	⋯	⋯	⋯	⋯	⋯	⋯
	5.48–5.67	0.7	1	1	⋯	⋯	⋯	⋯	⋯	⋯
	5.65–5.84	0.85	0.7	1	⋯	⋯	⋯	⋯	⋯	⋯
	5.83–6.02	0.92	0.5	1.5	⋯	⋯	⋯	⋯	2	⋯
	6.01–6.20	0.83	1	⋯	1	1	⋯	⋯	⋯	⋯
	6.01–6.20	0.75	1	⋯	1	1.5	⋯	⋯	⋯	⋯
	6.18–6.37	0.83	0.8	⋯	1	1.3	⋯	⋯	⋯	⋯
	6.19–6.37	0.85	0.6	⋯	1	0.8	⋯	⋯	⋯	⋯
	6.35–6.61	0.75	0.8	⋯	2	⋯	⋯	⋯	⋯	1
	6.35–6.61	0.83	0.9	⋯	1.5	⋯	⋯	⋯	⋯	⋯
	6.59–6.85	0.77	1	⋯	2	⋯	⋯	⋯	⋯	⋯
	6.59–6.85	0.85	1	⋯	1	⋯	⋯	⋯	⋯	⋯
	6.79–7.06	0.75	1.5	⋯	1.8	⋯	⋯	⋯	⋯	⋯
	7.19–7.45	0.8	1	⋯	1.5	⋯	⋯	1	⋯	⋯
	7.67–7.92	0.7	1	⋯	2	⋯	2.5	1	1	⋯
Sirius	7.18–7.46	0.7	1.4	⋯	1.7	⋯	⋯	1	⋯	⋯

Notes. Column (1): Sirius is the standard star for the observation session on 2022-02-24 at 7.19–7.45 μm. Column (3): the input surface pressure (Earth at 4084 m) in the PSG models. Columns (4)–(11): the input scaling factors of different atmospheric molecular species in the PSG models. See Figure 7 for an illustration of the contribution of different molecular species at different wavelengths.

Appendix B
Data Reduction: Sirius versus PSG Models

The standard star, Sirius, was observed only in one setting from 7.28–7.46 μm. While the Sirius spectrum has advantages in reflecting the actual baseline, we compare the qualities of the results derived by using the Sirius spectrum as well as using the PSG models. The data reduction with Sirius is straightforward, as the median filtering processes or the modeling of telluric lines are not needed.

As a result, we present in Figure 8 the equivalent widths of each individually identified line derived from the two data reduction methods. We conclude that the results are in good agreement with each other by ∼10%.

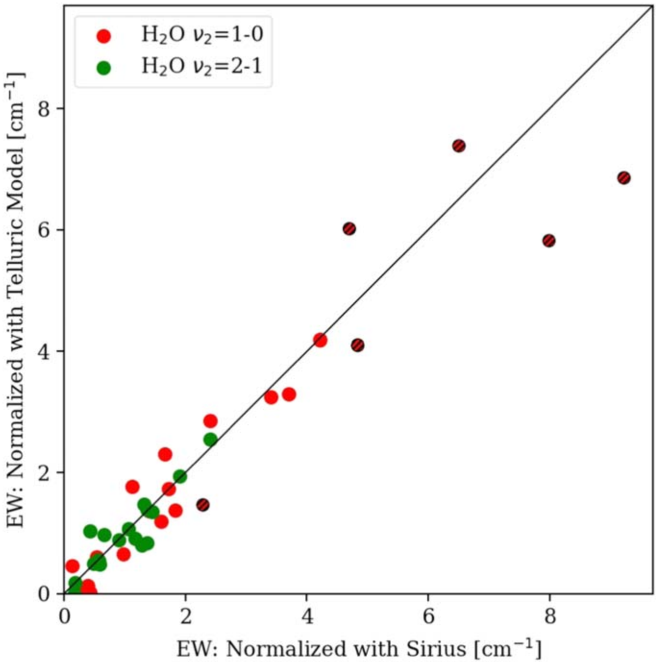

Figure 8. Comparison between the equivalent widths determined from spectra calibrated with the standard star Sirius vs. using PSG models for the telluric correction.

Appendix C
The Hidden Component at −38 km s^{-1}

As presented in Sections 3 and 4, data analyses in this paper are based on the decomposition of the absorption profiles into the three components at −54.5, − 45, and −39.5 km s^{-1} in low-energy levels, while the −39.5 km s^{-1} component is hot. However, we realize that one cold component of ∼50 K may exist at −38 km s^{-1} because of the detection of the cold CO component (Li et al. 2022).

We argue that a cold component is possibly hidden in Figure 9, in which a list of accumulative average spectra is

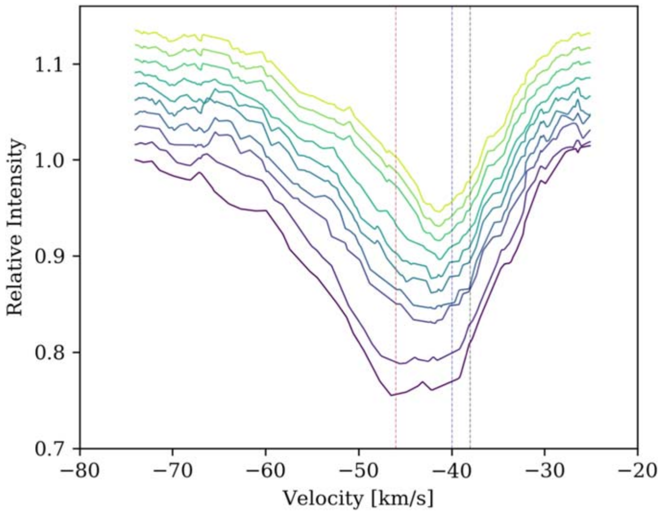

Figure 9. Accumulative average spectra from 100–1000 K. Each spectrum represents the median of spectra in energy levels between 0 and 100 K, 0 and 200 K, ⋯, 0 and 1000 K. The dashed vertical lines represent −46, −40, and −38 km s^{-1}.

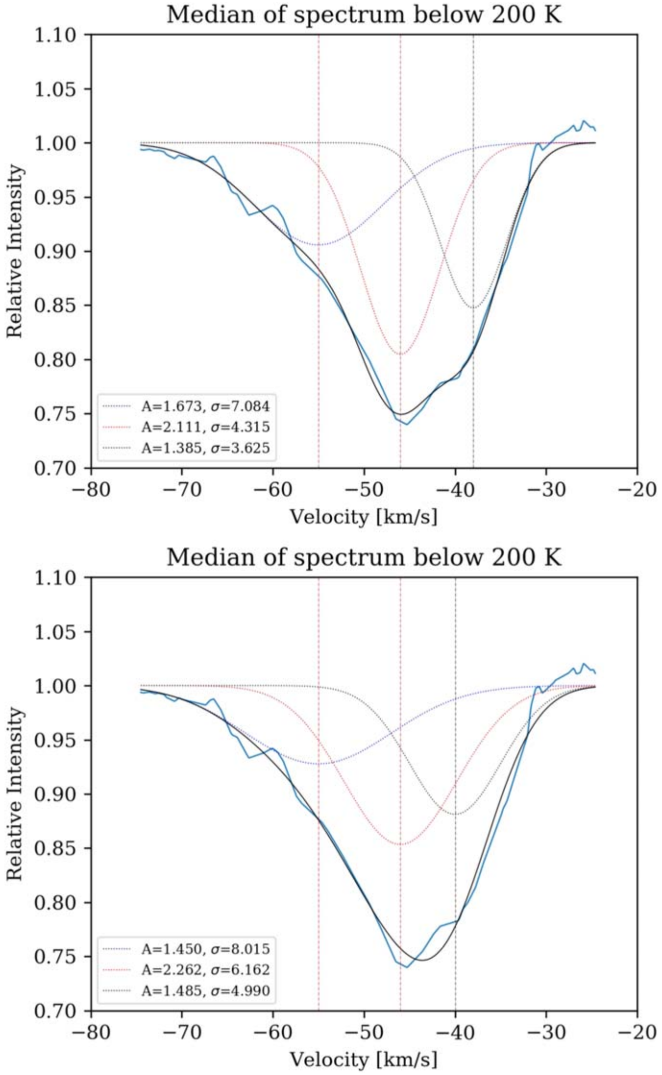

Figure 10. Two different Gaussian fitting results for the spectrum averaged below 200 K. In the upper panel, the central velocities are −55, − 46, and −38 km s^{-1}. In the lower panel, the central velocities are −55, − 46, and −40 km s^{-1}.

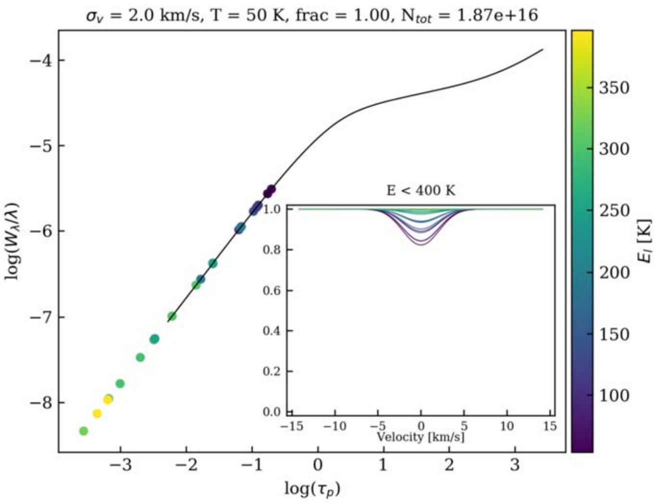

Figure 11. Expected cold line profiles of water and the correspondent curve-of-growth based on parameters constrained in CO observations.

presented. We note that the absorption feature at −35 km s^{-1} is possibly related to the cold component because it disappears as the energy levels increase. We also present two different Gaussian fitting methods for the average spectrum below 200 K in Figure 10, while in one, we fix the right wing with a component at −38 km s^{-1} and in the other at −40 km s^{-1}. We conclude that the previous one provides a better fit, suggesting that at this energy level, the cold −38 km s^{-1} component possibly dominates the line profile.

Even if the cold −38 km s^{-1} component does exist, we conclude that the water-to-CO abundance is still low at this temperature. Otherwise, very saturated water absorption lines will dominate the line profiles. We estimate an upper limit of such a water-to-CO ratio of 0.4% by Figure 11.

Appendix D
Additional Figures

Figure 12 presents the two grid-search results and the best-fitted curve-of-growth for the “H2” component. Figure 13 presents the results for the $\nu_2 = 2$–1 transitions on the “H1” component.

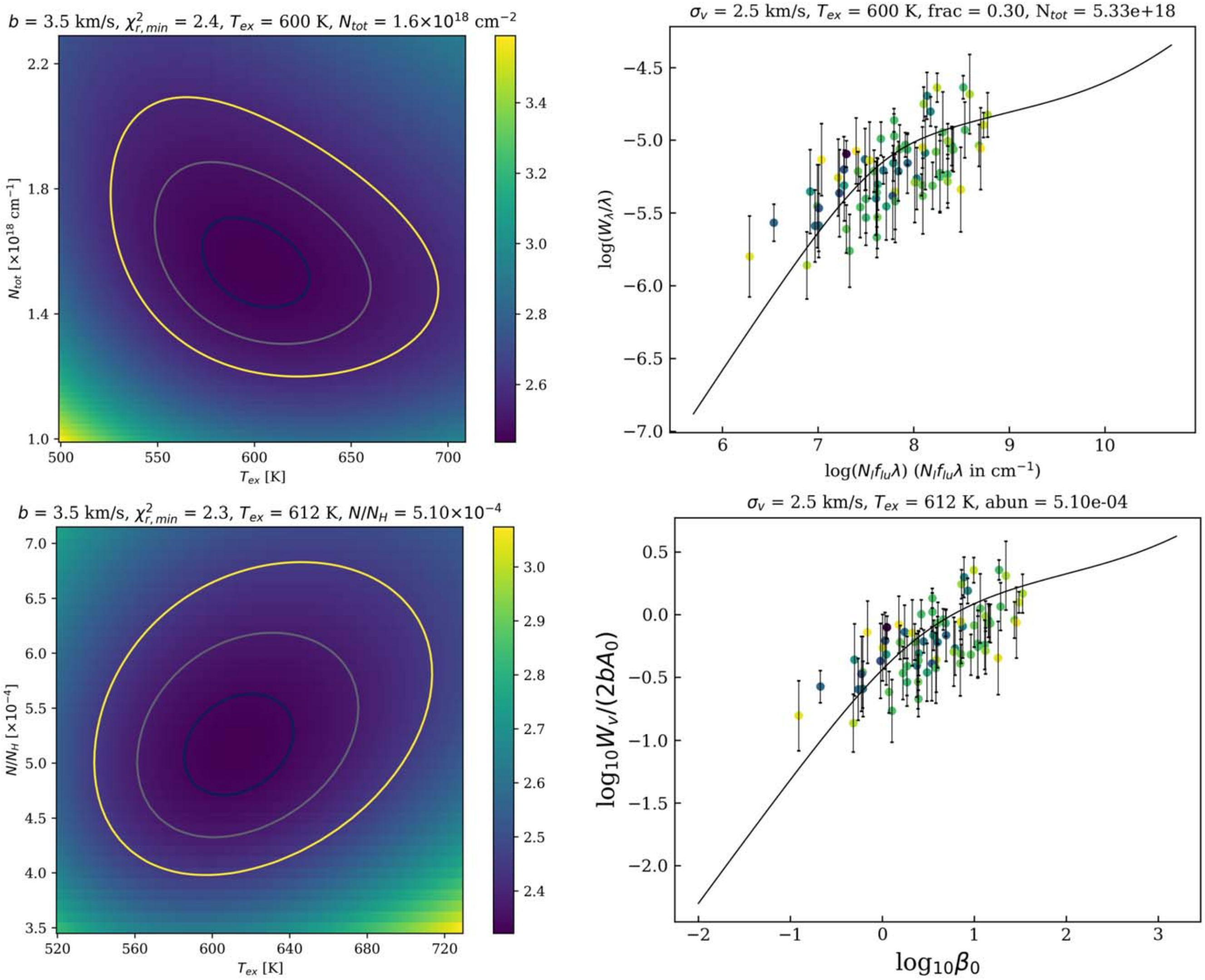

Figure 12. Left panels: grid-search results of "H2" ($\nu_2 = 2$–1 transition) for both the slab and the disk model illustrating the best-fitting results. The contours represent the 1σ, 2σ, and 3σ uncertainty levels. Right panels: the curves of growth for the slab and the disk model.

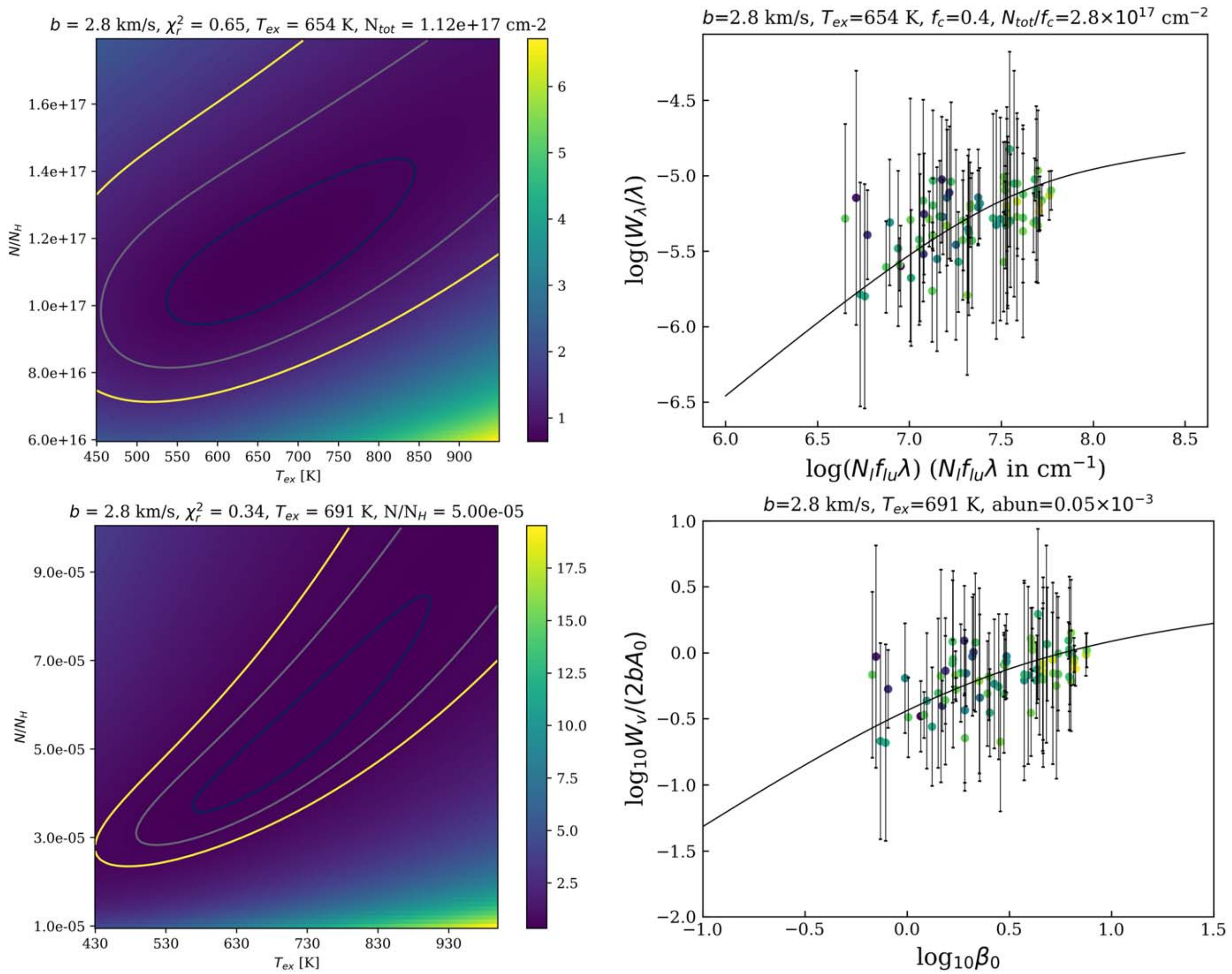

Figure 13. Left panels: grid-search results of "H1" ($\nu_2 = 2$–1 transition) for both the slab and the disk model illustrating the best-fitting results. The contours represent the 1σ, 2σ, and 3σ uncertainty levels. Right panels: the curves of growth for the slab and the disk model.

Appendix E
List of the Water Lines

We present from Table 10–14 the properties of decomposed water lines, H_2O $\nu_2 = 1$–0 and $\nu_2 = 2$–1, of W3 IRS 5 from 5.36–7.92 μm in this study. For "H2" in the $\nu_2 = 1$–0 transitions, the velocity centers of lines with $E_l < 800$ K are fixed at -54 km s^{-1}. For "W," in the $\nu_2 = 1$–0 transitions, the velocity centers are fixed at -45 km s^{-1}. $\tau_{p,\mathrm{thin}}$, $\tau_{p,\mathrm{slab}}$, and β_0 are calculated from the best-fitted temperatures and column densities from the rotation diagram, the slab model, and the disk model.

The Gaussian fitting results of the central velocity, v_{LSR}, vary among different transitions of the same physical component. The dispersion is contributed by both the uncertainty in v_{LSR} as well as the uncertainty level of the fitting results, Δv_{LSR}. We report the fitted central velocity and the uncertainty level of one component as follows:

$$v_{\mathrm{LSR}} = \frac{1}{N}\sum_i v_{\mathrm{LSR},i}, \tag{E1}$$

and

$$\Delta v_{\mathrm{LSR}} = \sqrt{\frac{1}{N}\sum_i (\Delta v_{\mathrm{LSR},i})^2 + \langle v_{\mathrm{LSR},i}^2 \rangle - \langle v_{\mathrm{LSR},i} \rangle^2}\,. \tag{E2}$$

Table 10

Line Parameters of the -39.5 km s^{-1} Component ("H1") in the $\nu_2 = 1$–0 Transition

Transition	λ (μm)	E_l (K)	g_l	g_u	A_{ul} (s^{-1})	$v_{\rm LSR}$ (km s^{-1})	σ_v (km s^{-1})	N_l ($\times 10^{15}$ cm^{-2})	W_v (km s^{-1})	log $_{10}(\tau_{p,\rm thin})$	log $_{10}(\tau_{p,\rm slab})$	log $_{10}(\beta_0)$
$12_{1,11}$-$11_{2,10}$	5.3737	2193.9	23	25	10.9	-39.2 ± 1.3	6 ± 1	5.6 ± 0.5	3.67 ± 0.802	-0.55	0.35	0.58
$11_{3,8}$-$10_{4,7}$	5.3772	2274.8	63	69	3.3	-40.7 ± 1.4	5.2 ± 1	11.4 ± 1.6	2.372 ± 0.7	-0.68	0.2	0.43
$7_{6,1}$-$7_{5,2}$	5.4183	1524.6	45	45	1.3	-40.5 ± 0.8	4.2 ± 0.8	25.5 ± 3.3	1.904 ± 0.526	-0.7	0.3	0.5
$11_{2,10}$-$10_{1,9}$	5.4248	1860	21	23	10.2	-41.4 ± 0.6	6 ± 0.5	8.1 ± 0.4	4.98 ± 0.53	-0.39	0.61	0.82
$11_{6,5}$-$11_{5,6}$	5.4521	2875.6	69	69	2.4	-39 ± 1.2	4 ± 1.2	4 ± 0.6	0.6 ± 0.18	-1.21	-0.48	-0.23
$10_{1,9}$-$9_{2,8}$	5.4862	1554.1	19	21	9.5	-41 ± 0.8	6 ± 0.8	7.3 ± 0.5	4.51 ± 0.724	-0.44	0.84	1.04
$10_{1,9}$-$9_{2,8}$	5.4862	1554.1	19	21	9.5	-38.2 ± 0.8	5.6 ± 0.9	6.1 ± 0.4	3.766 ± 0.592	-0.5	0.84	1.04
$10_{3,7}$-$9_{4,6}$	5.4904	1928.9	19	21	2.6	-42 ± 4	6 ± 2.4	10.3 ± 3.3	1.85 ± 1.244	-0.87	-0.07	0.14
$11_{4,7}$-$10_{5,6}$	5.5031	2472.4	63	69	1.7	-39.1 ± 3.2	6 ± 3.1	20.7 ± 5.5	2.416 ± 1.356	-0.75	-0.23	0
$9_{2,7}$-$8_{3,6}$	5.5179	1447.3	51	57	4.6	-39 ± 0.6	5.3 ± 0.6	13.3 ± 0.7	4.026 ± 0.488	-0.44	1.06	1.25
$5_{3,3}$-$4_{2,2}$	5.5229	454.3	9	11	3.9	-37.5 ± 1.5	5.5 ± 1.2	14.5 ± 1.7	3.908 ± 1.114	-0.42	1.19	1.35
$11_{1,10}$-$11_{0,11}$	5.529	1909.1	69	69	0.8	-39.1 ± 1.1	4 ± 0.9	17.3 ± 2.5	0.896 ± 0.268	-1.03	-0.04	0.17
$12_{4,9}$-$12_{3,10}$	5.5298	2823.1	75	75	2.2	-36 ± 3.5	6 ± 3.3	8.3 ± 2.5	1.192 ± 0.752	-1.08	-0.41	-0.16
$9_{2,8}$-$8_{1,7}$	5.5319	1270	17	19	8.7	-39.1 ± 1.4	5.4 ± 0.8	6.7 ± 0.8	3.88 ± 1.12	-0.45	1.03	1.22
$9_{1,8}$-$8_{2,7}$	5.5479	1273.9	51	57	8.7	-39.5 ± 0.6	5.5 ± 0.6	8.4 ± 0.5	4.812 ± 0.606	-0.37	1.5	1.69
$10_{5,6}$-$10_{4,7}$	5.5496	2274.8	63	63	2.7	-40.2 ± 1	4 ± 1	5.8 ± 0.7	1.046 ± 0.268	-0.95	0.12	0.35
$5_{5,0}$-$5_{4,1}$	5.5685	878	33	33	1.1	-39.6 ± 2.4	4 ± 2.2	31.1 ± 9.9	2.188 ± 1.506	-0.61	0.74	0.92
$6_{5,1}$-$6_{4,2}$	5.5707	1090.1	13	13	1.8	-40.4 ± 1.3	5.5 ± 1.2	23.8 ± 2.6	2.696 ± 0.644	-0.66	0.35	0.53
$7_{5,2}$-$7_{4,3}$	5.5775	1339.6	45	45	2.2	-40.3 ± 0.8	4.2 ± 0.8	17 ± 1.5	2.398 ± 0.454	-0.59	0.76	0.95
$8_{2,7}$-$7_{1,6}$	5.5836	1013	45	51	7.9	-40.5 ± 1.7	6 ± 1.1	12.3 ± 1.6	6.186 ± 2.026	-0.25	1.66	1.84
$9_{3,6}$-$8_{4,5}$	5.6118	1615	51	57	2	-39.7 ± 3.4	6 ± 2	20.9 ± 5.7	3.028 ± 1.798	-0.63	0.57	0.77
$7_{2,6}$-$6_{1,5}$	5.6318	781	13	15	6.9	-39.3 ± 3.3	5 ± 1.9	8.2 ± 2	3.39 ± 2.214	-0.4	1.3	1.47
$9_{2,8}$-$9_{1,9}$	5.6485	1323.7	19	19	1.1	-42.9 ± 1.1	6 ± 1	48.6 ± 4	3.646 ± 0.652	-0.55	0.12	0.32
$9_{1,9}$-$8_{0,8}$	5.6551	1070.3	17	19	13.1	-39.7 ± 0.9	5.6 ± 1	3.9 ± 0.4	3.748 ± 0.8	-0.51	1.42	1.6
$9_{1,9}$-$8_{0,8}$	5.6551	1070.3	17	19	13.1	-41.8 ± 1.2	5.1 ± 0.9	3.7 ± 0.4	3.498 ± 0.92	-0.48	1.42	1.6
$9_{4,6}$-$9_{3,7}$	5.659	1749.6	19	19	3	-38.2 ± 3	5.4 ± 2.1	9 ± 2.6	1.874 ± 1.148	-0.82	0.15	0.36
$9_{4,6}$-$9_{3,7}$	5.659	1749.6	19	19	3	-39.5 ± 2.5	5.2 ± 1.8	8.6 ± 2.1	1.784 ± 0.932	-0.81	0.15	0.36
$10_{2,8}$-$10_{1,9}$	5.6645	1860	21	21	2.1	-37.3 ± 1	5.2 ± 1.1	8.5 ± 0.9	1.24 ± 0.26	-1	-0.06	0.15
$9_{3,7}$-$9_{2,8}$	5.6784	1554.1	19	19	2.3	-40.8 ± 1.4	4.4 ± 1.5	5.9 ± 0.9	0.966 ± 0.318	-1.04	0.23	0.43
$11_{5,6}$-$11_{4,7}$	5.6789	2731.7	69	69	4	-38.9 ± 2	4 ± 1.8	2.6 ± 0.7	0.732 ± 0.424	-1.12	-0.07	0.18
$8_{4,5}$-$8_{3,6}$	5.6864	1447.3	51	51	3.1	-38.6 ± 1	6 ± 0.8	20.3 ± 1.5	4.168 ± 0.69	-0.48	0.89	1.08
$7_{1,6}$-$6_{2,5}$	5.6921	795.4	39	45	6.6	-37.5 ± 0.9	5.4 ± 0.7	11.9 ± 0.7	5.232 ± 0.832	-0.25	1.75	1.93
$7_{4,4}$-$7_{3,5}$	5.7051	1174.8	15	15	3.1	-38.4 ± 1.5	5.7 ± 1	14.4 ± 1.9	3.052 ± 0.882	-0.6	0.61	0.79
$11_{3,8}$-$11_{2,9}$	5.7131	2432	69	69	3.2	-37.5 ± 1.1	4.4 ± 0.9	5.4 ± 0.8	1.23 ± 0.356	-0.92	0.12	0.35
$6_{4,3}$-$6_{3,4}$	5.7162	933.6	39	39	2.9	-39.2 ± 0.8	6 ± 0.6	30.5 ± 2.4	5.582 ± 1.016	-0.32	1.21	1.39
$5_{2,4}$-$4_{1,3}$	5.7187	396.3	9	11	5.2	-38.2 ± 1.2	5 ± 1.2	11.2 ± 1.2	4.264 ± 1.13	-0.3	1.41	1.57
$5_{4,2}$-$5_{3,3}$	5.7217	725	11	11	2.4	-37.8 ± 1.3	5 ± 1.2	23.4 ± 2.5	3.622 ± 0.894	-0.41	0.78	0.95
$4_{4,0}$-$4_{3,1}$	5.7281	552.2	9	9	1.6	-38.2 ± 1.4	5 ± 1.1	28.1 ± 3	2.968 ± 0.73	-0.5	0.68	0.84
$8_{3,6}$-$8_{2,7}$	5.732	1273.9	51	51	2.7	-39 ± 0.4	5.2 ± 0.4	23 ± 0.9	4.126 ± 0.356	-0.42	0.99	1.18
$3_{2,1}$-$2_{1,2}$	5.7477	114.4	15	21	2.7	-38.4 ± 1.5	5 ± 1.4	22.5 ± 2.9	4.512 ± 1.672	-0.21	1.68	1.83
$6_{4,2}$-$6_{3,3}$	5.755	951.6	13	13	3.2	-39.6 ± 1.3	5.7 ± 0.9	16.1 ± 1.8	3.518 ± 0.86	-0.54	0.77	0.94
$7_{2,6}$-$7_{1,7}$	5.7735	843.7	15	15	1.7	-39.2 ± 1.4	6 ± 1.3	34.2 ± 3.7	3.998 ± 0.956	-0.51	0.66	0.84
$7_{3,5}$-$7_{2,6}$	5.7792	1020.8	15	15	3.1	-40.3 ± 2.2	6 ± 1.3	14.8 ± 3	3.208 ± 1.396	-0.61	0.76	0.94
$10_{3,7}$-$10_{2,8}$	5.7995	2068.5	21	21	4.1	-37.9 ± 1.1	4.7 ± 0.9	6.5 ± 0.9	1.916 ± 0.594	-0.72	0.07	0.29
$7_{1,6}$-$7_{0,7}$	5.8022	843.3	45	45	1.8	-39.8 ± 0.7	5.2 ± 0.7	44.3 ± 2.7	5.176 ± 0.734	-0.29	1.16	1.34
$11_{4,7}$-$11_{3,8}$	5.805	2608.3	69	69	5.3	-37.5 ± 2.5	6 ± 2.4	5.9 ± 1.2	2.302 ± 1.03	-0.78	0.2	0.44
$8_{4,4}$-$8_{3,5}$	5.8088	1510.7	17	17	4.5	-36.1 ± 2	6 ± 1.9	7.7 ± 1.3	2.554 ± 0.908	-0.72	0.54	0.74

Table 10
(Continued)

Transition	λ (μm)	E_l (K)	g_l	g_u	A_{ul} (s^{-1})	$v_{\rm LSR}$ (km s^{-1})	σ_v (km s^{-1})	N_l ($\times 10^{15}$ cm^{-2})	W_v (km s^{-1})	log $_{10}(\tau_{p,\rm thin})$	log $_{10}(\tau_{p,\rm slab})$	log $_{10}(\beta_0)$
$9_{4,5}$-$9_{3,6}$	5.828	1845.5	57	57	5.2	−38.8 ± 0.8	5 ± 0.8	8.5 ± 0.6	3.164 ± 0.53	−0.53	0.82	1.03
$6_{0,6}$-$5_{1,5}$	5.8304	469.9	11	13	10.8	−38.3 ± 1.5	5 ± 1.2	6.7 ± 0.6	4.616 ± 1.3	−0.2	1.76	1.92
$6_{2,5}$-$6_{1,6}$	5.8342	643.4	39	39	2.1	−37.9 ± 1.1	5.3 ± 0.9	35.7 ± 2.9	4.734 ± 0.94	−0.29	1.36	1.53
$8_{2,6}$-$8_{1,7}$	5.838	1270	17	17	3.3	−38.1 ± 1.8	6 ± 1.3	16.8 ± 2.9	3.958 ± 1.54	−0.5	0.63	0.82
$5_{3,3}$-$5_{2,4}$	5.8473	598.7	11	11	3.5	−37.8 ± 2.5	5.7 ± 1.8	23.6 ± 4.5	5.438 ± 2.472	−0.31	1.08	1.25
$4_{3,2}$-$4_{2,3}$	5.867	432.1	27	27	3.2	−37.1 ± 0.8	5.1 ± 1.1	22.9 ± 2.2	4.512 ± 1.114	−0.26	1.6	1.76
$9_{3,6}$-$9_{2,7}$	5.8729	1729	57	57	5.2	−41.1 ± 1.7	6 ± 1.2	11.3 ± 1.4	4.166 ± 1.152	−0.48	0.93	1.14
$3_{3,1}$-$3_{2,2}$	5.8784	296.8	7	7	2.3	−38.8 ± 2.6	5.8 ± 1.4	39.9 ± 7.3	6.184 ± 2.748	−0.24	1	1.15
$8_{3,6}$-$7_{4,3}$	5.886	1339.6	45	51	1	−37.8 ± 1.9	6 ± 1.1	51.9 ± 8.4	4.242 ± 1.556	−0.46	0.54	0.73
$5_{2,4}$-$5_{1,5}$	5.8909	469.9	11	11	2.5	−38.5 ± 1	5 ± 0.7	21.5 ± 1.3	3.398 ± 0.544	−0.39	1.07	1.23
$7_{2,5}$-$7_{1,6}$	5.9228	1013	45	45	4.4	−38.6 ± 2	6 ± 1.2	19.6 ± 3.2	5.956 ± 2.322	−0.28	1.43	1.61
$8_{3,5}$-$8_{2,6}$	5.9246	1413.9	17	17	6.1	−39 ± 0.5	4.4 ± 0.5	6.6 ± 0.3	3.002 ± 0.32	−0.5	0.78	0.98
$7_{3,4}$-$7_{2,5}$	5.9507	1125.5	45	45	6.5	−40.7 ± 1.1	6 ± 0.8	14.7 ± 1.1	6.598 ± 1.186	−0.23	1.5	1.69
$6_{3,3}$-$6_{2,4}$	5.953	867.1	13	13	6	−40.1 ± 1.4	6 ± 0.9	16.9 ± 1.7	6.846 ± 1.746	−0.2	1.17	1.34
$6_{3,3}$-$5_{4,2}$	5.9792	877.7	11	13	0.7	−40.5 ± 1.1	4.8 ± 1.1	33.7 ± 3.7	2.364 ± 0.558	−0.66	0.26	0.44
$6_{2,4}$-$6_{1,5}$	5.9942	781	13	13	5.8	−39 ± 3.5	5 ± 2.2	10.9 ± 2.7	3.86 ± 2.648	−0.33	1.24	1.41
$6_{3,4}$-$5_{4,1}$	6.0191	878	33	39	0.7	−41.4 ± 1.3	4.5 ± 1.3	38.5 ± 5.3	2.534 ± 0.752	−0.6	0.71	0.89
$5_{2,3}$-$5_{1,4}$	6.0441	574.6	33	33	7.2	−36 ± 3	6 ± 2.6	17.8 ± 3.4	7.968 ± 4.292	−0.07	1.94	2.1
$4_{2,2}$-$4_{1,3}$	6.0702	396.3	9	9	7.7	−38.1 ± 1.4	5 ± 1.2	10.1 ± 0.9	4.852 ± 1.282	−0.2	1.57	1.73
$5_{3,2}$-$4_{4,1}$	6.0887	702.1	27	33	0.4	−39 ± 3.3	5 ± 2.1	71.9 ± 16.8	2.59 ± 1.304	−0.63	0.52	0.69
$2_{0,2}$-$1_{1,1}$	6.1432	53.4	3	5	3.8	−36.8 ± 2.1	5 ± 2.2	5 ± 1.1	2.496 ± 1.244	−0.47	1.34	1.49
$2_{0,2}$-$1_{1,1}$	6.1432	53.4	3	5	3.8	−36.9 ± 1.1	5 ± 1.4	6.7 ± 0.8	3.146 ± 0.964	−0.39	1.34	1.49
$5_{4,1}$-$6_{3,4}$	6.2388	933.6	39	33	0.3	−41.1 ± 2.5	6 ± 1.4	94.8 ± 20	2.496 ± 1.132	−0.72	0.33	0.51
$2_{0,2}$-$2_{1,1}$	6.3703	136.9	5	5	11	−37.7 ± 1.8	5 ± 1.6	9.1 ± 1.1	6.854 ± 2.386	0.05	1.78	1.92
$3_{1,2}$-$3_{2,1}$	6.4092	305.2	21	21	10	−36.6 ± 1.9	5 ± 2.3	4.4 ± 1	3.586 ± 2.17	−0.34	2.21	2.36
$6_{4,3}$-$7_{3,4}$	6.4266	1211.7	45	39	0.6	−38.7 ± 0.9	4.3 ± 0.8	31.9 ± 3.4	1.656 ± 0.368	−0.77	0.43	0.61
$5_{1,4}$-$5_{2,3}$	6.4335	642.3	33	33	11.5	−36.3 ± 0.6	5.3 ± 0.5	6.5 ± 0.3	5.772 ± 0.66	−0.19	2.16	2.33
$7_{2,5}$-$7_{3,4}$	6.4506	1211.7	45	45	12.5	−40.2 ± 1	5.7 ± 1	5.2 ± 0.4	5.852 ± 1.026	−0.28	1.81	2
$6_{2,4}$-$6_{3,3}$	6.4531	951.6	13	13	11.3	−39.4 ± 1	5.3 ± 0.7	4.3 ± 0.4	4.568 ± 0.998	−0.37	1.47	1.65
$10_{3,7}$-$10_{4,6}$	6.4691	2325.3	21	21	13.7	−40.4 ± 1.8	5.6 ± 1.5	2.7 ± 0.5	3.538 ± 1.44	−0.51	0.5	0.73
$8_{2,6}$-$8_{3,5}$	6.4697	1510.7	17	17	12.7	−41.3 ± 2.6	4.9 ± 2.1	2.6 ± 0.7	3.282 ± 2.008	−0.5	1.13	1.32
$5_{2,3}$-$5_{3,2}$	6.4718	731.9	33	33	9.4	−37.9 ± 1.4	5 ± 1.2	5.7 ± 0.7	4.4 ± 1.334	−0.25	2	2.17
$9_{3,6}$-$9_{4,5}$	6.4749	1956.7	57	57	12.7	−39.4 ± 1.4	4.5 ± 1.3	1.3 ± 0.2	1.628 ± 0.638	−0.81	1.24	1.45
$6_{1,5}$-$6_{2,4}$	6.4788	867.1	13	13	10.6	−40.2 ± 0.8	5.8 ± 0.9	6.2 ± 0.5	6.056 ± 1.178	−0.27	1.53	1.7
$11_{4,7}$-$11_{5,6}$	6.5067	2875.6	69	69	12.5	−39.2 ± 2.9	6 ± 1.8	3.1 ± 0.7	3.844 ± 1.968	−0.5	0.48	0.73
$11_{4,7}$-$11_{5,6}$	6.5067	2875.6	69	69	12.5	−39.2 ± 2	6 ± 1.9	3 ± 0.5	3.776 ± 1.28	−0.54	0.48	0.73
$9_{2,7}$-$9_{3,6}$	6.5126	1845.5	57	57	12.2	−38.4 ± 0.9	4.9 ± 0.7	3.3 ± 0.3	3.904 ± 0.794	−0.42	1.33	1.54
$7_{3,4}$-$7_{4,3}$	6.529	1339.6	45	45	9.5	−39.7 ± 1	4.6 ± 1	3.9 ± 0.4	3.61 ± 0.784	−0.42	1.59	1.78
$13_{5,8}$-$13_{6,7}$	6.5392	3965.1	81	81	12.5	−38.2 ± 1.6	5 ± 1.7	1.4 ± 0.2	1.864 ± 0.608	−0.79	−0.45	−0.16
$10_{4,6}$-$10_{5,5}$	6.5401	2481	21	21	11.1	−39.2 ± 2.6	6 ± 1.7	2.8 ± 0.6	3.208 ± 1.512	−0.61	0.28	0.51
$3_{2,2}$-$3_{3,1}$	6.5421	410.3	7	7	4.5	−37.2 ± 3.6	6 ± 2.9	11.8 ± 3.2	4.972 ± 3.204	−0.35	1.32	1.48
$3_{2,2}$-$3_{3,1}$	6.5421	410.3	7	7	4.5	−37.9 ± 2.8	5.2 ± 2.5	8.3 ± 2.3	3.72 ± 2.326	−0.47	1.32	1.48
$7_{1,6}$-$7_{2,5}$	6.5474	1125.5	45	45	9.5	−39.4 ± 1.4	5.3 ± 0.9	5.4 ± 0.6	4.88 ± 1.368	−0.33	1.79	1.97
$5_{3,3}$-$6_{2,4}$	6.5633	867.1	13	11	1.3	−37.4 ± 2.9	6 ± 1.8	45.2 ± 10.1	4.858 ± 2.524	−0.39	0.56	0.74
$5_{3,3}$-$6_{2,4}$	6.5633	867.1	13	11	1.3	−39 ± 0.9	4.5 ± 0.9	31.3 ± 2.7	3.47 ± 0.664	−0.43	0.56	0.74
$2_{0,2}$-$3_{1,3}$	6.5673	204.7	7	5	9.4	−36.3 ± 3.5	6 ± 3.1	4.8 ± 1.2	2.818 ± 1.822	−0.53	1.69	1.84
$13_{3,10}$-$13_{4,9}$	6.5832	3644.9	81	81	13.2	−40.8 ± 2.5	4 ± 2.5	0.6 ± 0.2	0.818 ± 0.512	−1.07	−0.13	0.15

Table 10
(Continued)

Transition	λ (μm)	E_l (K)	g_l	g_u	A_{ul} (s^{-1})	v_{LSR} (km s^{-1})	σ_v (km s^{-1})	N_l ($\times 10^{15}$ cm^{-2})	W_v (km s^{-1})	log $_{10}(\tau_{p,thin})$	log $_{10}(\tau_{p,slab})$	log $_{10}(\beta_0)$
$6_{3,4}$-$6_{4,3}$	6.6007	1088.6	39	39	7.5	−41.1 ± 1	5.5 ± 0.9	8.3 ± 0.6	5.988 ± 1.078	−0.24	1.67	1.86
$6_{3,4}$-$6_{4,3}$	6.6007	1088.6	39	39	7.5	−39.6 ± 1.4	5.4 ± 0.9	7.6 ± 0.9	5.454 ± 1.568	−0.27	1.67	1.86
$6_{3,4}$-$6_{4,3}$	6.6007	1088.6	39	39	7.5	−38.7 ± 1.2	5.4 ± 1.1	6.5 ± 0.6	4.852 ± 1.102	−0.35	1.67	1.86
$10_{4,7}$-$10_{5,6}$	6.6409	2472.4	63	63	10	−40.3 ± 1.9	4 ± 2	1.5 ± 0.4	1.69 ± 0.82	−0.73	0.74	0.97
$13_{5,9}$-$13_{6,8}$	6.6474	3953.2	27	27	11.4	−39.2 ± 2.3	4 ± 2.4	0.3 ± 0.1	0.358 ± 0.212	−1.44	−0.94	−0.65
$4_{1,4}$-$5_{0,5}$	6.6834	468	33	27	8.4	−38.5 ± 3.8	5 ± 2.6	5.3 ± 1.3	3.214 ± 2.032	−0.35	2.15	2.31
$12_{4,9}$-$12_{5,8}$	6.6867	3273.1	75	75	10.9	−43 ± 3.2	5.8 ± 3.1	1 ± 0.3	1.292 ± 0.716	−1.03	0.12	0.39
$10_{3,8}$-$10_{4,7}$	6.7052	2274.8	63	63	9.6	−38.9 ± 1.6	5 ± 1.3	2.3 ± 0.3	2.45 ± 0.798	−0.66	0.91	1.14
$10_{3,8}$-$10_{4,7}$	6.7052	2274.8	63	63	9.6	−40 ± 0.8	4.2 ± 0.9	2.6 ± 0.2	2.758 ± 0.55	−0.52	0.91	1.14
$6_{1,6}$-$6_{2,5}$	6.7121	795.4	39	39	4.9	−38.4 ± 3.1	5 ± 2.3	8.7 ± 1.8	3.778 ± 2.112	−0.33	1.78	1.95
$6_{3,4}$-$7_{2,5}$	6.7146	1125.5	45	39	1.9	−39.1 ± 1.1	4.9 ± 1.1	12.5 ± 1.4	2.382 ± 0.552	−0.66	1.07	1.26
$6_{3,4}$-$7_{2,5}$	6.7146	1125.5	45	39	1.9	−37.9 ± 0.8	4.2 ± 0.7	20 ± 1.8	3.554 ± 0.728	−0.37	1.07	1.26
$8_{2,7}$-$8_{3,6}$	6.7157	1447.3	51	51	7.7	−37.8 ± 1.6	4 ± 1.7	3.1 ± 0.6	2.59 ± 1.058	−0.52	1.49	1.69
$7_{0,7}$-$7_{1,6}$	6.7731	1013	45	45	4.7	−40.7 ± 0.8	5.1 ± 0.8	10.6 ± 0.7	5.24 ± 0.792	−0.28	1.64	1.82
$7_{0,7}$-$7_{1,6}$	6.7731	1013	45	45	4.7	−40.1 ± 0.9	6 ± 0.9	13.6 ± 0.8	6.604 ± 0.986	−0.23	1.64	1.82
$9_{2,8}$-$9_{3,7}$	6.7826	1749.6	19	19	7.5	−40.1 ± 1.8	4.3 ± 1.8	3 ± 0.6	2.588 ± 1.072	−0.56	0.79	1
$5_{0,5}$-$6_{1,6}$	6.7865	643.4	39	33	8.4	−36.2 ± 2.1	6 ± 1.7	6.8 ± 1	4.52 ± 1.762	−0.38	2.09	2.26
$7_{1,7}$-$7_{2,6}$	6.7959	1020.8	15	15	4.6	−40.9 ± 1.3	5.6 ± 1.1	8.6 ± 0.8	4.408 ± 0.96	−0.43	1.15	1.33
$7_{1,7}$-$7_{2,6}$	6.7959	1020.8	15	15	4.6	−39.2 ± 1	5.5 ± 0.9	9.2 ± 0.8	4.66 ± 0.888	−0.38	1.15	1.33
$10_{1,9}$-$10_{2,8}$	6.8251	2068.5	21	21	7.5	−39.4 ± 2.4	6 ± 1.4	5.6 ± 1	4.656 ± 1.922	−0.41	0.55	0.77
$10_{1,9}$-$10_{2,8}$	6.8251	2068.5	21	21	7.5	−38.3 ± 1.5	4 ± 1.3	2.4 ± 0.5	2.094 ± 0.992	−0.61	0.55	0.77
$6_{0,6}$-$7_{1,7}$	6.8714	843.7	15	13	8.1	−39.7 ± 1.6	5.6 ± 1	7.2 ± 1	5.482 ± 1.83	−0.29	1.51	1.68
$8_{0,8}$-$8_{1,7}$	6.8749	1270	17	17	4.4	−38.9 ± 0.9	5.2 ± 0.7	8.2 ± 0.7	4.068 ± 0.786	−0.41	0.97	1.16
$8_{1,8}$-$8_{2,7}$	6.8867	1273.9	51	51	4.4	−40.2 ± 0.7	6 ± 0.6	11.2 ± 0.6	5.538 ± 0.65	−0.33	1.44	1.63
$5_{1,4}$-$6_{2,5}$	6.9063	795.4	39	33	5.8	−38 ± 0.7	5.1 ± 0.6	9.9 ± 0.4	4.516 ± 0.572	−0.24	1.82	1.99
$7_{1,7}$-$8_{0,8}$	6.9588	1070.3	17	15	7.8	−40.7 ± 0.9	4.9 ± 0.9	4.7 ± 0.4	3.792 ± 0.712	−0.43	1.36	1.54
$7_{2,6}$-$8_{1,7}$	6.9655	1270	17	15	5.7	−39.5 ± 2.4	5.3 ± 2.1	4.6 ± 1.3	2.846 ± 1.706	−0.61	1.04	1.23
$9_{0,9}$-$9_{1,8}$	6.9774	1552.3	57	57	4.2	−40.9 ± 2.1	5.2 ± 2	8.6 ± 1.5	4.322 ± 1.704	−0.4	1.23	1.43
$9_{1,9}$-$9_{2,8}$	6.9833	1554.1	19	19	4.2	−38.8 ± 1	6 ± 1	7 ± 0.6	3.646 ± 0.65	−0.55	0.75	0.95
$8_{3,6}$-$9_{2,7}$	7.0015	1729	57	51	3.4	−39.9 ± 0.7	5.1 ± 0.7	9.1 ± 0.6	3.44 ± 0.492	−0.5	0.93	1.14
$12_{1,11}$-$12_{2,10}$	7.0134	2819.8	25	25	7.1	−39 ± 1.1	4.2 ± 0.9	1.6 ± 0.2	1.488 ± 0.462	−0.82	−0.06	0.19
$7_{1,6}$-$8_{2,7}$	7.0218	1273.9	51	45	5.9	−39.9 ± 0.8	6 ± 0.6	13.1 ± 0.7	7.484 ± 1.022	−0.15	1.54	1.73
$11_{0,11}$-$11_{1,10}$	7.1889	2193.5	69	69	4	−40.3 ± 1	6 ± 0.6	5.9 ± 0.5	3.17 ± 0.556	−0.61	0.74	0.96
$11_{1,11}$-$11_{2,10}$	7.1903	2193.9	23	23	4	−41.1 ± 1.1	6 ± 1	3.3 ± 0.3	1.838 ± 0.326	−0.88	0.26	0.49
$14_{2,13}$-$14_{3,12}$	7.2028	3670.3	87	87	6.9	−37.1 ± 1.4	4 ± 1.4	0.5 ± 0.1	0.5 ± 0.182	−1.29	−0.28	0
$10_{3,8}$-$11_{2,9}$	7.2356	2432	69	63	4.3	−38.5 ± 0.8	4.5 ± 0.6	2.6 ± 0.3	1.45 ± 0.32	−0.84	0.52	0.75
$12_{0,12}$-$12_{1,11}$	7.2995	2552.8	25	25	3.9	−39.3 ± 0.8	4 ± 0.9	1.1 ± 0.1	0.644 ± 0.136	−1.18	−0.02	0.22
$11_{2,10}$-$12_{1,11}$	7.3432	2552.8	25	23	5.6	−41.5 ± 2.9	5.4 ± 2.2	1.1 ± 0.3	0.858 ± 0.544	−1.18	0.1	0.34
$11_{2,9}$-$12_{3,10}$	7.3945	2823.1	75	69	4.6	−42.4 ± 3.8	6 ± 2	2.9 ± 0.9	1.848 ± 1.246	−0.88	0.25	0.5
$3_{0,3}$-$4_{3,2}$	7.4108	550.3	27	21	0.2	−38.7 ± 2	5 ± 1.9	96.9 ± 19.2	1.928 ± 0.806	−0.77	0.4	0.56
$12_{3,10}$-$13_{2,11}$	7.432	3232.2	81	75	4.5	−40.3 ± 1.6	6 ± 1.2	4.1 ± 0.5	2.6 ± 0.71	−0.71	−0.09	0.18
$12_{2,11}$-$13_{1,12}$	7.4401	2937.9	81	75	5.4	−39 ± 2.9	6 ± 2.7	2 ± 0.5	1.596 ± 0.796	−0.94	0.26	0.51
$9_{5,4}$-$10_{6,5}$	7.8984	2697.2	63	57	7.1	−36 ± 3.4	6 ± 2.6	1.8 ± 0.5	2.186 ± 1.348	−0.78	0.56	0.81

Table 11
Line Parameters of the −54.5 km s^{-1} Component ("H2") in the $\nu_2 = 1$–0 Transition

Transition	λ (μm)	E_l (K)	g_l	g_u	A_{ul} (s^{-1})	$v_{\rm LSR}$ (km s^{-1})	σ_v (km s^{-1})	N_l ($\times 10^{15}$ cm^{-2})	W_v (km s^{-1})	log $_{10}(\tau_{p,\rm thin})$	log $_{10}(\tau_{p,\rm slab})$	log $_{10}(\beta_0)$
$11_{2,10}$-$10_{1,9}$	5.4248	1860	21	23	10.2	−55.9 ± 1	5.4 ± 1.2	2.8 ± 0.4	1.83 ± 0.568	−0.78	0	0.19
$11_{6,5}$-$11_{5,6}$	5.4521	2875.6	69	69	2.4	−54.2 ± 1.7	5 ± 1.4	5.5 ± 0.8	0.812 ± 0.24	−1.17	−0.97	−0.68
$10_{1,9}$-$9_{2,8}$	5.4862	1554.1	19	21	9.5	−53.7 ± 1.3	5 ± 1.5	2.9 ± 0.4	1.84 ± 0.61	−0.78	0.19	0.36
$9_{2,7}$-$8_{3,6}$	5.5179	1447.3	51	57	4.6	−54.2 ± 1.1	5 ± 1.2	6.6 ± 0.8	2.08 ± 0.58	−0.73	0.4	0.55
$9_{1,8}$-$8_{2,7}$	5.5479	1273.9	51	57	8.7	−54 ± 1.4	5 ± 1.5	2.4 ± 0.4	1.458 ± 0.544	−0.87	0.82	0.96
$10_{5,6}$-$10_{4,7}$	5.5496	2274.8	63	63	2.7	−54.7 ± 2	5 ± 2.4	4.3 ± 1.1	0.778 ± 0.394	−1.19	−0.44	−0.2
$6_{5,1}$-$6_{4,2}$	5.5707	1090.1	13	13	1.8	−54.9 ± 2.4	5 ± 2.8	8.8 ± 2.9	1.022 ± 0.702	−1.04	−0.36	−0.23
$8_{2,7}$-$7_{1,6}$	5.5836	1013	45	51	7.9	−55.4 ± 3.2	7 ± 3.1	6.1 ± 1.8	3.4 ± 2.162	−0.62	0.95	1.07
$3_{3,1}$-$2_{2,0}$	5.6456	195.9	5	7	5.8	−54.5	7.5 ± 1.7	5 ± 0.5	2.782 ± 0.54	−0.74	0.62	0.67
$6_{2,5}$-$5_{1,4}$	5.6759	574.6	33	39	5.9	−54.5	9 ± 2.5	5.7 ± 0.8	2.732 ± 0.838	−0.85	1.08	1.16
$9_{3,7}$-$9_{2,8}$	5.6784	1554.1	19	19	2.3	−56.3 ± 2.4	5 ± 2.6	4.7 ± 1.3	0.772 ± 0.44	−1.2	−0.42	−0.25
$8_{4,5}$-$8_{3,6}$	5.6864	1447.3	51	51	3.1	−53.1 ± 2.2	5.4 ± 2.2	5.5 ± 1.5	1.194 ± 0.696	−0.96	0.22	0.38
$7_{1,6}$-$6_{2,5}$	5.6921	795.4	39	45	6.6	−54.5	7 ± 3	3.1 ± 0.7	1.744 ± 0.786	−0.89	1.01	1.11
$6_{4,3}$-$6_{3,4}$	5.7162	933.6	39	39	2.9	−54.3 ± 3	7 ± 2.4	9.2 ± 2	1.832 ± 0.862	−0.89	0.49	0.6
$5_{2,4}$-$4_{1,3}$	5.7187	396.3	9	11	5.2	−54.5	8.4 ± 2	5.7 ± 0.7	2.59 ± 0.626	−0.83	0.62	0.69
$4_{4,0}$-$4_{3,1}$	5.7281	552.2	9	9	1.6	−54.5	7 ± 4.5	10.8 ± 3.7	1.298 ± 0.894	−1.04	−0.09	−0.01
$8_{3,6}$-$8_{2,7}$	5.732	1273.9	51	51	2.7	−54.1 ± 0.9	5.6 ± 1.1	9.9 ± 1	1.856 ± 0.39	−0.83	0.31	0.45
$3_{2,1}$-$2_{1,2}$	5.7477	114.4	15	21	2.7	−54.5	8.3 ± 2.3	23.4 ± 3.9	6.044 ± 2.25	−0.44	0.86	0.9
$7_{2,6}$-$7_{1,7}$	5.7735	843.7	15	15	1.7	−53.8 ± 1.9	5 ± 1.9	15.8 ± 3.8	1.884 ± 0.982	−0.75	−0.07	0.03
$10_{3,7}$-$10_{2,8}$	5.7995	2068.5	21	21	4.1	−52.4 ± 2.8	7 ± 3.9	4.4 ± 1.4	1.328 ± 0.88	−1.1	−0.52	−0.3
$7_{1,6}$-$7_{0,7}$	5.8022	843.3	45	45	1.8	−54.3 ± 2.5	5 ± 2.9	10 ± 3.1	1.238 ± 0.842	−0.95	0.43	0.53
$8_{4,4}$-$8_{3,5}$	5.8088	1510.7	17	17	4.5	−50.6 ± 2.4	5.1 ± 2.1	4.4 ± 1.2	1.464 ± 0.822	−0.88	−0.12	0.05
$6_{3,4}$-$6_{2,5}$	5.818	795.4	39	39	3.4	−54.5	7 ± 3.9	6.5 ± 1.5	1.634 ± 0.802	−0.99	0.69	0.79
$6_{1,6}$-$5_{0,5}$	5.8227	468	33	39	10.8	−54.5	7 ± 2.3	4.9 ± 0.8	4.474 ± 1.58	−0.45	1.46	1.53
$9_{4,5}$-$9_{3,6}$	5.828	1845.5	57	57	5.2	−53.3 ± 1.6	5.3 ± 1.9	3.9 ± 0.7	1.488 ± 0.604	−0.91	0.21	0.4
$6_{2,5}$-$6_{1,6}$	5.8342	643.4	39	39	2.1	−54.5	7 ± 3.1	12.8 ± 3	2.086 ± 0.996	−0.83	0.6	0.69
$2_{2,0}$-$1_{1,1}$	5.8605	53.4	3	5	5	−54.5	7 ± 2.5	4.2 ± 0.7	2.6 ± 0.992	−0.65	0.57	0.6
$4_{3,2}$-$4_{2,3}$	5.867	432.1	27	27	3.2	−54.5	9 ± 4.7	9.8 ± 2.7	2.452 ± 1.42	−0.82	0.81	0.88
$3_{3,1}$-$3_{2,2}$	5.8784	296.8	7	7	2.3	−54.5	7 ± 3.1	12.4 ± 2.9	2.212 ± 1.084	−0.83	0.2	0.25
$8_{3,5}$-$8_{2,6}$	5.9246	1413.9	17	17	6.1	−53.5 ± 1.7	5 ± 2.1	1.8 ± 0.4	0.88 ± 0.384	−1.13	0.12	0.27
$5_{1,4}$-$5_{0,5}$	5.9683	468	33	33	3	−54.5	9 ± 1.9	19.9 ± 2.1	4.712 ± 1.094	−0.61	0.87	0.94
$4_{2,2}$-$4_{1,3}$	6.0702	396.3	9	9	7.7	−54.5	7 ± 4.6	1.8 ± 0.5	1.24 ± 0.742	−0.95	0.79	0.85
$3_{1,2}$-$3_{0,3}$	6.1138	196.7	21	21	6.4	−54.5	8 ± 4.2	6.5 ± 1.3	3.522 ± 1.546	−0.62	1.24	1.29
$2_{0,2}$-$1_{1,1}$	6.1432	53.4	3	5	3.8	−54.5	7 ± 2.7	5.9 ± 1	3.196 ± 1.124	−0.57	0.51	0.54
$2_{0,2}$-$1_{1,1}$	6.1432	53.4	3	5	3.8	−54.5	7.6 ± 1.4	7.7 ± 0.6	4.106 ± 0.748	−0.53	0.51	0.54
$4_{2,3}$-$3_{3,0}$	6.163	410.6	21	27	0.4	−54.5	7 ± 1.5	47.2 ± 4.6	2.408 ± 0.5	−0.8	0.04	0.1
$2_{0,2}$-$2_{1,1}$	6.3703	136.9	5	5	11	−54.5	7.2 ± 1.9	8.2 ± 0.7	6.876 ± 1.57	−0.24	0.96	1
$5_{1,4}$-$5_{2,3}$	6.4335	642.3	33	33	11.5	−54.5	7 ± 1.2	3.4 ± 0.3	3.808 ± 0.748	−0.57	1.41	1.49
$7_{2,5}$-$7_{3,4}$	6.4506	1211.7	45	45	12.5	−55.2 ± 2.9	5 ± 2.9	1.1 ± 0.3	1.372 ± 0.92	−0.88	1.12	1.26
$10_{3,7}$-$10_{4,6}$	6.4691	2325.3	21	21	13.7	−55.9 ± 3.1	7 ± 3.1	1.8 ± 0.4	2.526 ± 1.32	−0.79	−0.06	0.18
$5_{2,3}$-$5_{3,2}$	6.4718	731.9	33	33	9.4	−54.5	9 ± 4	6.7 ± 1.9	6.204 ± 3.91	−0.47	1.25	1.35
$2_{1,2}$-$3_{0,3}$	6.4922	196.7	21	15	7.2	−54.5	7 ± 1.5	16.4 ± 1.1	6.908 ± 1.274	−0.21	1.23	1.27
$13_{3,10}$-$13_{4,9}$	6.5832	3644.9	81	81	13.2	−50.5 ± 6.1	5 ± 2.6	1.6 ± 0.4	2.2 ± 1.252	−0.71	−0.52	−0.16
$13_{5,9}$-$13_{6,8}$	6.6474	3953.2	27	27	11.4	−54.7 ± 3.5	5 ± 3	0.4 ± 0.1	0.476 ± 0.306	−1.41	−1.3	−0.91
$4_{1,4}$-$5_{0,5}$	6.6834	468	33	27	8.4	−54.5	7 ± 2.6	3.6 ± 0.6	2.75 ± 0.912	−0.67	1.37	1.44
$12_{4,9}$-$12_{5,8}$	6.6867	3273.1	75	75	10.9	−58.5 ± 4	5 ± 2.3	1.3 ± 0.4	1.656 ± 1.008	−0.84	−0.32	0.01
$10_{3,8}$-$10_{4,7}$	6.7052	2274.8	63	63	9.6	−53.4 ± 2.9	5.7 ± 3.1	1.2 ± 0.3	1.324 ± 0.79	−1	0.35	0.59

Table 11
(Continued)

Transition	λ (μm)	E_l (K)	g_l	g_u	A_{ul} (s^{-1})	v_{LSR} (km s^{-1})	σ_v (km s^{-1})	N_l ($\times 10^{15}$ cm^{-2})	W_v (km s^{-1})	log $_{10}(\tau_{p,thin})$	log $_{10}(\tau_{p,slab})$	log $_{10}(\beta_0)$
$7_{0,7}$-$7_{1,6}$	6.7731	1013	45	45	4.7	−55.4 ± 2	5 ± 2.5	3.2 ± 0.8	1.68 ± 0.954	−0.82	0.92	1.04
$7_{0,7}$-$7_{1,6}$	6.7731	1013	45	45	4.7	−55.6 ± 2	5 ± 2.5	3.5 ± 0.9	1.782 ± 1.084	−0.77	0.92	1.04
$8_{0,8}$-$8_{1,7}$	6.8749	1270	17	17	4.4	−54.4 ± 1.6	7 ± 1.7	5.8 ± 0.7	3.064 ± 0.81	−0.71	0.29	0.43
$5_{1,4}$-$6_{2,5}$	6.9063	795.4	39	33	5.8	−54.5	7.9 ± 2.3	4.2 ± 0.7	2.588 ± 0.916	−0.75	1.08	1.17
$7_{1,7}$-$8_{0,8}$	6.9588	1070.3	17	15	7.8	−55.5 ± 2.1	5 ± 2.8	1.8 ± 0.5	1.538 ± 0.974	−0.87	0.65	0.77
$9_{1,9}$-$9_{2,8}$	6.9833	1554.1	19	19	4.2	−53.8 ± 1.9	5 ± 2.1	2.2 ± 0.6	1.184 ± 0.64	−0.95	0.11	0.27
$3_{2,2}$-$4_{3,1}$	6.9933	552.2	9	7	8.6	−54.5	9 ± 2.2	6.4 ± 0.8	5.314 ± 1.42	−0.56	0.78	0.86
$8_{3,6}$-$9_{2,7}$	7.0015	1729	57	51	3.4	−54.4 ± 2	5 ± 2.4	2.7 ± 0.7	1.052 ± 0.558	−1.03	0.31	0.49
$7_{1,6}$-$8_{2,7}$	7.0218	1273.9	51	45	5.9	−54.4 ± 1.6	5.6 ± 1.6	4 ± 0.7	2.494 ± 0.988	−0.64	0.86	1
$3_{3,0}$-$4_{4,1}$	7.0447	702.1	27	21	14.2	−54.5	7 ± 4.1	1.8 ± 0.6	2.624 ± 1.702	−0.75	1.37	1.46
$4_{2,3}$-$5_{3,2}$	7.1469	731.9	33	27	5.6	−54.5	7 ± 2.3	4 ± 0.6	2.574 ± 0.848	−0.72	1.07	1.17
$11_{0,11}$-$11_{1,10}$	7.1889	2193.5	69	69	4	−54.8 ± 2.1	6.5 ± 2.4	2.3 ± 0.6	1.312 ± 0.716	−1.02	0.17	0.39
$14_{2,13}$-$14_{3,12}$	7.2028	3670.3	87	87	6.9	−51.6 ± 2.5	5 ± 2.7	0.4 ± 0.1	0.414 ± 0.22	−1.47	−0.67	−0.31
$10_{3,8}$-$11_{2,9}$	7.2356	2432	69	63	4.3	−53 ± 2	7 ± 2.9	1.8 ± 0.4	1.038 ± 0.502	−1.21	−0.02	0.23
$12_{3,10}$-$13_{2,11}$	7.432	3232.2	81	75	4.5	−54.8 ± 2.9	5.8 ± 2.7	1.6 ± 0.5	1.054 ± 0.694	−1.07	−0.53	−0.21
$9_{5,4}$-$10_{6,5}$	7.8984	2697.2	63	57	7.1	−50.5 ± 3.6	5.9 ± 2.5	1.8 ± 0.5	2.176 ± 1.316	−0.78	0.05	0.33

Table 12
Line Parameters of the −45 km s^{-1} Component ("W") in the ν_2 = 1–0 Transition

Transition	λ (μm)	E_l (K)	g_l	g_u	A_{ul} (s^{-1})	$v_{\rm LSR}$ (km s^{-1})	σ_v (km s^{-1})	N_l (×10^{15} cm^{-2})	W_v (km s^{-1})	log $_{10}(\tau_{p,\rm thin})$
$7_{1,6}$-$6_{2,5}$	5.6921	795.4	39	45	6.6	−45	5 ± 2.5	2.9 ± 0.8	1.434 ± 0.838	−0.44
$6_{0,6}$-$5_{1,5}$	5.8304	469.9	11	13	10.8	−45	4.7 ± 1.8	2.6 ± 0.7	2.488 ± 1.322	−0.25
$4_{3,2}$-$4_{2,3}$	5.867	432.1	27	27	3.2	−45	5 ± 1.8	10.3 ± 1.7	2.33 ± 0.868	−0.36
$5_{2,4}$-$5_{1,5}$	5.8909	469.9	11	11	2.5	−45	5 ± 1.5	8.1 ± 1.3	1.786 ± 0.526	−0.5
$4_{2,2}$-$4_{1,3}$	6.0702	396.3	9	9	7.7	−45	5 ± 2.4	3.8 ± 0.9	2.594 ± 1.236	−0.31
$2_{0,2}$-$1_{1,1}$	6.1432	53.4	3	5	3.8	−45	5 ± 1.9	9.2 ± 1.4	4 ± 1.572	−0.23
$2_{0,2}$-$1_{1,1}$	6.1432	53.4	3	5	3.8	−45	4.6 ± 0.8	9.7 ± 0.7	4 ± 0.856	−0.14
$2_{0,2}$-$2_{1,1}$	6.3703	136.9	5	5	11	−45	5 ± 3.3	5.2 ± 1.2	3.896 ± 2.656	0.03
$3_{1,2}$-$3_{2,1}$	6.4092	305.2	21	21	10	−45	4.3 ± 1.6	4.7 ± 0.8	3.334 ± 1.648	−0.13
$5_{1,4}$-$5_{2,3}$	6.4335	642.3	33	33	11.5	−45	4 ± 0.5	3.7 ± 0.3	3.33 ± 0.662	−0.12
$2_{0,2}$-$3_{1,3}$	6.5673	204.7	7	5	9.4	−45	5 ± 1.5	5.5 ± 1.2	3.88 ± 1.854	−0.33
$5_{0,5}$-$6_{1,6}$	6.7865	643.4	39	33	8.4	−45	4.7 ± 1.5	3 ± 0.9	2.788 ± 1.618	−0.38
$5_{1,4}$-$6_{2,5}$	6.9063	795.4	39	33	5.8	−45	4.9 ± 0.9	4 ± 0.4	2.436 ± 0.566	−0.29

Table 13
Line Parameters of the −39.5 km s^{-1} Component ("H1") in the ν_2 = 2–1 Transition

Transition	λ (μm)	E_l (K)	g_l	g_u	A_{ul} (s^{-1})	$v_{\rm LSR}$ (km s^{-1})	σ_v (km s^{-1})	N_l (×10^{15} cm^{-2})	W_v (km s^{-1})	log $_{10}(\tau_{p,\rm thin})$	log $_{10}(\tau_{p,\rm slab})$	log $_{10}(\beta_0)$
$4_{4,1}$-$3_{3,0}$	5.4373	2744.1	21	27	9.8	−38.7 ± 1.5	4.8 ± 1.2	2.1 ± 0.6	1.596 ± 0.906	−0.85	−1.62	−1.15
$5_{3,2}$-$4_{2,3}$	5.5105	2744.7	27	33	6.1	−37.6 ± 4.8	6 ± 2.8	3.5 ± 1.5	1.668 ± 1.538	−0.92	−1.72	−1.25
$4_{3,2}$-$3_{2,1}$	5.6226	2617.1	21	27	8.6	−41.3 ± 2.7	4.4 ± 2.7	1.4 ± 1	1.044 ± 1.516	−1	−1.54	−1.08
$9_{2,8}$-$8_{1,7}$	5.6247	3582.4	17	19	16.1	−38.2 ± 3.5	4 ± 3.8	0.4 ± 0.3	0.49 ± 0.838	−1.3	−2.07	−1.57
$11_{0,11}$-$10_{1,10}$	5.667	3891.4	63	69	27.6	−36 ± 2.2	5.5 ± 1.6	0.9 ± 0.2	1.834 ± 0.83	−0.82	−1.47	−0.96
$11_{0,11}$-$10_{1,10}$	5.667	3891.4	63	69	27.6	−40.2 ± 3.1	5.2 ± 2	1 ± 0.3	1.928 ± 1.248	−0.77	−1.47	−0.96
$6_{2,5}$-$5_{1,4}$	5.7627	2878.3	33	39	10.9	−38.5 ± 3.8	6 ± 2.2	2.4 ± 0.8	2.148 ± 1.578	−0.78	−1.43	−0.96
$9_{1,9}$-$8_{0,8}$	5.7754	3362.5	17	19	25.2	−37.4 ± 1.5	4.6 ± 1.2	0.8 ± 0.2	1.546 ± 0.65	−0.81	−1.69	−1.2
$9_{0,9}$-$8_{1,8}$	5.7769	3362.7	51	57	25.2	−39.9 ± 2.8	5 ± 2.7	0.8 ± 0.6	1.598 ± 2.53	−0.87	−1.22	−0.73
$8_{3,6}$-$8_{2,7}$	5.7823	3589.3	51	51	5.3	−40.2 ± 10.6	6 ± 5.9	5.7 ± 5.1	2.138 ± 4.148	−0.79	−2.09	−1.6
$7_{4,3}$-$7_{3,4}$	5.7954	3542.9	45	45	6.4	−40.5 ± 2.2	4.2 ± 1.9	2.6 ± 0.8	1.214 ± 0.826	−0.91	−2.03	−1.53
$8_{1,8}$-$7_{0,7}$	5.8322	3136.9	45	51	23.9	−38.5 ± 2.2	4.9 ± 1.5	0.7 ± 0.2	1.462 ± 0.66	−0.87	−1.12	−0.65
$4_{2,3}$-$3_{1,2}$	5.8491	2549.6	21	27	9.1	−40 ± 1.4	4.1 ± 1.2	2.2 ± 0.6	1.856 ± 1.036	−0.68	−1.42	−0.97
$4_{2,3}$-$3_{1,2}$	5.8491	2549.6	21	27	9.1	−40 ± 1.4	4.1 ± 1.2	2.2 ± 0.6	1.856 ± 1.036	−0.68	−1.42	−0.97
$3_{2,2}$-$2_{1,1}$	5.9031	2436.3	5	7	9.5	−36 ± 3.5	6 ± 2.5	1.4 ± 0.6	1.468 ± 1.408	−0.96	−1.91	−1.45
$6_{2,5}$-$6_{1,6}$	5.9052	2938.5	39	39	4.2	−37.8 ± 2.1	4 ± 1.9	2.3 ± 0.7	0.756 ± 0.466	−1.09	−1.85	−1.38
$6_{1,6}$-$5_{0,5}$	5.9485	2763	33	39	20.7	−36.9 ± 1.1	4.8 ± 0.9	1.3 ± 0.2	2.392 ± 0.714	−0.63	−1.03	−0.56
$6_{0,6}$-$5_{1,5}$	5.9622	2766	11	13	20.6	−39.2 ± 3.2	5.1 ± 2.2	0.8 ± 0.3	1.51 ± 1.15	−0.9	−1.51	−1.04
$6_{0,6}$-$5_{1,5}$	5.9622	2766	11	13	20.6	−39.2 ± 3.2	5.1 ± 2.2	0.8 ± 0.3	1.51 ± 1.15	−0.9	−1.51	−1.04
$5_{3,2}$-$5_{2,3}$	5.9925	2954.6	33	33	8.7	−38.3 ± 1.8	4.1 ± 1.9	3.2 ± 1.5	2.142 ± 2.218	−0.63	−1.6	−1.12
$5_{1,5}$-$4_{0,4}$	6.0059	2614.4	9	11	18.8	−39.2 ± 1.5	4 ± 1.7	0.6 ± 0.3	1.122 ± 1.028	−0.84	−1.51	−1.05
$4_{2,3}$-$4_{1,4}$	6.0224	2620.4	27	27	5.9	−36 ± 13.3	6 ± 7.7	3.5 ± 4.7	1.672 ± 4.8	−0.86	−1.62	−1.16
$4_{2,3}$-$4_{1,4}$	6.0224	2620.4	27	27	5.9	−39.8 ± 5.2	6 ± 2.8	6.1 ± 2.7	2.824 ± 2.71	−0.65	−1.62	−1.16
$7_{3,4}$-$7_{2,5}$	6.0232	3441.8	45	45	11.7	−36 ± 2.5	4 ± 2.6	0.9 ± 0.6	0.84 ± 1.18	−1.06	−1.65	−1.16
$4_{1,4}$-$3_{0,3}$	6.0613	2491.3	21	27	16.6	−39.4 ± 0.9	4.5 ± 0.6	1.2 ± 0.1	2.058 ± 0.48	−0.66	−1.08	−0.62
$5_{1,4}$-$5_{0,5}$	6.0802	2763	33	33	6.4	−37 ± 2.6	5.6 ± 1.8	4.4 ± 2	2.31 ± 2.332	−0.72	−1.58	−1.11
$2_{2,1}$-$2_{1,2}$	6.101	2412.5	15	15	5.9	−37.8 ± 1.8	4.4 ± 1.4	1.8 ± 0.4	0.906 ± 0.396	−1.05	−1.72	−1.27
$5_{2,3}$-$5_{1,4}$	6.1498	2878.3	33	33	14.1	−39.6 ± 9.1	4.9 ± 6.3	1.4 ± 1.5	1.696 ± 3.84	−0.83	−1.3	−0.83
$4_{1,3}$-$4_{0,4}$	6.1686	2614.4	9	9	9.2	−38 ± 3.4	4 ± 4	0.7 ± 0.7	0.566 ± 1.148	−1.22	−1.87	−1.41
$3_{2,1}$-$3_{1,2}$	6.1716	2549.6	21	21	12.5	−38.3 ± 2.3	4 ± 2.8	1.3 ± 1.1	1.414 ± 2.464	−0.82	−1.33	−0.87
$2_{1,2}$-$1_{0,1}$	6.1753	2328.3	9	15	13.9	−40.9 ± 1.4	4.8 ± 1	1.2 ± 0.2	2.402 ± 0.89	−0.65	−1.28	−0.83
$2_{1,2}$-$1_{0,1}$	6.1753	2328.3	9	15	13.9	−39.2 ± 1.7	5.3 ± 1.3	1.4 ± 0.4	2.66 ± 1.692	−0.61	−1.28	−0.83
$3_{0,3}$-$2_{1,2}$	6.2028	2412.5	15	21	11.8	−39 ± 4.4	6 ± 2.5	3.5 ± 2.1	4.488 ± 6.678	−0.4	−1.25	−0.8
$3_{1,2}$-$3_{0,3}$	6.2394	2491.3	21	21	13.2	−38.6 ± 1.6	4.2 ± 1.9	1.3 ± 0.6	1.504 ± 1.524	−0.78	−1.25	−0.79
$2_{1,1}$-$2_{0,2}$	6.2878	2395.1	5	5	17.7	−40.2 ± 4.9	6 ± 3.3	1.8 ± 0.8	2.782 ± 2.976	−0.67	−1.67	−1.22
$2_{1,1}$-$2_{0,2}$	6.2878	2395.1	5	5	17.7	−40.5 ± 1.4	4 ± 1.2	1.2 ± 0.2	1.902 ± 0.778	−0.68	−1.67	−1.22
$1_{1,0}$-$1_{0,1}$	6.3157	2328.3	9	9	21.3	−39.4 ± 2.6	4 ± 2.4	0.4 ± 0.1	0.802 ± 0.608	−1.07	−1.29	−0.84
$1_{1,0}$-$1_{0,1}$	6.3157	2328.3	9	9	21.3	−39.2 ± 2.7	5.6 ± 1.9	1.5 ± 0.4	2.932 ± 1.566	−0.61	−1.29	−0.84
$1_{0,1}$-$1_{1,0}$	6.5149	2359.9	9	9	24.9	−38.5 ± 3.3	4 ± 4	0.4 ± 0.4	0.984 ± 2.182	−0.97	−1.2	−0.75
$3_{1,2}$-$3_{2,1}$	6.5994	2617.1	21	21	19.1	−39.5 ± 5.3	6 ± 3.2	1.6 ± 0.7	3.24 ± 2.988	−0.56	−1.1	−0.64

Table 13
(Continued)

Transition	λ (μm)	E_l (K)	g_l	g_u	A_{ul} (s^{-1})	$v_{\rm LSR}$ (km s^{-1})	σ_v (km s^{-1})	N_l ($\times 10^{15}$ cm^{-2})	W_v (km s^{-1})	log $_{10}(\tau_{p,\rm thin})$	log $_{10}(\tau_{p,\rm slab})$	log $_{10}(\beta_0)$
$3_{1,2}$-$3_{2,1}$	6.5994	2617.1	21	21	19.1	−38.1 ± 3.1	4 ± 2.7	0.7 ± 0.3	1.4 ± 1.224	−0.77	−1.1	−0.64
$5_{1,4}$-$5_{2,3}$	6.616	2954.6	33	33	23.3	−38.5 ± 1.2	4.2 ± 1	0.9 ± 0.2	2.212 ± 0.82	−0.6	−1.04	−0.57
$2_{1,2}$-$3_{0,3}$	6.64	2491.3	21	15	13.5	−37.5 ± 2.7	4.2 ± 3.1	1.5 ± 1.1	1.544 ± 2.39	−0.79	−1.31	−0.85
$7_{2,5}$-$7_{3,4}$	6.6462	3542.9	45	45	24.3	−37.5 ± 6.2	6 ± 5.3	0.6 ± 0.5	1.632 ± 2.7	−0.92	−1.27	−0.78
$7_{2,5}$-$7_{3,4}$	6.6462	3542.9	45	45	24.3	−36 ± 6.6	6 ± 4	0.7 ± 0.4	1.888 ± 2.512	−0.86	−1.27	−0.78
$6_{2,4}$-$6_{3,3}$	6.6574	3283.5	13	13	21.5	−40 ± 15.1	6 ± 12.7	0.6 ± 1.3	1.554 ± 6.392	−0.95	−1.69	−1.2
$4_{0,4}$-$4_{1,3}$	6.6674	2697.9	9	9	15.1	−38.4 ± 6.1	5.6 ± 4.2	1.6 ± 1.5	2.628 ± 5.308	−0.68	−1.61	−1.15
$4_{2,2}$-$4_{3,1}$	6.7113	2885.5	9	9	13.9	−42.1 ± 8.3	4 ± 8.1	0.2 ± 0.4	0.368 ± 1.412	−1.42	−1.76	−1.29
$7_{1,6}$-$7_{2,5}$	6.7261	3441.8	45	45	20.3	−38.9 ± 2.6	4 ± 2.7	0.6 ± 0.4	1.47 ± 1.926	−0.8	−1.27	−0.78
$3_{2,1}$-$3_{3,0}$	6.7334	2744.1	21	21	9.1	−38.6 ± 2.6	4.5 ± 2.4	1.3 ± 0.7	1.328 ± 1.494	−0.85	−1.48	−1.01
$2_{0,2}$-$3_{1,3}$	6.7455	2502.3	7	5	18.4	−37.7 ± 2.5	4 ± 2.2	1.1 ± 0.4	1.608 ± 1.372	−0.72	−1.63	−1.18
$7_{3,4}$-$7_{4,3}$	6.7536	3700	45	45	18	−36 ± 4	4 ± 3.8	0.2 ± 0.1	0.484 ± 0.588	−1.26	−1.49	−0.99
$5_{0,5}$-$5_{1,4}$	6.7653	2878.3	33	33	12.5	−38.5 ± 5	6 ± 2.9	1.9 ± 1.5	2.656 ± 4.578	−0.71	−1.23	−0.76
$4_{2,3}$-$4_{3,2}$	6.7693	2883.9	27	27	12.6	−38.7 ± 7.1	6 ± 4	1.1 ± 1.1	1.614 ± 3.308	−0.94	−1.32	−0.84
$6_{3,3}$-$6_{4,2}$	6.7814	3451.2	13	13	15.2	−36 ± 2.3	4 ± 2.2	0.4 ± 0.1	0.742 ± 0.518	−1.09	−1.93	−1.44
$4_{1,4}$-$4_{2,3}$	6.7857	2744.7	27	27	11.1	−37 ± 1.8	4.2 ± 1.8	1.1 ± 0.3	1.412 ± 0.934	−0.82	−1.27	−0.81
$5_{3,2}$-$5_{4,1}$	6.7987	3239.3	33	33	12.1	−37.6 ± 6.5	6 ± 3.8	0.9 ± 0.5	1.262 ± 1.6	−1.05	−1.48	−1
$9_{4,5}$-$9_{5,4}$	6.7993	4518.4	57	57	18.6	−36.9 ± 6.5	4 ± 4.4	0.2 ± 0.2	0.452 ± 0.944	−1.33	−1.9	−1.37
$3_{0,3}$-$4_{1,4}$	6.8136	2620.4	27	21	17.1	−39.9 ± 4.3	5.7 ± 3.3	1.6 ± 0.8	2.424 ± 2.61	−0.73	−1.11	−0.65
$3_{0,3}$-$4_{1,4}$	6.8136	2620.4	27	21	17.1	−39.8 ± 2.7	5.1 ± 2.3	1.5 ± 0.9	2.254 ± 3.024	−0.67	−1.11	−0.65
$3_{0,3}$-$4_{1,4}$	6.8136	2620.4	27	21	17.1	−38.9 ± 2.2	4.6 ± 2	1 ± 0.4	1.504 ± 1.394	−0.85	−1.11	−0.65
$8_{1,7}$-$8_{2,6}$	6.8165	3734.1	17	17	18.4	−36 ± 11.6	6 ± 7.6	0.5 ± 1	1.168 ± 4.75	−1.03	−1.91	−1.41
$6_{3,4}$-$6_{4,3}$	6.8186	3450.1	39	39	14.6	−37.8 ± 2	4 ± 2.2	0.6 ± 0.3	1.114 ± 1.146	−0.93	−1.46	−0.97
$7_{4,3}$-$7_{5,2}$	6.8295	3918.7	45	45	14	−40 ± 8.2	6 ± 4.5	1.2 ± 0.9	2.046 ± 3.154	−0.81	−1.73	−1.22
$9_{5,4}$-$9_{6,3}$	6.8322	4777.3	57	57	15.4	−36 ± 7.3	6 ± 4.4	0.8 ± 0.6	1.556 ± 2.25	−0.91	−2.15	−1.61
$8_{4,5}$-$8_{5,4}$	6.8395	4199.9	51	51	16.1	−37.3 ± 6.7	6 ± 5.6	0.8 ± 0.7	1.526 ± 2.828	−0.95	−1.79	−1.28
$4_{1,4}$-$5_{0,5}$	6.8449	2763	33	27	16	−39.3 ± 1.4	5.1 ± 1	1.9 ± 0.3	2.832 ± 0.916	−0.58	−1.12	−0.65
$8_{3,6}$-$8_{4,5}$	6.8498	3977	51	51	17.9	−36.2 ± 3.3	4 ± 3.5	0.7 ± 0.5	1.4 ± 2.26	−0.77	−1.6	−1.09
$1_{1,0}$-$2_{2,1}$	6.8512	2506.3	15	9	26	−43 ± 3	6 ± 2.1	1.5 ± 0.7	2.656 ± 2.634	−0.62	−1.21	−0.76
$6_{0,6}$-$6_{1,5}$	6.8786	3087.4	13	13	10.9	−39.5 ± 7.4	5.7 ± 5.8	0.8 ± 1	1.07 ± 2.902	−1.1	−1.81	−1.33
$1_{1,1}$-$2_{2,0}$	6.8842	2508	5	3	22.5	−41 ± 3	4.4 ± 2.7	0.7 ± 0.4	1.13 ± 1.474	−0.91	−1.75	−1.29
$4_{0,4}$-$5_{1,5}$	6.8848	2766	11	9	16.6	−40.1 ± 3	5.1 ± 2.4	1.7 ± 0.9	2.734 ± 3.308	−0.62	−1.57	−1.11
$3_{1,2}$-$4_{2,3}$	7.0096	2744.7	27	21	13.1	−38.2 ± 1.1	4 ± 1.3	1.4 ± 0.4	1.714 ± 1.016	−0.66	−1.27	−0.8
$6_{1,6}$-$7_{0,7}$	7.0362	3136.9	45	39	15.6	−39.3 ± 3.4	6 ± 2	1.3 ± 0.6	2.254 ± 2.234	−0.7	−1.18	−0.7
$3_{2,1}$-$4_{3,2}$	7.205	2883.9	27	21	18.3	−39 ± 4	5.5 ± 2.9	0.6 ± 0.5	1.284 ± 2.078	−1.01	−1.18	−0.71
$7_{1,6}$-$8_{2,7}$	7.2245	3589.3	51	45	11.1	−38.8 ± 1.7	5.1 ± 1.4	0.6 ± 0.2	0.804 ± 0.614	−1.18	−1.53	−1.04
$8_{0,8}$-$9_{1,9}$	7.2337	3614.1	19	17	14.5	−39 ± 1.1	5 ± 0.8	0.4 ± 0.1	0.774 ± 0.31	−1.11	−1.85	−1.36
$3_{2,2}$-$4_{3,1}$	7.2371	2885.5	9	7	17.5	−38.9 ± 1.1	6 ± 0.7	0.6 ± 0.1	1.204 ± 0.242	−1.07	−1.67	−1.2
$3_{2,2}$-$4_{3,1}$	7.2371	2885.5	9	7	17.5	−38.9 ± 1.1	6 ± 0.7	0.6 ± 0.1	1.204 ± 0.242	−1.07	−1.67	−1.2
$3_{3,0}$-$4_{4,1}$	7.2937	3063.4	27	21	28.4	−39.9 ± 1.5	5.8 ± 0.9	0.5 ± 0.1	1.736 ± 0.524	−0.88	−1.09	−0.62
$4_{2,3}$-$5_{3,2}$	7.3988	3064.7	33	27	11.9	−40.8 ± 2.2	5 ± 2.7	1.1 ± 0.8	1.564 ± 2.496	−0.87	−1.35	−0.87
$4_{3,2}$-$5_{4,1}$	7.4294	3239.3	33	27	20.8	−36 ± 2.3	6 ± 1.5	0.8 ± 0.3	2.018 ± 1.668	−0.76	−1.21	−0.73
$10_{1,10}$-$11_{0,11}$	7.4372	4194.5	69	63	13.2	−38.1 ± 1.7	4.1 ± 1.7	0.3 ± 0.1	0.516 ± 0.402	−1.29	−1.68	−1.16

Table 14
Line Parameters of the −54.5 km s^{-1} Component (“H2”) in the $\nu_2 = 2$–1 Transition

Transition	λ (μm)	E_l (K)	g_l	g_u	A_{ul} (s^{-1})	$v_{\rm LSR}$ (km s^{-1})	σ_v (km s^{-1})	N_l ($\times 10^{15}$ cm^{-2})	W_v (km s^{-1})	log $_{10}(\tau_{p,\rm thin})$
$11_{0,11}$-$10_{1,10}$	5.667	3891.4	63	69	27.6	−51.5 ± 3.1	7 ± 4	0.8 ± 0.3	1.582 ± 1.136	−1.01
$11_{0,11}$-$10_{1,10}$	5.667	3891.4	63	69	27.6	−55.2 ± 7.2	7 ± 11.7	0.5 ± 0.5	1.058 ± 2.386	−1.19
$6_{2,5}$-$5_{1,4}$	5.7627	2878.3	33	39	10.9	−53 ± 6.1	7 ± 6.7	1.4 ± 1	1.352 ± 1.936	−1.05
$9_{1,9}$-$8_{0,8}$	5.7754	3362.5	17	19	25.2	−51.9 ± 2.9	7 ± 4.1	0.7 ± 0.2	1.404 ± 0.964	−1.07
$8_{1,8}$-$7_{0,7}$	5.8322	3136.9	45	51	23.9	−54 ± 3.5	7 ± 5.7	0.7 ± 0.4	1.47 ± 1.728	−1.05
$4_{2,3}$-$3_{1,2}$	5.8491	2549.6	21	27	9.1	−54.5 ± 7.9	8 ± 13.3	1.1 ± 1.2	1.04 ± 2.212	−1.27
$4_{2,3}$-$3_{1,2}$	5.8491	2549.6	21	27	9.1	−54.5 ± 7.9	8 ± 13.3	1.1 ± 1.2	1.04 ± 2.212	−1.27
$6_{2,5}$-$6_{1,6}$	5.9052	2938.5	39	39	4.2	−53.3 ± 5.5	7 ± 8.7	1.9 ± 1.4	0.648 ± 0.956	−1.42
$6_{1,6}$-$5_{0,5}$	5.9485	2763	33	39	20.7	−51.4 ± 2.9	7 ± 3.6	0.8 ± 0.2	1.538 ± 0.924	−1.03
$5_{1,5}$-$4_{0,4}$	6.0059	2614.4	9	11	18.8	−53.7 ± 4.2	9 ± 9.7	1 ± 0.8	1.966 ± 3.016	−1.04
$4_{2,3}$-$4_{1,4}$	6.0224	2620.4	27	27	5.9	−50.5 ± 14.4	7.4 ± 13	4.4 ± 5.4	2.122 ± 5.51	−0.89

Table 14
(Continued)

Transition	λ (μm)	E_l (K)	g_l	g_u	A_{ul} (s^{-1})	$v_{\rm LSR}$ (km s^{-1})	σ_v (km s^{-1})	N_l ($\times 10^{15}$ cm^{-2})	W_v (km s^{-1})	log $_{10}(\tau_{p,\rm thin})$
$4_{2,3}$-$4_{1,4}$	6.0224	2620.4	27	27	5.9	−54.3 ± 7.5	7 ± 9.2	3.8 ± 3.7	1.89 ± 3.766	−0.9
$4_{1,4}$-$3_{0,3}$	6.0613	2491.3	21	27	16.6	−53.9 ± 1.5	7 ± 2.3	1.2 ± 0.2	2.116 ± 0.872	−0.89
$2_{2,1}$-$2_{1,2}$	6.101	2412.5	15	15	5.9	−53.3 ± 4.3	7 ± 8	1.3 ± 1	0.68 ± 1.058	−1.4
$2_{1,2}$-$1_{0,1}$	6.1753	2328.3	9	15	13.9	−54.7 ± 6	9 ± 12.7	0.9 ± 0.9	1.876 ± 3.926	−1.05
$2_{1,1}$-$2_{0,2}$	6.2878	2395.1	5	5	17.7	−54.7 ± 11.8	7 ± 12.3	0.7 ± 0.9	1.24 ± 3.296	−1.08
$1_{1,0}$-$1_{0,1}$	6.3157	2328.3	9	9	21.3	−54.7 ± 5.1	7 ± 6.1	0.8 ± 0.4	1.748 ± 1.898	−0.96
$3_{1,2}$-$3_{2,1}$	6.5994	2617.1	21	21	19.1	−55 ± 5.9	7 ± 4.1	3 ± 1	5.512 ± 4.508	−0.41
$3_{1,2}$-$3_{2,1}$	6.5994	2617.1	21	21	19.1	−53.6 ± 4.2	7 ± 4.7	1.6 ± 0.6	3.264 ± 2.532	−0.69
$5_{1,4}$-$5_{2,3}$	6.616	2954.6	33	33	23.3	−53 ± 2.9	7 ± 3.9	0.7 ± 0.2	1.856 ± 1.11	−0.95
$7_{2,5}$-$7_{3,4}$	6.6462	3542.9	45	45	24.3	−52 ± 17.7	7 ± 13.5	0.2 ± 0.4	0.708 ± 2.024	−1.32
$2_{0,2}$-$3_{1,3}$	6.7455	2502.3	7	5	18.4	−52.2 ± 6.4	7.3 ± 9.7	1 ± 0.7	1.574 ± 2.374	−1.05
$7_{3,4}$-$7_{4,3}$	6.7536	3700	45	45	18	−51.5 ± 5.6	7 ± 5.9	0.5 ± 0.2	1.056 ± 0.958	−1.21
$6_{3,3}$-$6_{4,2}$	6.7814	3451.2	13	13	15.2	−51.5 ± 4.6	7 ± 6.7	0.5 ± 0.3	0.886 ± 0.966	−1.29
$4_{1,4}$-$4_{2,3}$	6.7857	2744.7	27	27	11.1	−51.5 ± 6.7	7 ± 9.1	0.6 ± 0.4	0.81 ± 1.174	−1.32
$9_{5,4}$-$9_{6,3}$	6.8322	4777.3	57	57	15.4	−50.5 ± 7.6	7 ± 5.9	1.1 ± 0.6	1.954 ± 2.454	−0.91
$4_{1,4}$-$5_{0,5}$	6.8449	2763	33	27	16	−54.3 ± 2.7	7 ± 3.8	1.3 ± 0.4	2.016 ± 1.366	−0.9
$1_{1,0}$-$2_{2,1}$	6.8512	2506.3	15	9	26	−57.5 ± 6.8	9 ± 5.6	1.6 ± 0.7	2.982 ± 2.762	−0.82
$3_{1,2}$-$4_{2,3}$	7.0096	2744.7	27	21	13.1	−52.7 ± 5.2	9 ± 5.8	1.5 ± 0.5	2.002 ± 1.41	−1.03
$6_{1,6}$-$7_{0,7}$	7.0362	3136.9	45	39	15.6	−54.8 ± 4.7	9 ± 7.8	1.8 ± 1.1	3.13 ± 4.02	−0.81
$8_{0,8}$-$9_{1,9}$	7.2337	3614.1	19	17	14.5	−54.5 ± 1.9	9 ± 3.8	0.7 ± 0.2	1.286 ± 0.802	−1.23
$3_{2,2}$-$4_{3,1}$	7.2371	2885.5	9	7	17.5	−54.4 ± 5.3	7 ± 6.5	0.1 ± 0.1	0.276 ± 0.362	−1.73
$3_{2,2}$-$4_{3,1}$	7.2371	2885.5	9	7	17.5	−54.4 ± 5.3	7 ± 6.5	0.1 ± 0.1	0.276 ± 0.362	−1.73
$3_{3,0}$-$4_{4,1}$	7.2937	3063.4	27	21	28.4	−54.4 ± 4.7	7 ± 5.7	0.2 ± 0.1	0.634 ± 0.76	−1.38
$4_{3,2}$-$5_{4,1}$	7.4294	3239.3	33	27	20.8	−50.5 ± 5.4	9 ± 6.1	0.8 ± 0.4	2.144 ± 2.176	−0.97

ORCID iDs

Jialu Li (李佳璐) https://orcid.org/0000-0003-0665-6505
Adwin Boogert https://orcid.org/0000-0001-9344-0096
Andrew G. Barr https://orcid.org/0000-0003-4909-2770
Curtis DeWitt https://orcid.org/0000-0002-6528-3836
Maisie Rashman https://orcid.org/0000-0002-3936-2469
David Neufeld https://orcid.org/0000-0001-8341-1646
Nick Indriolo https://orcid.org/0000-0001-8533-6440
Yvonne Pendleton https://orcid.org/0000-0001-8102-2903
Edward Montiel https://orcid.org/0000-0003-2553-4474
Matt Richter https://orcid.org/0000-0002-8594-2122
J. E. Chiar https://orcid.org/0000-0003-2029-1549
Alexander G. G. M. Tielens https://orcid.org/0000-0003-0306-0028

References

Asplund, M., Grevesse, N., Sauval, A. J., et al. 2009, ARA&A, 47, 481
Astropy Collaboration, Price-Whelan, A. M., Sipőcz, B. M., et al. 2018, AJ, 156, 123
Astropy Collaboration, Robitaille, T. P., Tollerud, E. J., et al. 2013, A&A, 558, A33
Barr, A. G., Boogert, A., DeWitt, C. N., et al. 2018, ApJL, 868, L2
Barr, A. G., Boogert, A., DeWitt, C. N., et al. 2020, ApJ, 900, 104
Barr, A. G., Boogert, A., Li, J., et al. 2022a, ApJ, 935, 165
Barr, A. G., Li, J., Boogert, A., et al. 2022b, A&A, 666, A26
Beltrán, M. T., & de Wit, W. J. 2016, A&ARv, 24, 6
Bergin, E. A., Alves, J., Huard, T., et al. 2002, ApJL, 570, L101
Bernstein, M. P., Allamandola, L. J., & Sandford, S. A. 1997, AdSpR, 19, 991
Bernstein, M. P., Sandford, S. A., Allamandola, L. J., et al. 1995, ApJ, 454, 327
Beuther, H., Churchwell, E. B., McKee, C. F., et al. 2007, in Protostars and Planets V, ed. B. Reipurth, D. Jewitt, & K. Keil (Tucson, AZ: Univ. Arizona Press), 165
Boonman, A. M. S., Doty, S. D., van Dishoeck, E. F., et al. 2003, A&A, 406, 937
Boonman, A. M. S., & van Dishoeck, E. F. 2003, A&A, 403, 1003
Caratti o Garatti, A., Stecklum, B., Garcia Lopez, R., et al. 2017, NatPh, 13, 276
Cardelli, J. A., Meyer, D. M., Jura, M., et al. 1996, ApJ, 467, 334
Carr, J. S., & Najita, J. R. 2008, Sci, 319, 1504
Cartledge, S. I. B., Lauroesch, J. T., Meyer, D. M., et al. 2004, ApJ, 613, 1037
Cernicharo, J., Lim, T., Cox, P., et al. 1997, A&A, 323, L25
Cesaroni, R., Galli, D., Lodato, G., et al. 2007, in Protostars and Planets V, ed. B. Reipurth, D. Jewitt, & K. Keil (Tucson, AZ: Univ. Arizona Press), 197
Chavarría, L., Herpin, F., Jacq, T., et al. 2010, A&A, 521, L37
Clarke, M., Vacca, W. D., & Shuping, R. Y. 2015, in ASP Conf. Ser. 495, Astronomical Data Analysis Software an Systems XXIV, ed. A. R. Taylor & E. Rosolowsky (San Francisco, CA: ASP), 355
Draine, B. T. 2011, in Physics of the Interstellar and Intergalactic Medium, ed. B. T. Draine (Princeton, NJ: Princeton Univ. Press)
Draine, B. T., Roberge, W. G., & Dalgarno, A. 1983, ApJ, 264, 485
Dungee, R., Boogert, A., DeWitt, C. N., et al. 2018, ApJL, 868, L10
Faure, A., & Josselin, E. 2008, A&A, 492, 257
Frost, A. J., Oudmaijer, R. D., de Wit, W. J., et al. 2021, A&A, 648, A62
Gibb, E. L., Whittet, D. C. B., Boogert, A. C. A., et al. 2004, ApJS, 151, 35
Goldsmith, P. F., & Langer, W. D. 1999, ApJ, 517, 209
Goldsmith, P. F., Melnick, G. J., Bergin, E. A., et al. 2000, ApJL, 539, L123
Goto, M., Geballe, T. R., Harju, J., et al. 2019, A&A, 632, A29
Harris, C. R., Millman, K. J., van der Walt, S. J., et al. 2020, Natur, 585, 357
Hollenbach, D., Elitzur, M., & McKee, C. F. 2013, ApJ, 773, 70
Hollenbach, D., Kaufman, M. J., Bergin, E. A., et al. 2009, ApJ, 690, 1497
Hosokawa, T., Yorke, H. W., & Omukai, K. 2010, ApJ, 721, 478
Hunter, J. D. 2007, CSE, 9, 90
Imai, H., Kameya, O., Sasao, T., et al. 2000, ApJ, 538, 751
Indriolo, N., Neufeld, D. A., Barr, A. G., et al. 2020, ApJ, 894, 107
Indriolo, N., Neufeld, D. A., DeWitt, C. N., et al. 2015, ApJL, 802, L14
Indriolo, N., Tan, J. C., Boogert, A. C. A., et al. 2018, ApJL, 865, L18
Jenkins, E. B. 2009, ApJ, 700, 1299
Karska, A., Herpin, F., Bruderer, S., et al. 2014, A&A, 562, A45
Kaufman, M. J., & Neufeld, D. A. 1996, ApJ, 456, 611
Kaźmierczak-Barthel, M., van der Tak, F. F. S., Helmich, F. P., et al. 2014, A&A, 567, A53
Knez, C., Lacy, J. H., Evans, N. J., et al. 2009, ApJ, 696, 471
Kuiper, R., Klahr, H., Beuther, H., et al. 2010, ApJ, 722, 1556
Kuiper, R., Klahr, H., Beuther, H., et al. 2011, ApJ, 732, 20

Lacy, J. H. 2013, ApJ, 765, 130
Lacy, J. H., Richter, M. J., Greathouse, T. K., et al. 2003, Proc. SPIE, 4841, 1572
Lahuis, F., & van Dishoeck, E. F. 2000, A&A, 355, 699
Li, J., Boogert, A., Barr, A. G., et al. 2022, ApJ, 935, 161
Maud, L. T., Cesaroni, R., Kumar, M. S. N., et al. 2019, A&A, 627, L6
McKee, C. F., & Tan, J. C. 2003, ApJ, 585, 850
Mihalas, D. 1978, Stellar Atmospheres (San Francisco, CA: Freeman)
Mitchell, G. F., Maillard, J.-P., & Hasegawa, T. I. 1991, ApJ, 371, 342
Nakano, T. 1989, ApJ, 345, 464
Navarete, F., Galli, P. A. B., & Damineli, A. 2019, MNRAS, 487, 2771
Nickerson, S., Rangwala, N., Colgan, S. W. J., et al. 2021, ApJ, 907, 51
Nickerson, S., Rangwala, N., Colgan, S. W. J., et al. 2023, ApJ, 945, 26
Nieva, M.-F., & Przybilla, N. 2012, A&A, 539, A143
Ormel, C. W., Min, M., Tielens, A. G. G. M., et al. 2011, A&A, 532, A43
Purser, S. J. D., Lumsden, S. L., Hoare, M. G., et al. 2021, MNRAS, 504, 338
Rangwala, N., Colgan, S. W. J., Le Gal, R., et al. 2018, ApJ, 856, 9
Richter, M. J., Dewitt, C. N., McKelvey, M., et al. 2018, JAI, 7, 1840013
Rodgers, C. D., & Williams, A. P. 1974, JQSRT, 14, 319
Rodón, J. A., Beuther, H., Megeath, S. T., et al. 2008, A&A, 490, 213
Rothman, L. S., Gordon, I. E., Babikov, Y., et al. 2013, JQSRT, 130, 4
Salgado, F., Berné, O., Adams, J. D., et al. 2012, ApJL, 749, L21
Salyk, C., Pontoppidan, K. M., Blake, G. A., et al. 2011, ApJ, 731, 130
Snell, R. L., Howe, J. E., Ashby, M. L. N., et al. 2000, ApJL, 539, L101
Sofia, U. J., Cardelli, J. A., Guerin, K. P., et al. 1997, ApJL, 482, L105
Suri, S., Beuther, H., Gieser, C., et al. 2021, A&A, 655, A84
Takahashi, T., Silk, J., & Hollenbach, D. J. 1983, ApJ, 275, 145
Tennyson, J., Zobov, N. F., Williamson, R., et al. 2001, JPCRD, 30, 735
Tielens, A. G. G. M. 2005, in The Physics and Chemistry of the Interstellar Medium, ed. A. G. G. M. Tielens (Cambridge: Cambridge Univ. Press)
Tielens, A. G. G. M., & Allamandola, L. J. 1987, Interstellar Processes (Dordrecht: Springer), 397
van der Tak, F. F. S., Tuthill, P. G., & Danchi, W. C. 2005, A&A, 431, 993
van der Tak, F. F. S., van Dishoeck, E. F., Evans, N. J., et al. 2000, ApJ, 537, 283
van Dishoeck, E. F., & Helmich, F. P. 1996, A&A, 315, L177
van Dishoeck, E. F., Kristensen, L. E., Mottram, J. C., et al. 2021, A&A, 648, A24
Villanueva, G. L., Smith, M. D., Protopapa, S., et al. 2018, JQSRT, 217, 86
Vinogradoff, V., Fray, N., Duvernay, F., et al. 2013, A&A, 551, A128
Virtanen, P., Gommers, R., Oliphant, T. E., et al. 2020, NatMe, 17, 261
Wang, K.-S., Bourke, T. L., Hogerheijde, M. R., et al. 2013, A&A, 558, A69
Wang, Y., Beuther, H., Zhang, Q., et al. 2012, ApJ, 754, 87
Whittet, D. C. B. 2010, ApJ, 710, 1009
Wilson, C. D., Mason, A., Gregersen, E., et al. 2003, A&A, 402, L59
Yorke, H. W., & Bodenheimer, P. 1999, ApJ, 525, 330
Young, E. T., Becklin, E. E., Marcum, P. M., et al. 2012, ApJL, 749, L17
Zinnecker, H., & Yorke, H. W. 2007, ARA&A, 45, 481